MAGNETIC NANOPARTICLE CATALYST FOR HYDROGENATION OF FURFURAL TO BIOFUEL

AHMED HALILU

INSTITUTE OF GRADUATE STUDIES
UNIVERSITY OF MALAYA
KUALA LUMPUR

2016

University of Malaya

MAGNETIC NANOPARTICLE CATALYST FOR HYDROGENATION OF FURFURAL TO BIOFUEL

AHMED HALILU

DISSERTATION SUBMITTED IN FULFILMENT OF THE

REQUIREMENTS FOR THE DEGREE OF MASTER OF PHILOSOPHY

INSTITUTE OF GRADUATE STUDIES (IGS)
UNIVERSITY OF MALAYA
KUALA LUMPUR

2016

University of Malaya

UNIVERSITY OF MALAYA

ORIGINAL LITERARY WORK DECLARATION

Name of Candidate: AHMED HALILU

Registration/Matric No: HGA140003

Name of Degree: MASTER OF PHILOSOPHY

Title of Thesis ("this Work"): MAGNETIC NANOPARTICLE CATALYST FOR HYDROGENATION OF FURFURAL TO BIOFUEL

Field of Study: CHEMICAL ENGINEERING (ENERGY)

I do solemnly and sincerely declare that:

(1) I am the sole author/writer of this Work;
(2) This Work is original;
(3) Any use of any work in which copyright exists was done by way of fair dealing and for permitted purposes and any excerpt or extract from, or reference to or reproduction of any copyright work has been disclosed expressly and sufficiently and the title of the Work and its authorship have been acknowledged in this Work;
(4) I do not have any actual knowledge nor do I ought reasonably to know that the making of this work constitutes an infringement of any copyright work;
(5) I hereby assign all and every rights in the copyright to this Work to the University of Malaya ("UM"), who henceforth shall be owner of the copyright in this Work and that any reproduction or use in any form or by any means whatsoever is prohibited without the written consent of UM having been first had and obtained;
(6) I am fully aware that if in the course of making this Work I have infringed any copyright whether intentionally or otherwise, I may be subject to legal action or any other action as may be determined by UM.

Candidate's Signature Date:

Subscribed and solemnly declared before,

Witness's Signature Date:

Name: Prof. Dr. Sharifah Bee Abd Hamid

Designation: Supervisor

University of Malaya

ABSTRACT

The growing global energy demands as a result of population increase, the excessive dependency on depleting fossil oil, and the health-environmental issues posed by fossil oil have prompted the need for clean energy alternative via renewable energy options. Consequently, this study was undertaken to solve these energy issues via heterogeneous catalysis. A simple repeating unit of $Fe(MFe)O_4$-SiO_2 (M = Ni, Ru) heterogeneous catalyst was design, built and optimized on Gaussian computational platform using the mechanics method and universal force field (UFF) functional. Data on vibrational spectroscopy of metal to point charge linkages of simple repeating unit of the catalyst was acquired. This was preceded with experimental one-pot synthesis at ambient condition into a novel template free mesoporous magnetic $Fe(MFe)O_4$-SiO_2 nanoparticle catalyst. The experimental vibrational modes were corroborated with the computational vibration modes to mark the outstanding capacities of the catalyst in hydrogenation of biomass derived oxygenates to biofuel. The catalysts physicochemical properties were confirmed using Raman Spectroscopy, X-ray Diffraction (XRD), Atomic Force Microscopy (AFM), High Resolution Transmission Electron Microscopy (HRTEM), Field Emission Scanning Electron Microscopy (FESEM), Vibrating Sample Magnetometer Analysis (VSM), and X-ray Photoelectron Spectroscopy (XPS). As a parameter to confirm the catalyst inverse spinel structure, the crystal field stabilization energy (CFSE) for Ni, Ru and Fe $^{n+}$ phases in the catalyst were quantitatively evaluated as; CFSE-Fe $^{2+}$ ~ -4.03578 $\times 10^{-10}$ eV and CFSE-Fe $^{3+}$ 0 eV, CFSE-Ni $^{2+}$ ~ -7.4388 $\times 10^{-11}$ eV and CFSE-Ru $^{3+}$ ~ -10.7618 $\times 10^{-11}$ eV. The active Ni $^{2+}$ and Ru $^{3+}$ component incorporation at the octahedral site was confirmed with the octahedral site preference energy (OSPE) values being; OSPE Ni $^{2+}$ ~ -5.2347 $\times 10^{-11}$ eV and OSPE for Ru $^{3+}$ ~ -7.4883 $\times 10^{-11}$ eV. In addition, super paramagnetic physical properties of the catalyst with low coercivity of 6.991 G for $Fe(MFe)O_4$-SiO_2 catalyst compared with

University of Malaya

27.323 G for Fe_3O_4-SiO_2 core shell geometry supports the OSPE. These are intrinsic properties that were confirmed to reveal the extrinsic properties such as BET nitrogen adsorption analysis mesoporosity of the catalyst as corroborated with AFM revealing approximately < 20 nm pore sizes and 14.32 nm particle sizes from XRD and HTREM analysis. The catalyst showed redox property at 400-500 ^oC and makes it potentially effective for hydro-processing reactions. Correspondingly, > 92 % conversion of furfural to furfuryl alcohol at 90-250 ^oC and 5-20 bar was observed during hydrogenation reaction over $Fe(MFe)O_4$-SiO_2 catalyst. Also, 100% conversion of furfural to furfural alcohol, pentane and tetrahydrofuran; and vanillin to vanillyl alcohol, guaiacol, cyclohexane, cyclohexanol and cyclohexanone was observed at 250 ^oC and 90 bar over the catalyst. With the aid of time dependent density functional theory on B3LYP functional that revealed the highest occupied molecular orbital and the lowest unoccupied molecular orbital of furfural and vanillin, GC-MS and GC-FID, TPR analysis, a probable mechanism via a non-hydrogen spillover route was proposed for the formation of the aforementioned biofuel molecules. The catalyst recorded six cycles of reusability and ~100 % recoverability.

University of Malaya

ABSTRAK

Keperluan untuk bekalan tenaga global yang semakin meningkat akibat pertambahan penduduk, pergantungan terhadap bahan api fosil secara berlebihan, kesan-kesan negatif terhadap kesihatan dan alam sekitar telah menjana keperluan untuk sumber tenaga alternatif yang bersih serta boleh diperbaharui. Justeru itu, kajian ini telah dijalankan bagi menyelesaikan isu-isu tersebut melalui pemangkinan heterogen. Satu unit berulang mudah, Fe (MFe) O_4-SiO_2 (M = Ni, Ru) yang merupakan pemangkin heterogen, telah direka, dibina dan dioptimumkan menerusi platfom pengkomputeran Gaussian dengan menggunakan kaedah mekanik dan "Universal Force Field" (UFF). Data berkaitan getaran spektroskopi pada ikatan antara logam dan titik caj yang merupakan sebahagian unit berulang mudah tersebut telah diperoleh. Langkah ini telah didahului dengan eksperimen sintesis satu periuk pada keadaan ambien bagi menghasilkan Fe (MFe) O_4-SiO_2 yang "mesoporous" tanpa sebarang templat yang juga merupakan pemangkin bersaiz nano. Data berkenaan mod getaran daripada eksperimen ini turut disokong dengan data daripada pengiraan mod yang menandakan kapasiti tinggi bagi pemangkin ini dalam penghidrogenan bahan teroksida berasaskan biojisim kepada bahan api bio. Sifat fizikokimia pemangkin ini telah dikaji menggunakan analisis spektroskopi Raman, pembelauan X-ray (XRD), mikroskop daya atom (AFM), mikroskop elektron penghantar berosolusi tinggi (HRTEM), "Field Emission Electron Microscope" (FESEM), "Vibrating analysis sampel magnetometer" (VSM) dan spektroskopi X-ray fotoelektron (XPS). Sebagai parameter untuk mengesahkan struktur spinel songsang pemangkin, tenaga penstabilan bidang kristal (CFSE) untuk fasa Ni, Ru dan Fe^{n+} dalam pemangkin telah dinilai secara kuantitatif untuk menghasilkan; CFSE-Fe^{2+} ~ -4.03578×10^{-10} eV dan CFSE-Fe^{3+} 0 eV, CFSE-Ni^{2+} ~ -7.4388×10^{-11} eV dan CFSE-Ru^{3+} ~ -10.7618×10^{-11} eV. Kedudukan komponen aktif Ni^{2+} dan Ru^{3+} di tapak oktahedron yang telah disahkan dengan tenaga keutamaan tapak oktahedron

University of Malaya

(OSPE); OSPE Ni $^{2+}$ ~ -5.2347× 10^{-11} eV dan OSPE for Ru $^{3+}$ ~ -7.4883× 10^{-11} eV. Di samping itu, sifat fizikal pemangkin sebagai paramagnet super dengan kadar perubahan sifat magnetik yang rendah pada 6,991 G untuk pemangkin Fe (MFe) O_4-SiO_2 berbanding 27,323 G untuk Fe_3O_4-SiO_2 ,yang merupakan teras pemangkin tersebut, turut menyokong data OSPE ini. Ini merupakan ciri-ciri intrinsik yang mendedahkan sifat-sifat luaran pemangkin ini seperti analisis penjerapan "mesoporosity" BET nitrogen yang turut disokong dengan AFM yang mendedahkan saiz 20 nm liang dan ~ 14.32 nm saiz zarah daripada XRD dan analisis HTREM. Pemangkin ini juga mengalami tindak balas redoks antara 400-500 ^oC , menjadikannya berpotensi untuk tindak balas pemprosesan hidro. Sejajar dengan itu, > 92% penukaran furfural ke furfural alkohol antara 90-250 ^oC dan 5-20 bar dapat diperhatikan semasa tindak balas penghidrogenan dengan menggunakan Fe(MFe)O_4-SiO_2 sebagai pemangkin. Turut dapat diperhatikan adalah 100% penukaran furfural kepada furfural alkohol, pentana dan tetrahidrofuran; serta vanilin kepda vanillil alkohol, guaiacol, sikloheksana, sikloheksanol dan sikloheksanon pada 250 ^oC dan 90 bar dengan menggunakan pemangkin tersebut. Dengan bantuan, "time dependent density functional theory" menerusi fungsi B3LYP yang mendedahkan orbital molekul tertinggi yang diduduki dan orbital molekul terendah yang tidak diduduki furfural dan vanillin, GC-MS dan GC-FID, dan analisis TPR mekanisme bukan melalui limpahan hidrogen telah dicadangkan untuk pembentukan molekul bahan api bio yang dinyatakan di atas.

University of Malaya

ACKNOWLEDGEMENTS

Indeed, all praises are for He that begins all begining before the begining began. We seek his help, forgiveness and guidance. We also seek refuge with Allah from the evil of our own souls. We send praises to him; the life that never die and will never die, the life that neigther sleep nor slumber, the first and last, the architect of heaven and earth and what is in between. Whomsoever He guides, can never be misguided, and whomsoever He leaves astray, no one can guide such a person. I bear withness that there is no god worthy of worship but Allah alone, and I bear witness that Muhammad son of Abdullah (SAW) is his slave and messenger.

Majority of the experimentals during the progression of this study, were carried out chiefly using state of the art facilities in Nanotechnology and Catalysis Research Center (NANOCAT) and partly in IPPP, Physics Department University of Malaya as well as MIMOS, Malaysia. High Impact Research (HIR) under University of Malaya funded the research from project grant number F-00032, together with National Research Institute for Chemical Technology (NARICT) Zaria Nigeria and my Guardian. I am grateful for all the assistance provided so far.

I am highly grateful to my distinguished supervisor, Prof. Dr Sharifah Bee Abd Hamid, Director Nano Technology and Catalysis Research Center (NANOCAT) for all the insightful support and encouragement in various aspects and capacities. I am also thankful to my distinguished Prof. Dr. Idris, Muhammad Bugaje, Director General National Research Institute for Chemical Technology (NARICT) for being one of my source of adventourous and piecing confidence into the scientific and chemical engineering world. Many thanks also goes to Dr Nurudeen Yusuf and Arc Badiru for the unconditional togetherness, I appreciate the sincere advice offered at the onset of this study. I also appreciate Dr Abdulazeez Yusuf Atta and Dr Yahya Muhammad Sani for their involvement in various aspects and capacities. My sincere appreciation also

University of Malaya

goes to Dr I.A Umar my first supervisor and research mentor at Department of Chemical Engineering, Ahmadu Bello University Zaria Nigeria. Warm regards also goes to my co-authors expecially the academic icon Prof. Dr. Suresh K. Bhargava of RMIT, Melbourne. Many thanks also goes to other co-authors in person of Dr Tammar Hussein Ali and Dr Putla Sudarsanam for all the assistance. Still on, many thanks go to Messrs; Abdulazeez Isa, Sharafadeen Gbadamasi, Abimbola Adebisi, Murtala Maidamma Ambursa, Dr Abubakar Ahmed, Dr Muhammad Hakim, Dr Hayyan Adeeb, Abubakar Habib Adebisi, Yusuf Asfa Sunnah, Aliyu I Yerimah, Taofeeq Imran, Ahmad Ibraheem Muazzam, Saidu Mahmud Ahmad, Abdurrasheed Ayuba, Yusuf Basheeru Aliero, Harith Rashid Raza, Dr Jimmy, Dr Rakibul Hasan, Dr Rasel Das, Luqman muhammad Hakim and Nadia Jamal, Dr. Md Ziaul, Mrs Nur Azrin, Mrs Dilah, Mrs Durga, Mrs Nur Atiqa Dawud, Mrs Nur Azimah, Mrs Ameerah, Ms Emy Marlina, Ms Norlia, Ms. Tan Tongling, Ms Swe Jyan Teh, Mrs Elisa Rasouli, Mrs Mazlita, Ms Nor Fateha, Mrs Saba, Mr Mohamad Safuan Kamaruddin, Mr Subratat Saha, Mr Wafiy, Mr Hun Tiar Ong, and many more others whom names are not mentioned but have contributed in one way or the other.

I reserved the last part of my acknowledgement to my family because they are my greatest assets. To my beloved and deceased father Khalil bn Ahmad, i pray that Allah reunit us in Jannah. To my lovely and ever patient mother Ruqayyah bint Uthman; a rare gem for being the catalyst of my upliftment. To my mentor Arch Abdulqadir Muhammad, I appreciate every bit of guidance given to me right from childhood. Special appreciation goes to my one and only rare gem sister Saratu Bint Khalil we share a high binding energy. To my dia-atomic twin brothers and sisters Hussain Khalil, Hassan Khalil and Hussaina Khalil for keeping the electron distribution among us uniform. To my mono-atomic brothers and sister, Idris Khalil, Abubakar Sadiq Khalil, Amina Khalil, and late Khadija Khaleel many thanks. Still on, I appreciate my Uncle in

University of Malaya

person of Dr.Adam Abdullah and all the point charge-likes coordinated to him. I cannot forget my brothers and sister Tauheed, Jibril, Sulaiman and Hawwau for their prayers and concerns in unlimited capacities. And finally to my fiancee Amatullah for her prayers all through, i cherish, love and respect you all.

University of Malaya

TABLE OF CONTENTS

University of Malaya

University of Malaya

University of Malaya

University of Malaya

LIST OF FIGURES

University of Malaya

University of Malaya

University of Malaya

University of Malaya

University of Malaya

LIST OF TABLES

University of Malaya

University of Malaya

LIST OF SYMBOLS AND ABBREVIATIONS

HOMO	**:**	highest occupied molecular orbital
LUMO	:	lowest unoccupied molecular orbital
TPR	:	temperature programed reduction
FESEM	:	field emission scanning electron microscope
HRTEM	:	high resolution transmission electron microscope
XRF	:	X-ray fluorescence
TO-LO	:	transverse optical-longitudinal optical
TGA	:	thermal gravimetric analysis
DTG	:	differential thermal gravimetric analysis.
OSPE	:	octahedral site preference energy
CFSE	:	crystal field stabilization energy
Bi	:	Biot number
Nu	:	Nusselt number
$\mathbf{K_p}$	:	Thermal conductivity of particle
$\mathbf{K_f}$	:	Thermal conductivity of fluid
h	:	Heat transfer coefficient
$\mathbf{L_p}$	:	Particle size.

University of Malaya

LIST OF APPENDICES

;

University of Malaya

CHAPTER 1: INTRODUCTION

1.1 General introduction

This chapter gives the overall perspective of solving energy problem through heterogeneous catalysis on renewable feedstock alternative so as to mitigate issues associated with fossil derive ones. It went further to clarify on why mitigating the problems are worth investigating. The chapter gave general introduction in the field of research, as well as the present study.

The world is presently facing detrimental environmental problems due to vast consumption of fossil fuels and associated global warming effects (Serrano-Ruiz & Dumesic, 2011; Shuttleworth *et al.,* 2014). The consumption of fossil fuels results in increasing levels of greenhouse gas (GHG) emissions; CO_2 levels have increased from 284 ppm in 1832 to 397 ppm in 2013. Global GHG emissions are expected to rise by ~2.5% in 2015 compared with 2013 levels. If this situation continues, global average temperatures will increase by 2.5-5.4 ^{o}C above pre-industrial levels by 2050. Concurrently, it is expected that the global production of petroleum will reach a maximum by 2020 and thereafter decay gradually (Serrano-Ruiz & Dumesic, 2011; Tang *et al.,* 2014). This growing concern has motivated the researchers to search for alternative renewable feed-stocks for the production of fuels and chemicals.

In this context, biomass is a potential feedstock alternative to fossil fuels due to its high abundance, biodegradability, and remarkable sustainability (Climent, Corma, & Iborra, 2014; Tang *et al.,* 2014). Over 170 billion metric tons of biomass is produced per year by photosynthesis process. Especially, lignocellulose contains large amount of biomass with three major components: cellulose (~35-50%), hemicellulose (~20-35%), and lignin (~10-25%). Thus, the production of fuels and chemicals from lignocellulose derivatives is an attractive way to overcome the negative impacts of fossil fuels.

University of Malaya

Aldehydes are good precursors for photochemical smog and substrate for ozone formation. This is in addition to their reactiveness that leads to bio fuel ageing over time. This deters most of the fuel properties of bio-oil such as calorific value. Furfural being an aldehyde is one of the promising biomass platform chemicals that can be largely produced from acidic hydrolysis of hemicellulose (Climent *et al.,* 2014; G. Li *et al.,* 2014). Several processes have been developed for the conversion of furfural into a number of valuable chemicals and fuels, such as cyclopentane, furfuryl alcohol, 2-methylfuran, 2-methyltetrahydrofuran, tetrahydrofurfuryl alcohol, cyclopentanone, furfurylamine, 1,5-pentanediol, and so on. Furthermore, it becomes necessary that catalysts must exhibit a prominent role in the transformation of C (sp^2)-O carbonyl carbon of furfural into stable C (sp^3)-OH carbon of furfuryl alcohol at mild conditions or any fuel grade hydrocarbon. These implications provide numerous opportunities to develop cheap, promising, and easy recoverable catalysts for efficient hydro-processing of furfural to biofuels or platform chemicals. Vanillin on the other hand is also an aldehyde derived from lignin fragment of biomass. Under mild condition, formation of vanillyl alcohol is prominent and that may compliment furfural by investigating the catalyst activity on both furan and benzene ring respectively. At extreme conditions, formation of cyclic hydrocarbon is probable; this is a potential route in stabilizing bio-oil for instance. It is therefore plausible to note that application of magnetic nanoparticles in heterogeneous catalysis is growing tremendously due to the combined nano scale and magnetite properties (Gawande, Branco, & Varma, 2013; Polshettiwar *et al.,* 2011). To this regard, nano sized catalysts exhibit a number of unique properties, such as higher surface area, favorable electronic properties, and superior redox properties, which are significantly different from the bulk counterparts (Putla *et al.,* 2015). Owing to remarkable separation properties, magnetic catalysts offer a promising option that can meet the requirements of high accessibility with easy recoverability

University of Malaya

(Gawande *et al*., 2013; Polshettiwar *et al.,* 2011). As a result, filtration or centrifugation step and/or a tedious workup of the final reaction mixture can be avoided in several catalytic reactions. These beneficial properties of magnetic nanoparticles can contribute to achieve better results in the transformation of biomass derivatives such as bio-oil into valuable chemicals and fuels.

The present work has been undertaken in line with the above background. A simple repeating $Fe(MFe)O_4$-SiO_2 catalyst unit was designed, built and optimized on Guassian 09 computational platform. This was done to obtain prior vibrational spectroscopy of the linkages in the unit before experimentation to confirm and guide systematic synthesis of the catalyst. Therefore, experimental synthesis of a novel mesoporous magnetic $Fe(MFe)O_4$-SiO_2 nanoparticles catalyst using a one-pot methodology at ambient condition was achieved. The catalysts physicochemical properties have been confirmed using Raman spectroscopy, X-ray diffraction (XRD), Atomic force microscopy (AFM), High resolution transmission electron microscopy (HRTEM), Field emission scanning electron microscopy (FESEM), Vibrating sample magnetometer analysis (VSM), and X-ray photoelectron spectroscopy (XPS). In line with the identified catalyst physiochemical properties, catalytic performance was investigated for furfural to furfuryl alcohol at 90-250 ^oC and 5-20 barg during hydrogenation reaction. It was complimented further for furfural and vanillin at 250 ^oC and 90 barg, to yield furfuryl alcohol, pentane and tetrahydrofuran; vanillyl alcohol, guaiacol, cyclohexane, cyclohexanol and cyclohexanone respectively. However, to optimize the reaction conditions for furfural hydrogenation, the effect of reaction temperature, pressure, catalyst amount, and reactant concentration using magnetic $Fe(NiFe)O_4$-SiO_2 nano catalyst was investigated. Also, with the aid of time dependent density functional theory on B3LYP functional that revealed symmetry of highest occupied molecular orbital and the lowest unoccupied molecular orbital of furfural and vanillin, GC-MS and GC-FID,

University of Malaya

TPR analysis, a probable mechanism via a non-hydrogen spillover route was proposed for the formation of the aforementioned biofuel molecules during hydrogenation reaction.

1.2 Research problem statement

The problem that motivates this research is classified into three; environmental issue which involves aldehyde emission from biofuel, energy issue which involves low energy density value of biofuel, and finally process issues which involves the catalyst and process condition. Usually, turnover frequency (TOF), strength and concentration of catalytic active sites, textural properties such as surface area, porosity of heterogeneous catalyst, are the variable used in describing conventional catalysts. Because catalysts are metastable materials in dynamic states and can change with infinitesimally small change in prevailing reaction conditions, there is a need to study these changes in order to increase the catalyst performance for various reactions.

Lignocellulose derived bio-oil is chemically unstable due to the presence of carbonyl functionalities. These functionalities otherwise known as aldehydes are efficient precursors for photochemical smog formation. Smog complexes catalyze formation of ozone and can reduce oxygen profile for ozone. However, aldehydes are also the pivot that facilitates bio-oil to age over time. In an attempt to transform these carbonyl functionalities in aldehydes to more stable molecules so as to curb those aforementioned issues during practical applications of bio-oil, most of the conventional catalysts employed are noble metals with high metal loadings having no magnetic anisotropy. This prompt high incurred cost for the catalyst reusability and recoverability due to high cost of recoverability of non-magnetic catalyst. Also, process condition during catalyst activity evaluation is also usually high. Therefore, considering that most of the conventional catalysts are prepared via deposition of the active phase on the support

University of Malaya

materials, leaching is a major challenge for these conventional catalysts and may add to recurrent cost of any budget that considers research or even process industries. Our contribution in this field of study centers on introducing a new property such as the magnetic anisotropy in addition to others, so that cost of catalyst recoverability could be minimized. This is also being complimented further by tuning the catalyst active sites to be robust to leaching.

1.3 Justification for the study

The justification for the study centers on catalytic approach to tackle energy issues using renewable feedstock in order to compliment fossil derived ones. Against the conventional approach of using non-magnetic catalyst for the said justification, this study will no doubt open a platform that will improve biofuel production economics via upgrading of biomass derived oxygenates to solve most of the energy issues. Molecular modeling of the said magnetic catalyst and renewable feedstock as shown in the study creates a synergy of the catalyst activity and mechanism of the transformation process. The synergistic of the catalyst simulated symmetry and experiment as corroborated in this study agreed concurrently and this revealed high level of confidence from the *ab initio* considerations that the synthesized material is really the intended. In addition, the outstanding redox and textural properties of the catalyst suited for hydrogenation and other hydro-processing reactions via various spectroscopy experiments further reveal the superior nature of the catalyst. Therefore, the procedure developed for the catalyst actualization that results in yielding novel catalytic material is holistic to all kinds of material synthesis. This we also confirm to be one of the best procedures to develop new materials that have unique attributes for their specific applications. Interestingly, the study is in the readability profile of American Chemical Society (ACS) since February, 2016 and has received citation by July, 2016.

University of Malaya

1.4 Aim and objectives of the research

The aim of this study is divided into two stages: Prior to the first stage, catalyst was designed and modeled using quantum mechanics first principle approach, through universal force field functional so as to guide the synthesis process of the magnetic nano particle catalyst. The novel template free mesoporous catalyst consists of special and unique site to incorporate any kind of active noble or transition metal. The second stage involved investigation on the activities of the said catalyst for biofuel production from furfural and complimented with vanillin.

The main research objectives of this study are as follows:

- To synthesise metal incorporated magnetic $Fe(MFe)O_4$-SiO_2 via co-precipitation method.
- To determine the activity of the said catalyst in hydrogenation of cellulose derived furfural under varying reaction conditions.

Specific activities underlying the research objectives of the study include:

1- To design $Fe(MFe)O_4$-SiO_2 while considering the design parameters such as; catalyst nano size, catalyst shape, catalyst reducibility; design variables such as Biot number and Nusselt number that is informative on heat distribution around the catalyst, synthesis environment such as dynamic or steady; and design constraints such as the overall catalyst crystallite size should be $\geq$ sum of individual components of the catalyst. All these are guide by prior Guassian simulation of a simple repeating of $Fe(MFe)O_4$-SiO_2 catalyst.
2- To synthesize the catalyst while taking note of the design output (1)
3- To characterize the physical, chemical and textural properties of the synthesized catalyst (2)

University of Malaya

4- To investigate the activity of the catalyst during hydrogenation of furfurfal to biofuel under varying reaction conditions.

1.5 Scope of the research

The present study is limited to the synthesis of magnetic catalyst material and investigating its activity in hydrogenation of biomass-derived oxygenates such as furfural aldehyde to biofuel. The aim is to increase biofuel energy density and improve catalyst recoverability as one of the parameters in biofuel production cost as depicted in the general perspective of Fig 1.1.

Some researchers studied conventional catalyst such as metal supported on ordinary non-magnetic mesoporous silica in ameliorating the low energy density of biofuel. Nonetheless, these materials still have drawback of good recoverability due to their non-magnetic anisotropy nature. Despite the wide range of advances made on application of these catalyst materials, solving energy problem of biofuels is yet to replace petroleum diesel economically. This is due to incomplete fundamental understanding of the mechanism for the structure-activity relationship during catalysis. Increased cost of recoverability for these non-magnetic materials is therefore a challenge that needs to be solved. In this study, a novel magnetic material has been developed via a simple synthesis procedure that was guided via a prior prototype molecular modeling procedure to help assess and solve the draw backs associated with conventional catalysts with a test experiment using furfural and vanillin feed stocks. These oxygenates prominent in bio-oil in the form of aldehydes were converted into fuel grade molecules over the catalyst with metal and acid functions. Consequently, the present study went further to investigate the synergetic relationship between the catalyst surface atoms energetic that determines crystallite size as corroborated to activity during hydro-processing of furfural and vanillin.

University of Malaya

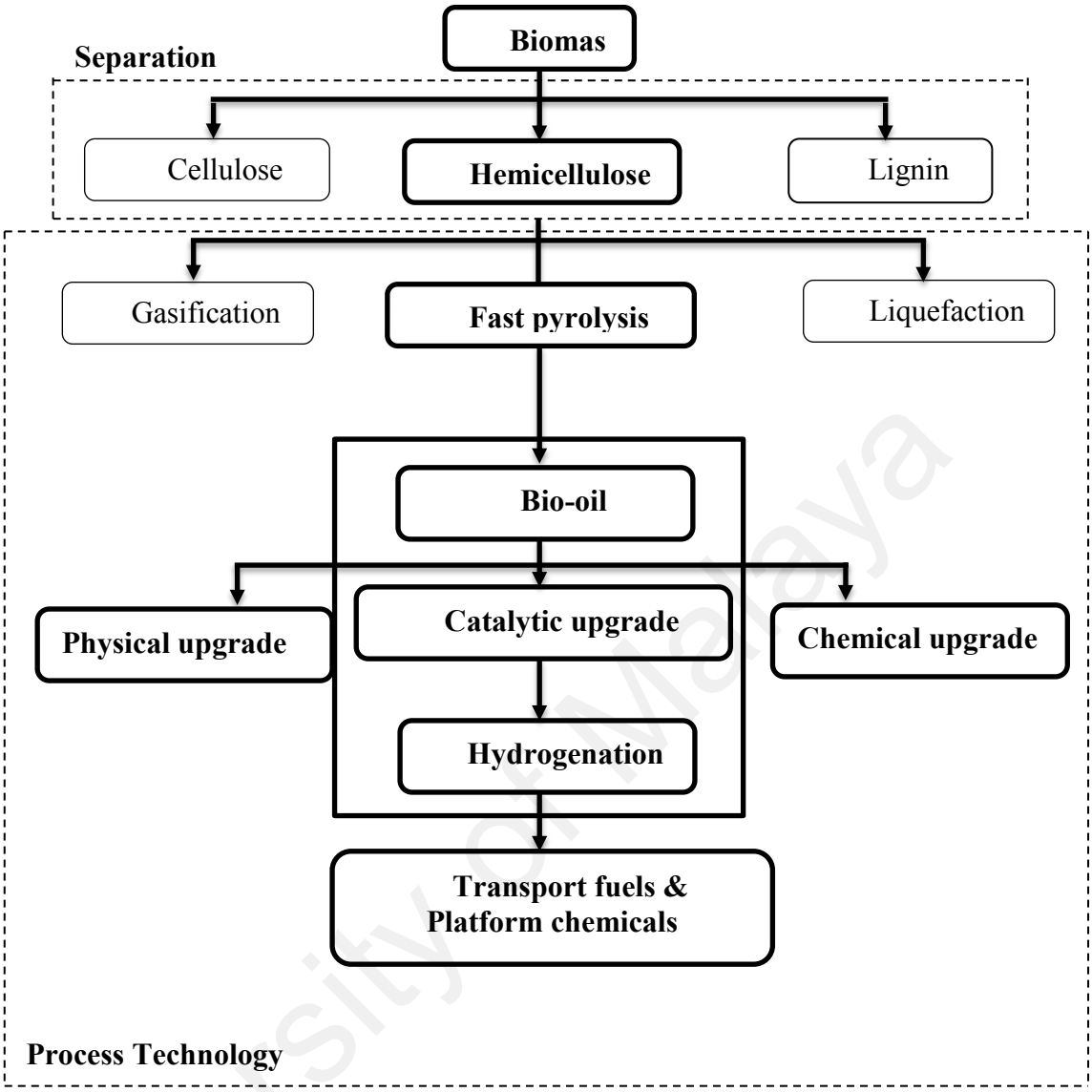

Fig. 1.1: General perspective to catalytic biofuel production from lignocellulose biomass.

University of Malaya

1.6 Outline of the thesis

The general layouts of the present thesis are organized in 7 chapters as follows:

The general layouts of the present thesis are organized in 7 chapters as follows:

Chapter 1- This chapter consists of a general introduction that gave elaborate research overview entailing the research objectives, perspective, and value preposition of the study, novelty of the catalyst and study, as well as question addressed by the research.

Chapter 2- The second chapter presents a review of literatures on bio-refinery concepts ranging from basic feed stocks such as lignocellulose biomass.

Chapter 3- This chapter presents all materials/method employed for the synthesis/development of $Fe(MFe)O_4$-SiO_2 nano particle catalyst.

Chapter 4- This chapter present results and discussion together with the catalyst design steps, synthesis steps, characterizations and catalyst activity study in line with the second objectives of the study. Data acquisition experiments for each of the characterization step are given therein. This is preceded with detailed data analysis step in order to understand fully the catalyst finger prints.

Chapter 5 - The chapter summarizes the overall conclusions and recommendations for future research proposal of the study.

Chapter 6- List of publication and papers presented.

Chapter 7- Conclusion and future work.

University of Malaya

CHAPTER 2: LITERATURE REVIEW

2.1 Bio-refinery concept

Bio-refinery has been defined by IEA Bioenergy task 42 as the ‘’sustainable processing of biomass into a spectrum of marketable products and energy’’ (Gupta, Tuohy, Kubicek, Saddler, & Xu, 2013). Therefore, Bio-refinery concept employs different technologies capable of isolating biomass into valued building blocks that have potentials to be converted into biofuels and platform chemicals. A network of facilities in this regard, integrates biomass conversion processes and equipment to produce transport fuels, power and chemicals. It is analogous to today’s petroleum refinery, which produces multiple fuels and products from crude petroleum (Rajagopal & Zilberman, 2007). The technological process in bio-refinery includes thermochemical process, biochemical process, mechanical process, and chemical processes. Thermochemical process such as gasification operates at >700 ^{o}C to produce syngas and pyrolysis operates ~300-600 ^{o}C to produce crude bio-oil (Demirbas, 2009; Zhang, Chang, Wang, & Xu, 2007). Biochemical process operates at low temperature and reaction rates with micro-organism fermentation such as anaerobic digestion (Romano & Zhang, 2008; Vertès, Inui, & Yukawa, 2008). Mechanical process is directed only on size reducing biomass or separating bio-refinery feedstock without changing the state or composition (Alvira, Tomás-Pejó, Ballesteros, & Negro, 2010; Huang, Ramaswamy, Tschirner, & Ramarao, 2008). Chemical process includes hydrolysis, trans-esterification, Fischer-Tropsch synthesis, mechanization, steam reforming (Alvira *et al.,* 2010).

University of Malaya

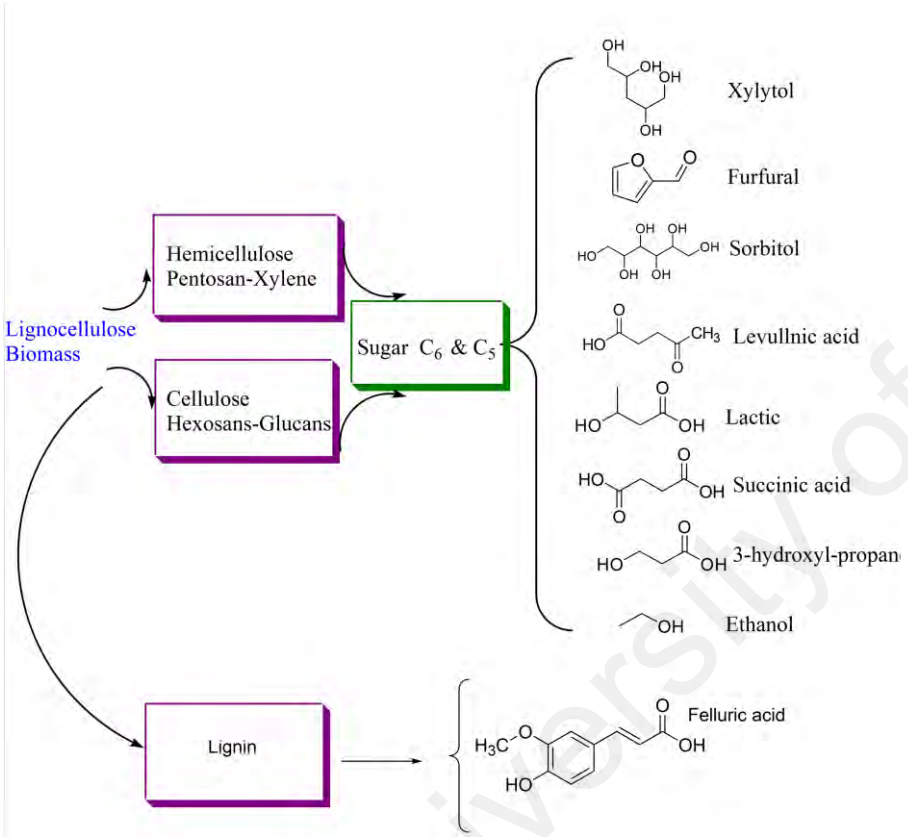

Fig. 2.1. Bio-refinery concept based on sugar platform (Fernando, Adhikari, Chandrapal, & Murali, 2006).

University of Malaya

2.2 Lignocellulose biomass

Lignocellulose biomass is the major energy plant that has huge potentials for fuel and chemical production (Chundawat, Beckham, Himmel, & Dale, 2011; Stöcker, 2008; Y. Sun & Cheng, 2002). Its structural building block is made of hemicellulose (~20-35%), cellulose (~35-50%), and lignin (~10-25%) fragments as shown in Fig 2.2. The more reactive sugar polymers in lignocellulose biomass are protected by the highly unreactive lignin fraction. Consequently, effective pre-treatment step is necessary to breakdown the refractory lignin seal for various potential applications.

Hemicellulose is a 3D-heterogeneous molecule with small crystalline region. The subunits in hemicellulose are composed of D-xylose, mannose, L-arabinose, galactose, glucuronic acids. These subunits are bonded by either β-1; 4-glycosidic bonds in main chains or β-1.2-, β -1.3-, β 1.6-glycosidic bonds of the inside chains. They are made of polyxylose, galactoglucomannan (gal-glu-man) and glucomannan (glu-man) polymers. The bond between three components of hemicellulose subunits contains chemical bond with lignin (Carvalheiro, Duarte, & Gírio, 2008; Gírio *et al.*, 2010; Mamman *et al.*, 2008; Saha, 2003).

Lignin is the heterogeneous biopolymers having guaiacylpropane (G), syringylpropane (S) and phydroxyphenylpropane (P) as basic subunits. These subunits are bonded with various ether bonds and carbon to carbon bond, mainly β-O-4 ether bonds (Fig 2.2). The basic polymer found in lignin includes guaiacyl lignin (G-lignin), guaiacyl syringyl lignin (GS-lignin) and guaiacyl syringyl hydroxyphenyl lignin (GSH-lignin). The composition of lignin is made of amorphous, heterogeneous, nonlinear 3D polymers. However, the bonds between three components contain chemical bond with hemicellulose. Its structures and subunits have been resolved through 2D HSQC NMR, based on 1H-13C

University of Malaya

correlations. Fig 2.3 presents some of the basic dimers that forms lignin building blocks such as: β-O-4 (~50%; aryl glycerol- β-aryl ether), α-O-4 (~2-8%; noncyclic benzyl aryl ether), β-5' (~9-12%; phenylcoumaran), 5-5' (~10-11; biphenyl), 4-O-5' (4~diaryl ether), β-1' (~7; 1,2 diaryl propane), β-β' (~3-5; pinoresinol) and 5-5'-α, β-O-4, dibenzodioxocin (2-7%), 5-O4' (biphenyl ether).

Basically to produce energy based products from lignocellulose biomass, methods such as pyrolysis at ~700 ^{o}C (Patwardhan, Brown, & Shanks, 2011; R. K. Sharma *et al.,* 2004), gasification at ~400-725 ^{o}C (Osada, Sato, Watanabe, Adschiri, & Arai, 2004; Resende, Fraley, Berger, & Savage, 2008), ionic liquids (Tan *et al.,* 2009), hydrogenolysis (Sakakibara & Nakayama, 1962), and oxidation (Halma *et al.,* 2015), have been widely employed to cleave these building block into smaller molecules. To further understand lignin treatments into fuel molecules, DFT studies revealed that ligands donates electron to the metal center so that C-O bond cleavage in lignin is facilitated (Cong Liu & Wilson, 2015). However, during pyrolysis of α-O-4 lignin dimers for instance, homolytic cleavage of C_{α}-O bond, homolytic cleavage of O-CH_3 bond and the homolytic cleavage of C-C bond have been shown to yield biofuels (Asmadi, Kawamoto, & Saka, 2011; J. Huang, Liu, Tong, Li, & Wu, 2014; Kawamoto, Watanabe, & Saka, 2015). Elemental component of all lignocellulose biomass and its ash content determines the overall energy density obtained. This is measured in terms of oxygen to carbon (O/C) ratio and HHV or LHV (Table 2.1) as the major determinants that may deters lignocellulose fuels being competitive with fossil energy density (Changjun Liu, Wang, Karim, Sun, & Wang, 2014).

University of Malaya

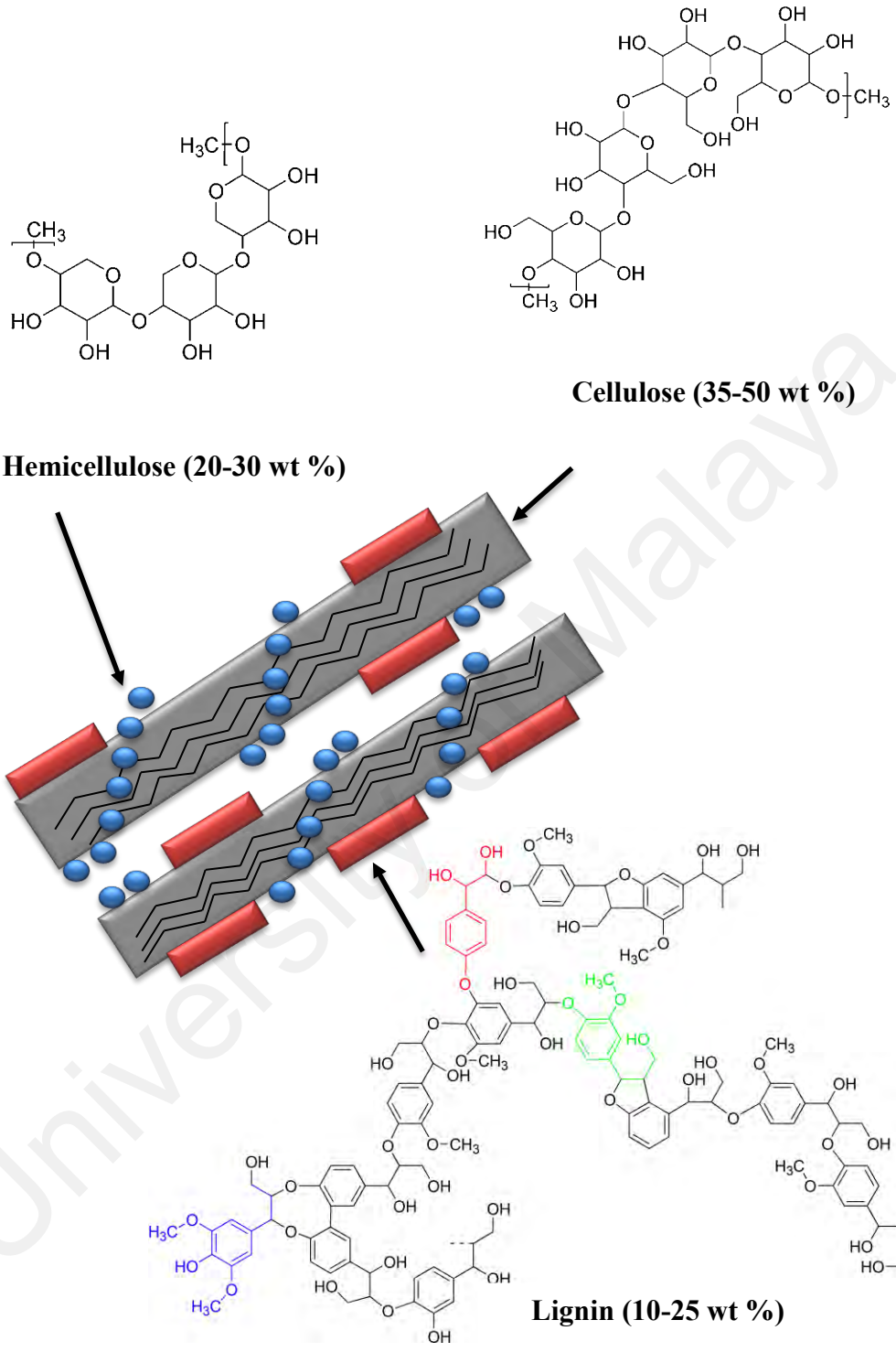

Fig. 2.2: Schematic representation of lignocellulosic biomass composition.

University of Malaya

Finally, Cellulose is a linear and homogeneous polymer composed of D-glucopyranose units linked by β-1, 4-glycosidic bonds. The carbon in cellulose is 44.44%, hydrogen is 6.17% and oxygen is 49.39%. β-1, 4-glycosidic bonds in cellulose building blocks confers rigidity and contributes to its overall chain stiffness. The basic polymer found in cellulose is the β-glucan. This is found in cellulose derived from wood, plants, tunicate, algae and bacterial (Moon, Martini, Nairn, Simonsen, & Youngblood, 2011). Cellulose fibrils in association with these building blocks are the main reinforcement in lignocellulose biomass.

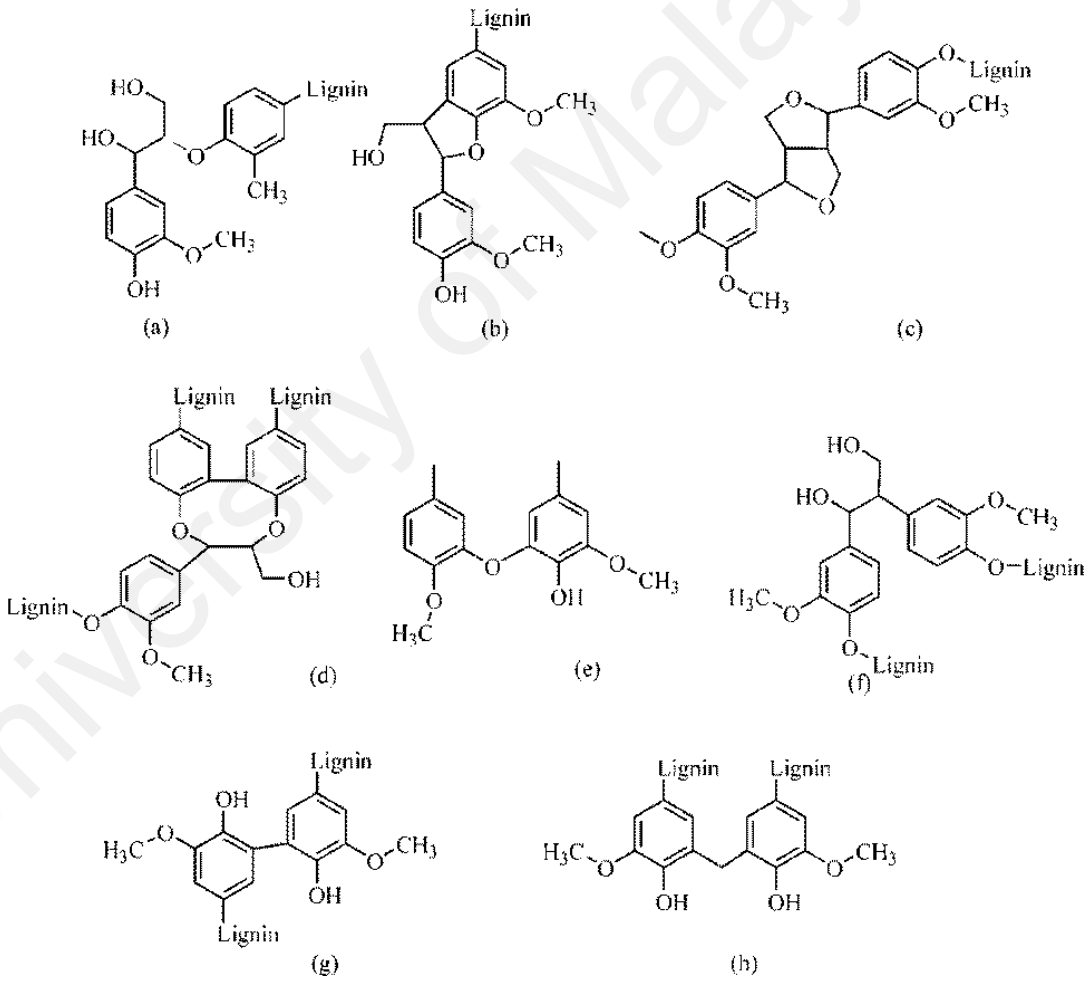

Fig. 2.3: Some major lignin dimers showing; (a) β-O-4 (Aryl glycerol- β-aryl ether), (b) β-5′ (phenylcoumaran), (c) β-β′ (pinoresinol), (d) 5-5′-α β-O-4, (dibenzodioxocin), (e) 5-O4′ (Biphenyl ether), (f) β-1′ (1, 2 diaryl propane), (g) 5-5′ (Biphenyl), (h) diphenyl methane (Zhu *et al.,* 2014).

University of Malaya

However, its reactivity depends on the three equatorially positioned primaries and two secondary –OH functionality with hydrogen bond network that makes cellulose insoluble in most organic solvents. The bond that exists between three components is without chemical bond to either hemicellulose or lignin (Badger, 2002; Ioelovich, 2008; Petropavlovskii & Kotel'nikova, 1979).

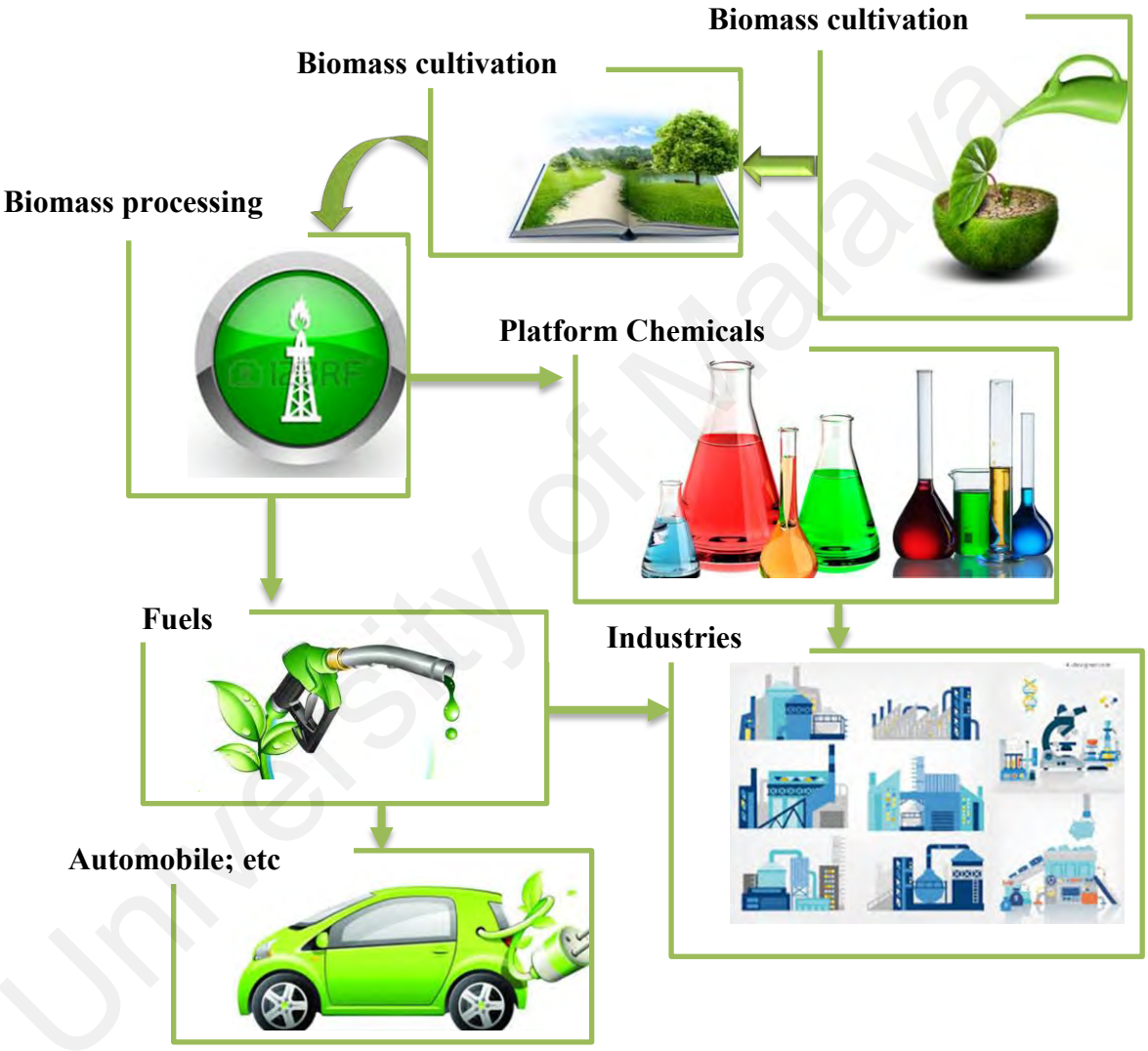

Fig. 2.4: Lignocellulose biomass prospects.

University of Malaya

Table 2.1: Physicochemical property of some familiar lignocellulose biomass.

Biomass	Elemental analysis (wt %)				Ash	O/C	HHV	Reference
	C	H	N	O	(wt %)		(MJ/kg)	
Palm tree	42.72	5.61	0.44	51.24	5.72	1.20	54.25	(Abnisa, Arami-Niya, Daud, Sahu, & Noor, 2013)
Wheat straw	58.4	6.00	0.10	-	0.09	-	-	(Sipilä, Kuoppala, Fagernäs, & Oasmaa, 1998)
Rapeseed	74.0	10.2	3.97	11.70	-	0.16	38.40	(S Şensöz, Angın, & Yorgun, 2000)
Microalgae	76.2	11.6	0.93	11.24	-	0.15	29.00	(Miao, Wu, & Yang, 2004)
Sesame	61.6	7.96	0.98	29.37	-	0.48	27.00	(Ateş, Pütün, & Pütün, 2004)
Bagasse	46.2	6.55	0.00	46.90	0.24	1.01	20.00	(Islam, Beg, & Islam, 2005)
Sunflower	66.5	9.20	4.50	19.80	-	0.30	32.20	(Gerçel, 2002)
Olive	66.9	9.20	2.00	21.90	-	0.32	31.80	(Sevgi Şensöz, Demiral, & Gerçel, 2006)
Rice straw	45.2	5.80	0.67	47.60	0.10	1.05	17.3	(D. C. Elliott, 2001; Tsai, Lee, & Chang, 2007)

HHV = highest heat value,

University of Malaya

2.3 Potentials of converting lignocellulose biomass to biofuels

The structural diversity in lignocellulose biomass as an energy plant considering its subunits, bond between subunits, composition, and polymer type is an indicative motivation to biofuel production from biomass. Lignocellulose biomass conversion to hydrocarbon biofuels was first reported in 1954 by Heinemann (Heinemann, 1954). Processes such as pyrolysis and hydrothermal methods are renowned for lignocellulose biomass conversion (Akash, Muchmore, & Lalvani, 1994; Goudriaan, Naber, & Van den Berg, 2005; Maldas & Shiraishi, 1997; Ramsurn & Gupta, 2012; van Dam, de Klerk-Engels, Struik, & Rabbinge, 2005; B. Zhang, von Keitz, & Valentas, 2008). Bio-oil is one of the main products from these processes (Table 2.2). However, recent studies showed that bio-oil as a multiphase liquid mixture contain over 1900 identified oxy-functionalized components such as aldehyde, acids, carbohydrates, phenolic, furan, ketones etc (Choi, 2015; Zacher, Olarte, Santosa, Elliott, & Jones, 2014), (Czernik & Bridgwater, 2004; Qin, Cui, Yi, & Wang, 2014), (Mortensen, Grunwaldt, Jensen, Knudsen, & Jensen, 2011; Staš, Chudoba, Kubička, & Pospíšil, 2015). The oxygen and water content in bio-oil depends on the method of production. Hydrothermal bio-oil production for instance, involves high pressure under N_2 or H_2O and the oxygen content of the bio-oil produced is usually low with typical composition; Carbon (68-81 wt %), sulfur + nitrogen (0.1 wt %), oxygen (9-25 wt %), water (6-25 wt %) and density (1.10-1.14 wt %) (Elliott *et al.,* 1991; Elliott, 2007; Peterson *et al.,* 2008). This is against pyrolysis bio-oil which yields bio-oil with high oxygen and water content and typical composition; Carbon (56-66 wt %), sulfur and nitrogen (0.1 wt %), oxygen (27-38 wt %), water (24-52 wt %) and density (1.10-1.2 wt %) (Bridgwater, 2012; Mohan, Pittman, & Steele, 2006). On general notes, biofuel production from lignocellulose biomass energy plants produces oxygenated compounds which may deter fuel properties

University of Malaya

(A. Bridgwater & Peacocke, 2000; A. V. Bridgwater, 2012; Choudhary & Phillips, 2011; D. C. Elliott, 2007) (Furimsky, 2000).

Aldehydes such as furfural (obtained from Hemicellulose fragments), vanillin and veratraldehyde (obtained from lignin fragments) are the main active species in bio-oil aside phenolic and other functionalities (Staš *et al.,* 2015). Aldehydes are non-regulated pollutants but causes adverse effect on human and environment. The reactive sp2 carbonyl carbon functionality in this oxygenates constitute major challenge in biofuels derived from lignocellulose biomass. This makes aldehydes in biofuel good precursor for photochemical smog formation (peroxide radicals; RCO_3) (Agarwal, 2007). Afterwards, they enhance ozone formation thereby making breathing difficult and also irritating to the eyes and nose in addition to their carcinogenic effects. Other class of bio-oil oxygenates only contributes to high O/C ratio in association to bio-oil calorific values or energy density. The interest in biofuel production is to get a high effective $H_{effective}$/C ratio [n (H)-2n (O)]/ (n(C) and a low O/C ratio.

In line with this background, furfural from hemicellulose is one of the vast arrays of chemicals that find wide applications in oil refining, plastics, pharmaceutical and agrochemical industries. There are no synthetic routes for the production of furfural ("Application Furfural," 1939; Mamman *et al.,* 2008; Yan, Wu, Lafleur, & Jarvis, 2014; Zeitsch, 2000). However, its production requires lignocellulose biomass rich in pentosans (Table 2.2 & 2.3 and Fig 2.5). Pentosan consists mostly of xylan therefore, through aqueous acid catalysis, pentosans are hydrolyzed to pentose and thereafter pentose is dehydrated to furfural in a unified process. However, furfural reaction loss is prominent in this case because of furfural resinification with furfural of various acidity or condensation in presence of xylose is most likely to occur. For instance in bagasse the ratio of xylan to Arabian is 18:24 (Zeitsch, 2000). This is so essential in the study of

University of Malaya

kinetics of xylose disappearance, an essential tool for the design of furfural reactors, as it permutes determination of residence time of the raw material in the reactor (Z. Chen, Zhang, Xu, & Li, 2015; Vinueza et al., 2015).

Furfural potentially involves in many type of reactions including; (a) Hydrogenation (b) Dehydration (c) C-O hydrogenolysis (d) Rearrangement (Lange, van der Heide, van Buijtenen, & Price, 2012), (e) C-C dissociation (Pang & Medlin, 2011; J. Sun & Liu, 2011), (f) Oligomerization or Polymerization (S. K. Patil & Lund, 2011), and (g) Diels Alder condensation (Laita, Boufi, & Gandini, 1997). Hydrogenation reaction target C=C and C=O bonds over properly selected catalyst into furfuryl alcohol and other related products matching fuel grade hydrocarbon (Mäki-Arvela, Hajek, Salmi, & Murzin, 2005; Ponec, 1997; Yu, Porosoff, & Chen, 2012). Once they are hydrogenated, they become prone to dehydration over acidic catalyst. Also, the C=C bonds produced by dehydration, are readily hydrogenated to give saturated alkyl chains. Therefore, dehydration and hydrogenation formally transforms C-OH group to C-H groups that is considered indirect hydrogenolysis (Dunlop, 1948). Hydrogenolysis of C-O via a non-dehydration and hydrogenation mechanism has been reported to be prominent for furfural though over selected catalysts. In this regard, Rh and Ir modified with ReO_x selectively dissociates C-O for the conversion of THF to 1,5-pentanediol (Koso *et al.*, 2009; Tucker *et al.*, 2012). However, rearrangement reaction yielding levunic acid otherwise known as 4-ketopentanoic acid from furfuryl alcohol of HMF is another class of furfural reaction (Hronec, Fulajtarová, & Liptaj, 2012; Hronec, Fulajtárova, & Mičušik, 2013). Decarbonylation is another type of reaction known as dissociation reaction that involves C-C dissociation. This reaction proceeds via adsorbed species on the metal surface where both furan ring and formyl group interact with the metal atoms to produce carbon monoxide (Pang & Medlin, 2011; Vorotnikov, Mpourmpakis, & Vlachos, 2012). In addition, Oligomerization or polymerization of furanic compound

University of Malaya

with furfural inclusive is prominent. Brown solids otherwise known as humin are as a result of polymerization of furfural in acidic media due to partial hydrogenation of furfural (Choura, Belgacem, & Gandini, 1996; S. K. Patil & Lund, 2011).

4-hydroxy-3-methoxybenzaldehyde conventionally known as vanillin (Fig 2.6), is an important flavor and aroma molecule having biogenetic relationship to the phenylypropanoid pathways and other molecules of physiological significance such as salicylate (Hocking, 1997; Walton, Mayer, & Narbad, 2003). It is used in food flavors, confectionery and beverages (~60%), perfume, cosmetics (~33%) and pharmaceuticals (~7%) (Priefert, Rabenhorst, & Steinbüchel, 2001). Notably, more than 12000 tons of vanillin are produced annually in global context, and <1% is natural, as they are majorly synthesized via a cheap chemical process in contrast to furfural which has no synthetic route of production (Lomascolo, Stentelaire, Asther, & Lesage-Meessen, 1999). However, the pathway formation of vanillin naturally is either from the coniferous as in softwood or the deciduous as in hardwood. The former produces 25% vanillin whiles the later mostly syringic aldehydes then vanillin via alkaline oxidation process. Most of the reaction path ways seen in furanic is also possible in vanillin compounds. Typically, biomass with appreciable coniferous and deciduous fragments produces bio-fuel with vanillin and that constitutes ageing challenge.

University of Malaya

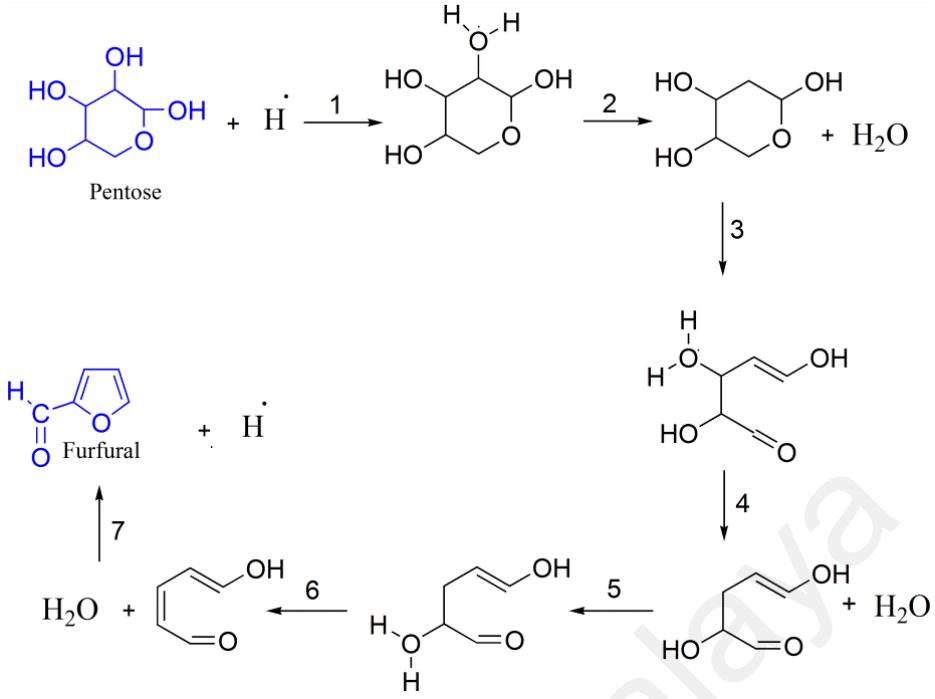

Fig. 2.5: The mechanism of dehydration of pentose to furfural (Zeitsch, 2000).

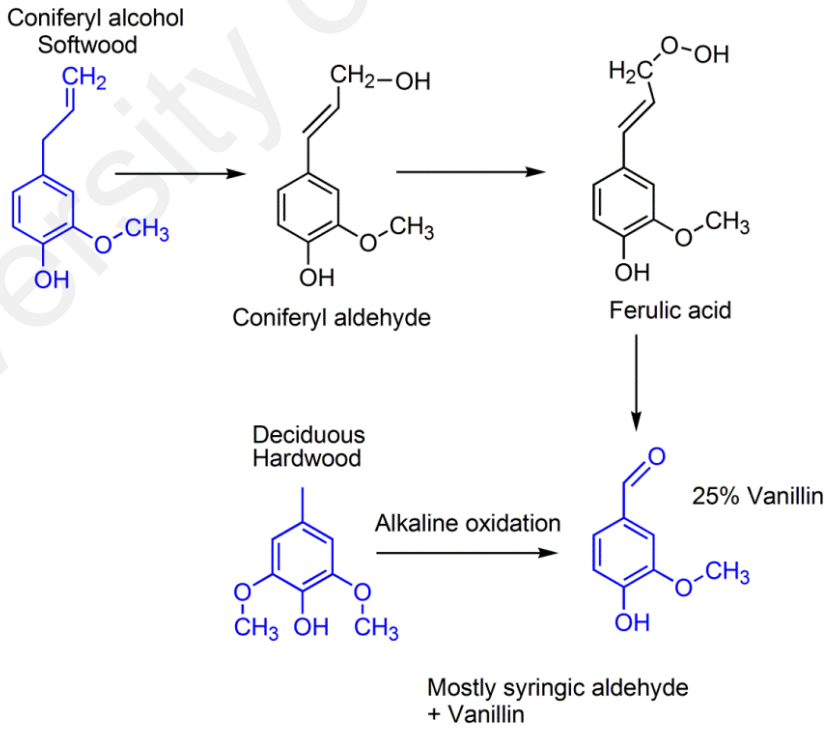

Fig. 2.6: Lignin conversion to vanillin (Hocking, 1997).

University of Malaya

According to the percent amount of pentosans as seen in Table 2.2 furfural production is more probable for these lignocellulose biomass in order of Corncobs > (all). Though bagasse, oat hulls, hazelnut shells, olive residue got high pentosan also.

Table 2.2: Potentials of different lignocellulose biomass for furfural production (Gebre, Fisha, Kindeya, & Gebremichal, 2015; Zeitsch, 2000)**.**

Lignocellulose biomass	Pentosans content
Bagasse	25-27%
Sunflower	25%
Rice Hulls	16-18%
Eucalyptus	20%
Pine wood	7-9%
Douglas fir wood	6
Spruce wood	11%
Oat Hulls	29-32%
Corncobs	30-32%
Almond husk	30
Hazelnut shells	23%
Residue of Olive extraction	21-23%
Balsa wood	18%
Beech wood	24%
Flax shives	23%

University of Malaya

Table 2.3: Comparison between lignocellulose derived bio-oil and crude oil. (Jacobson, Maheria, & Kumar Dalai, 2013; P. M. Mortensen, J. D. Grunwaldt, P. A. Jensen, K. G. Knudsen, & A. D. Jensen, 2011; R. H. Venderbosch, Ardiyanti, Wildschut, Oasmaa, & Heeres, 2010).

Properties	**Bio-oil**	**Crude oil**
Water (wt %)	15 – 30	0.1
pH	2.8 – 3.8	-
ρ (kg/l)	1.05 – 1.25	0.86
μ at 50 ^{0}C (cP)	40 – 100	180
HHV (MJ/kg)	16 – 19	44
Elemental and ash composition (wt %)		
C	55 – 65	83 – 86
O	28 – 40	< 1
H	5 – 7	11 – 14
S	< 0.05	< 4
N	< 0.4	< 1
Ash	< 0.2	0.1

University of Malaya

Table 2.4: Lignocellulose derived bio-oil production process via fast pyrolysis (Feeding Capacity of >1000kg/hr) (Isahak, Hisham, Yarmo, & Hin, 2012; Oasmaa, Van De Beld, Saari, Elliott, & Solantausta, 2015; Xiu & Shahbazi, 2012).

Organization	Country	Technology	Capacity (kg dry feed/hr)	Capacity (kg FRBO/h)	Application	Status
KiOR	USA	circulating fluidized bed,	20833	4542	bio-oil HDO	dormant
Genting	Malaysia	Rotating cone	2000	1200	fuel	dormant
ABRI Tech.	Canada	auger	2000		fuel	dormant
Fortum	Finland	Fluidized bed	10000	6313	fuel	operational
Ensyn Technologies	Canada	Circulating fluidized bed	2500	1720	fuel	operational
Red Arrow/Ensyn	USA	Circulating fluidized bed	1667	-	chemicals and fuel	operational
Red Arrow/Ensyn	USA	Circulating fluidized bed	1250	-	chemicals and fuel	operational
Ensyn Technologies	Canada	Circulating fluidized bed	625	-	chemicals and Fuel	operational
Ensyn/Fibria	Brazil	Circulating fluidized bed	16667	11470	fuel	In design phase
BTG BioLiquids/ EMPYRO	Netherlands	Rotating cone	5000	3200	fuel	commissioning

University of Malaya

Table 2.5: Lignocellulose derived bio-oil production process via fast pyrolysis (Feeding Capacity of 100-1000kg/hr).

KiOR	USA	Circulating fluidized bed,	417	-	bio-oil HDO	dormant
Biomass Engineering Ltd	UK	Fluidized bed	250	-	fuel and chemicals	dormant
Pytec	Germany	ablative	250	-	fuel	dormant
Virginia Tech	USA	Fluidized bed	250		fuel	dormant
Agri-Therm.University of western ontario	Canada	Fluidized bed (mobile)	420	-	chemical feedstock	operational
BTG	The Netherlands	Rotating cone	200	150	fuel and chemicals	operational
Valmet	Finland	Fluidized bed	300	-	fuel	operational
Fraunhofer UMSICHT	Germany	ablative	100	-	fuel and chemicals	commission

University of Malaya

Table 2.6: physicochemical properties some lignocellulose biomass derived bio-oil.

Biomass	Reactor Temp (K)	Oil yield (wt %)	RT (min)	Viscosity (cSt)	Solid (wt %)	PP	FP	Ref.
Wheat straw	Fluidized bed	-	-	50	0.30	-9	>106	(Sipilä *et al.*, 1998)
Rapeseed	Heinze	46.0	30	43	-	80	-	(S Şensöz *et al.*, 2000)
Microalgae	Fixed bed	17-27	2-3	0.1	-	-	-	(Miao *et al.*, 2004)
Sesame	Fixed bed	37.2	30	-	-		-	(Ateş *et al.*, 2004)
Bagasse	Vacuum	43	-	89	-	105	-24	(Islam *et al.*, 2005)
Sunflower	Fixed bed	48	0.5	-	-	-	-	(Gerçel, 2002)
Olive bagasse	Fixed bed	16	-	0.1	-	-	77	(Sevgi Şensöz *et al.*, 2006)
Rice straw	Fluidize bed	-	2-6	-	0.1	-	-	(D. C. Elliott, 2001)

PP = pour point, FP = flash point, HHV = highest heat value, LHV = lowest heat value

University of Malaya

2.3.1 Hydro-processing of lignocellulose derived bio-oil

Hydro-processing is a process of treating specific fossil or bio-fuel functionalities in presence of hydrogen into fuel grade molecules or platform chemicals. It is one of the best methods that have been employed to upgrade Bio-oil to fuel grade hydrocarbon. In this case, this process typically targets phenolic, aldehydes oxygenates in bio-oil by breaking aromatic–O, O–CH_3 bond (de-methylation) and also nucleophilic H_2 addition on R-C=O. In some instances such as hydro-denitrification, hydro-desulfurization, hydro-demetallization and so on, removal of nitrogen compounds, sulfur, metals are the main interest (Lee, Gu, Mullen, Boateng, & Vlachos, 2015; Lu & Heyden, 2015; Martinez, Alvarez, Aguirre, & Subramanian, 1986; Nakagawa, Takada, Tamura, & Tomishige, 2014; Nakagawa, Tamura, & Tomishige, 2013; Sitthisa, Sooknoi, Ma, Balbuena, & Resasco, 2011). There are number of process which falls in this category though two major classifications; hydro-treating and hydrocracking have been evidenced also (Bej, 2002; Elliott, Neuenschwander, & Hart, 2013; Patil, Armbruster, Richter, & Martin, 2011). Hydro-treating involves hydro-denitrification, mild and total hydrogenation hydro-demetallization, hydro-desulfurization, hydro-deoxygenation, and hydro-isomerization. These processes are kinetically facile with the aid of solid catalyst.

2.3.2 Alcoholic and cyclic fuel grade hydrocarbon as products of hydro-processing

The four aliphatic alcohol methanol, ethanol, propanol and butanol have been used as fuel because of their ease synthesis. Additionally, alcohol group has higher octane number than regular gasoline and therefore implies it can endure higher compression ratios before engine starts knocking. This gives engine an ability to deliver more power efficiently and economically by burning cleaner than regular gasoline and produces lesser CO, HC and NOx (Guerrieri, Caffrey, & Rao, 1995; Kim & Dale, 2005; Taylor *et al.,* 1996). Also, due to higher heat of vaporization of alcohol, peak temperature inside

University of Malaya

combustion chambers is reduced leading to lower NOx emission that makes engine power to increase. However, converting bio-oil aldehyde components such as furfural and vanillin to alcoholic components such as furfuryl alcohol or vanillyl alcohol have been reported by many researchers. This will add positive alcohol attributes for upgrading bio-oil.

2.3.3 Quantum scale consideration in hydro-processing

Considering that hydro-processing steps proceed via a metal function and acid function where necessary, metal with higher electronegativity has more covalent character of the metal oxide bond (Tamura, Shimizu, & Satsuma, 2012). In this case, electronegativity of some metal are in the order; $Fe^{3+} >> Cu^{2+} > Ni^{2+} > Co^{2+} > Ru^{3+}$ (Brozek & Dincă, 2014). Hydro-processing of bio-oil oxygenates for instance involves typical adsorption on these metal oxide (M-O) surfaces as well as adsorption on metal surface likewise. The variation on adsorption energy for hydrogen on metal surfaces varies with different metals according to their respective electronic structure. In this regard the transition metal employed for these processes, coupling between the adsorbate valence states and the metal d-states largely describes the disparities (Gajdoš, Eichler, & Hafner, 2004; Hammer & Norskov, 1995; Mavrikakis, Hammer, & Nørskov, 1998; Nilsson *et al.,* 2005). The rule therefore is that the higher the energy of the d-states relative to highest occupied states of the metal, the stronger the interaction with adsorbate states in this case likely bio-oil oxygenate. This is because when the d-states are close to the Fermi energy and antibonding states can be shifted well above it and becomes empty or bonding states can be shifted below it and become occupied (Nørskov, Bligaard, Rossmeisl, & Christensen, 2009).

In accordance to the background seen so far, there are different schools of thought considering adsorption of hydrogen and bio-oil oxygenate onto metal oxide surface. The

University of Malaya

classical view had a conjecture that due to exchange of Deuterium, then hydrogen spill over is prominent. The recent view claimed spillover of hydrogen is dependent on carrier nature being reducible or non-reducible. In the former case, there are no substantial justifications to prove that. But in the latter case, justifications were made that it is energetically highly unlikely for a non-reducible support to spill hydrogen. However, the support material Lewis acid site could contribute to possible adsorption of organic substrate on the surface (Han, Jung, Jung, Choi, & Park, 2012; Lykhach *et al.*, 2012; Prins, 2012).

Bio-oil upgrade to fuel grade hydrocarbon otherwise known as biofuel through bio-refinery operation involve two major factors such as catalyst and reactor. Table 2.8, 2.9, 2.10 and 2.11 present some recent studies on both liquid and vapor phase hydrogenation considering furfural and other bio-oil oxygenates that renders it having low energy density. The catalysts therein employ a metal function as well as acid functions (Lewis and Bronsted) in specifically targeting carbonyl and aromatic functionalities. These catalysts have a major drawback of using chromium and tin which has been marked to have health and environmental challenges. Moreover, they all have low recoverability.

2.3.4 Importance of hydrogen solubility in hydro-processing reaction

Hydrogen solubility in reacting phase media is the major requirement and issues that guides hydro-processing of bio-oil feedstock into fuel grade hydrocarbon or platform chemicals. The determination of solubility of hydrogen necessitates the use of equation of state, fugacity or other thermodynamic correlation of which their data may not exist at required hydro-processing conditions. This is very important when considering the molecular diffusion of hydrogen toward the metal-function and subsequent activation of the bio-oil functionality. At research level, the solubility of hydrogen in 10 different solvent has been evidenced by Erwin Brunner (Brunner, 1985) using the classical

University of Malaya

approach: ln x_2^o-Δ H_2(RT+ΔS_2/R) where x_2^o is the solubility and ΔH_2 and ΔS_2 enthalpy and entropy independent on temperature changes on transfer of 1 mol of H_2 from the gas phase at 101.325 kPa to the infinitely diluted solution. R is the gas constant taken to be 8.31441 J/kmol data based on this calculation for hydrogen solubility in different solvent is seen in table 2.7.

Table 2.7: Mole fraction solubility of hydrogen at 101.3 kPa in different solvents.

Solvents	**H_2 Solubities 104Xo**	**Temperature K**	**Δ H_2^a kJ/mol**	**ΔS_2^b kJ/mol.K**
	7.13	298.15		
n-Hexane	8.20	323.15	5.134	43.09
	10.7	373.15		
	6.76	298.15		
n-Octane	7.88	323.15	4.494	45.57
	9.75	373.15		
	6.73	298.15		
n-Decane	8.00	323.15	5.105	43.56
	10.2	373.15		
	3.15	298.15		
Toluene	3.75	323.15	5.773	47.68
	5.05	373.15		
	1.78	298.15		
Acetonitrile	2.16	323.15	6.794	45.06
	3.02	373.15		
	2.87	298.15		
Acetone	3.50	323.15	6.539	49.89
	4.97	373.15		
	2.70	298.15		
Tetrahydrofuran	3.30	323.15	6.888	45.26
	4.71	373.15		

University of Malaya

	1.84	298.15		
Dioxane	2.28	323.15	7.176	47.46
	3.29	373.15		
	1.47	298.15		
N-N Dimethylformamide	1.83	323.15	6.729	50.78
	2.54	373.15		

a = Enthalpy of solution & b = Entropy of solution data obtained from literature (Brunner, 1985; Elliott *et al.,* 2012; Purwanto, Deshpande, Chaudhari, & Delmas, 1996).

University of Malaya

Table 2.8: Vapour phase hydrogenation of furfural to furfuryl alcohol.

Feed	Product	Performance		Conventional Non- magnetic Catalyst	Process parameter	References
		Sel.%	C. %			
Furfural	Furfural alcohol	98	53	Cu-Cr	0.1Mpa, 533K, 0.3g cat	(Seo & Chon, 1981)
Furfural	Furfural alcohol	98	98	Cu/MgO	0.1Mpa, H_2/Furfural=2.5, GHSV 0.05mol $h^{-1}g_{cat}^{-1}$, 453K	(Nagaraja *et al.,* 2003)
Furfural	Furfural alcohol	98	100	Cu-Ca/SiO_2	0.1Mpa, H_2/Furfural= 5, LHSV 0.33 mL h^{-1} mL_{cat}^{-1}, 403K,	(Wu *et al*., 2005)
Furfural	Furfural alcohol	>99	98	CuLa/MCM-41	0.1Mpa, H_2/Furfural= 5, GHSV 0.087mol $h^{-1}g_{cat}^{-1}$, 413K,	(Ying Hao, Zhou, Wang, Zhang, & Liu, 2005)
Furfural	Furfural alcohol	88	90	Cu-Cr/TiO_2	0.1Mpa, H_2/Furfural= 3, GHSV 0.04mol $h^{-1}g_{cat}^{-1}$, 413K,	(W. Huang *et al.,* 2007)
Furfural	Furfural alcohol	87	91	Pt/TiO_2-V_2O_5-SiO_2	0.1Mpa, H_2/Furfural= 2, LHSV 2 g/hg_{cat}, 423K,	(Kijeński, Winiarek, Paryjczak, Lewicki, & Mikołajska, 2002)

University of Malaya

Table 2.9: Liquid phase hydrogenation of furfural to furfuryl alcohol.

Feed	Product	Performance		Conventional Catalyst	Process parameter	References
		Sel. %	C. %			
Furfural	Furfural alcohol	96	>99	Cu-Zn-Cr-Zr oxide	14g Fur, 88g iPrOH sol,1.5g cat, 2Mpa, 443 K, 3.5 H	(Sharma, Das, Sammynaiken, & Dalai, 2013)
Furfural	Furfural alcohol	99	98	Raney Ni-$CuPMo_{12}$	12g Fur, 8g EtOH sol,0.5g cat, 2Mpa, 353 K, 1 hr	(Baijun, Lianhai, Bingchun, Tianxi, & Iwatani, 1998)
Furfural	Furfural alcohol	100	> 99	Co-Mo-B alloy	12g Fur, 71g EtOH sol,2g cat, 1Mpa, 373 K, 3 hr	(Chen, Li, Luo, & Qiao, 2002)
Furfural	Furfural alcohol	98	90	Pt-Sn/SiO_2	2.3g Fur, 40g iPrOH sol,0.25g cat, 1Mpa, 373 K, 8 hr	(Vetere, & Ruggera, 2009)
Furfural	Furfural alcohol	100	97	Ni-Fe-B alloy	12g Fur, 24g EtOH sol,1g cat, 1Mpa, 373 K, 4 hr	(Li, Luo, Zhuang, Dai, & Qiao, 2003)
Furfural	Furfural alcohol	>96	>96	Cu-Fe oxide	2.4g Fur, 3.5g Octane sol,0.2g cat, 9Mpa, 433 K, 5 hr	(Yan, Liao, Wu, & Xie, 2013)

University of Malaya

Table 2.10: Liquid and vapour total hydrogenation of furfural.

Feed	Product	Performance		Conventional Catalyst	Process parameter	References
		Sel. %	C. %			
Furfural	THFA	76	>99	RuO_2	14g Fur, 88g iPrOH sol, 1.5g cat, 2Mpa, 443 K, 3.5 H	(Khairi, Hara, Ichikuni, & Shimazu, 2012)
Furfural	BHTHF	99	98	Raney Ni	12g Fur, 8g EtOH sol,0.5g cat, 2Mpa, 353 K, 1 hr	(Connolly *et al.*, 2010)
Furfural	THFA	100	>99	Ni-Pd/SiO_2	12g Fur, 71g EtOH sol,2g cat, 1Mpa, 373 K, 3 hr	(Nakagawa & Tomishige, 2010)

Table 2.11: Catalyst and conditions for hydro-processing of different bio-feed derived from lignocellulose biomass.

Feed	Product	Catalyst	Process condition	References
Furfural	Fuel grade hydrocarbon	Ni/CNTs	Batch., 150-300^{o}C, 4hr	(Elliott & Hart, 2008; Lessard, Morin, Wehrung, Magnin, & Chornet, 2010; Tike & Mahajani, 2007)
		Ru/C	Batch., 40-90^{o}C; 6.8-40.8bar; 1hr	
		Cu/Fe etc	Batch., 252^{o}C; 90 bar; 14 hrs	
	Fuel grade hydrocarbon	S-Ru/C,	Cont., 170^{o}C; 13.7Mpa	(Ardiyanti, Gutierrez, Honkela, Krause, & Heeres, 2011; Elliott *et*

University of Malaya

Pyrolysis oil		Ru/C, Ru/TiO_2, Ru/Al_2O_3,Pt/C, Pd/C Rh, Pt and Pd on ZrO_2	Batch., 350^oC; 20Mpa Batch., 350^oC; 20Mpa	*al.,* 2012; Venderbosch & Heeres, 2011)
Lignin	Fuel grade hydrocarbon	US&SS Co(Ni)Mo(W)	Auto.; 270^oC and 400^oC, 13Mpa	(Bridgwater, 2011)
Lignin derived guaiacol	Fuel grade hydrocarbon	US&S MoS_2 MoS_2/AC Pt/Al_2O_3, Hβ zeolite and MgO Rh, Pt, Pd on ZrO_2 Bifunctional Pt. Rh, Ru, Pd/Al_2O_3& SiO_2-Al_2O_3 Ni_2P{, Fe_2P, MoP, Co_2P, Wp on SiO_2 Mo_2N/C Mo_2N/Al_2O_3 &SBA15 Ni-Cu on γ-Al_2O_3, SiO_2, SiO_2-ZrO_2, La_2O_3 and CeO_2-ZrO_2	Cont., 300^oC; 4Mpa Batch., 300^oC; 5Mpa Cont., 300^oC; near atm. Batch., 330^oC; 8Mpa Batch., 250^oC; 4Mpa Cont., 300^oC; 1.5Mpa	(Bykova *et al.,* 2012; Genuit, Afanasiev, & Vrinat, 2005; Ghampson *et al.*, 2012; Lee *et al.,* 2012; Lin, Li, Wan, Lee, & Liu, 2011; Ruiz *et al.,* 2012; Runnebaum, Nimmanwudipong, Block, & Gates, 2011; Zhao, Li, Bui, & Oyama, 2011)

US = Un-sulfided, S = Sulfided

University of Malaya

2.4 Overview on heterogeneous catalysts

2.4.1 Statistical outlook

The drives that make heterogeneous catalysis viable to take the largest market share as shown in Fig 2.7 are consumer demands, environmental and energy legislation. Dated up to 2015 records, global market share for different classes of catalysts had three major interested areas of catalytic applications while mobile emission control takes the largest share. Heterogeneous catalyst option is gaining more recognition and at 2015, its demand rose by 20.4% more than others in 2010.

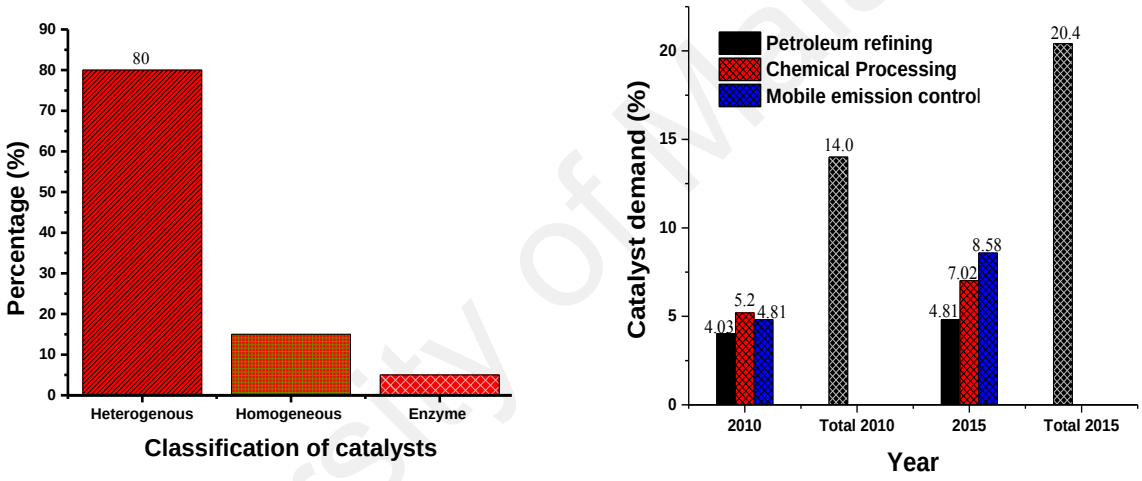

Fig. 2.7: Global market share for different class of catalysts (Baerns, 2013).

2.4.2 Catalyst design and synthesis

Understanding catalyst design-synthesis-structure-activity relationships in association with trial and error, empiricism and serendipity, is the key to promising and novel heterogeneous catalysis. Catalytic systems considers single and multiple reaction systems that operates at isothermal and non-isothermal conditions either in pellets, monolith, fixed bed reactors or membrane reactors. The relationship on catalyst physicochemical properties-operating parameters to gain insight into the underlying phenomena governing its performance is the basic step which needs to be investigated (Faba, Díaz, & Ordóñez, 2015). These catalysts are broadly classified into two

University of Malaya

categories as those with magnetic anisotropy and those without magnetic anisotropy. Basically the design parameter for conventional non-magnetic catalysts for instance includes; textural properties such as catalyst shape, surface area, pore size, pore diameter pore volume, crystallite size and particle size (Mohammadzadeh & Zamaniyan, 2002). Also for porous catalysts, evaluation of Thiele modulus could reveal the catalyst supremacy to mass transfer issues. In addition, quantum scale properties such as oxidation states also exist to improve the outstanding capacities of the catalyst (Norskov, Bligaard, Rossmeisl, & Christensen, 2009).

2.4.3 Conventional catalysts

Conventional catalysts as the name implies is traditional based that centers on the recoverability premise. These include sulfided, non-sulfided, noble metal and non-noble metals that have been employed for hydro-processing reactions among others. Sulfided CoMo, NiMo, Mo supported on γ-Al_2O_3 or Al_2O_3-SiO_2 have been tested for hydro-desulfurization of petroleum products and lignin to fuel grade molecules (Horáček, Homola, Kubičková, & Kubička, 2012), (Maugé, Vallet, Bachelier, Duchet, & Lavalley, 1996). In this case, Ni and Co promotes the active Mo and sulfur vacancies on MoO_2 guides adsorption of reactive species on it. The draw back with sulfided structures is low stability at extreme hydro-processing conditions. Non-sulfided such as transition (non-noble) metals catalysts (Ni, Mo, Fe, Co, W, and oxide form of W and Mo among others have been studied as alternative to the noble metal catalysts because of their low cost and are readily available. Noble metals such as Ru, Pd, Pt, and Rh have high electronegativity as compared to non-noble metals such as Ni and their usage is associated with high cost, inspite the observed potential activities. In as much as conventional catalysts have their numerous credits, one fact cannot be ruled out as their major drawback, and that is their non-magnetic nature that makes them to have low recovery.

University of Malaya

2.4.4 Magnetic catalysts

Magnetic catalysts are considered in this section against the drawbacks of the conventional catalysts. Conventional catalyst as seen earlier have two major disadvantages; low recoverability, non-biocompatible. This makes them potentially harmful to the environment, in contrast, magnetic catalysts displays advantages in term of recoverability and bio-compatibility (Ahmadi, Zhang, Gong, Zhu, & Sun, 2016). In line with techno-economic considerations, magnetic catalysts are superior to non-magnetic catalyst. The prominent among them is the iron oxide nanoparticle (IONP) that appears in different forms with distinct magnetic properties. Basically three types of IONP such as magnetite (Fe_3O_4 of $FeOFe_2O_3$), maghemite (γ-Fe_2O_3) and hematite (α-Fe_2O_3) are renowned. Their magnetic properties decreases in this order; Fe_3O_4 > γ-Fe_2O_3 > α-Fe_2O_3 (Lowrie, 1990). The magnetic property is seen in terms of magnetization of material and refers to the amount of individual magnetic moments within the material that are aligned when field is applied. It can also be seen in terms of magnetic susceptibility (X = M emu/g/H, G) as a quantitative measure of the response. Therefore, different materials get attracted to the field and are termed paramagnetic while others are slightly attracted and are termed diamagnetic. Consequently, the total magnetic susceptibility of material is the summation of the paramagnetic magnetic susceptibility (X_p) and diamagnetic susceptibility (X_d). These materials are classified under the auspices of molecular magnetism as against atomic based magnetism. This is because their magnetic moments resides on d or f orbitals and either magnetic spins located in s and/or p orbitals or molecular orbitals mediate the magnetic interaction. Conversely atom based magnetism are defined by the presence of magnetic moments which reside on d or f orbitals of transition or lanthanide metals with extended bonding in at least two dimensions. This is the main reason why atomic based magnetism are prepared via metallurgy at extreme conditions while molecular magnetism are prepared

University of Malaya

at low-temperature process incorporating a combination of organic, organometallic and co-ordination metal chemistry. Catalyst size affects the magnetic property of the catalytic material. For instance, $r_o = (6k_BT_B/K)^{1/3}$ where, r_o is the transition point from super paramagnetic to single domain, k_B is the Boltzmann constant, T_B is the blocking temperature and K is an anisotropy constant. In addition, Table 2.12, 2.13 shows size, shape, composition, shell-core as basic design parameter that influences magnetic property of some materials.

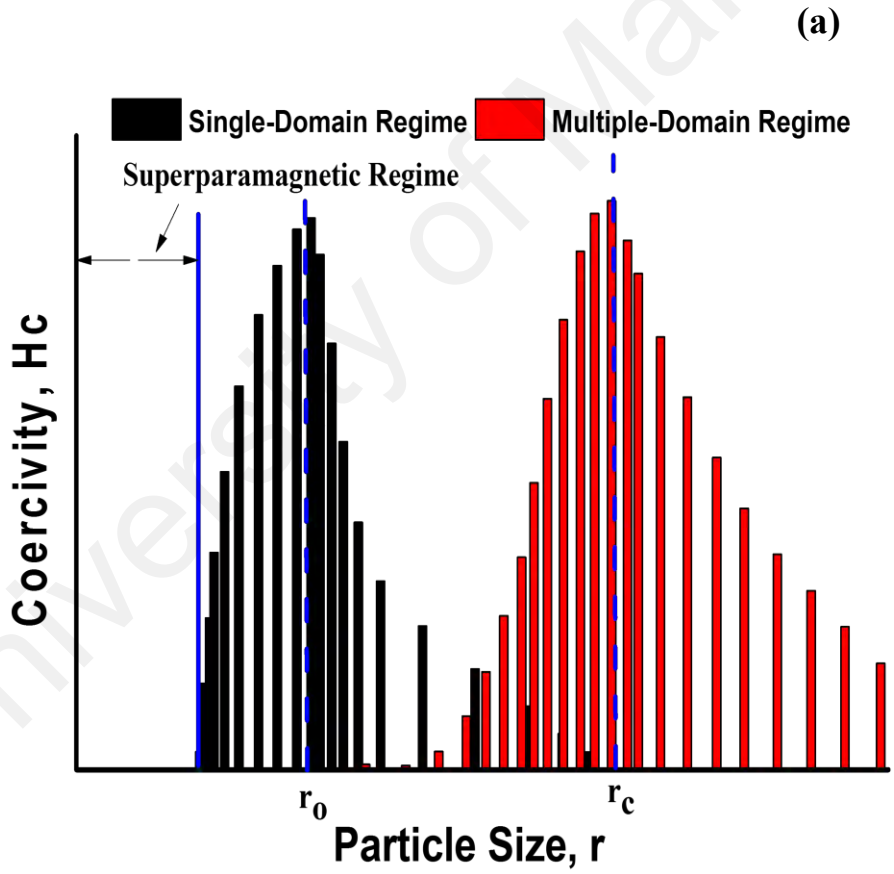

University of Malaya

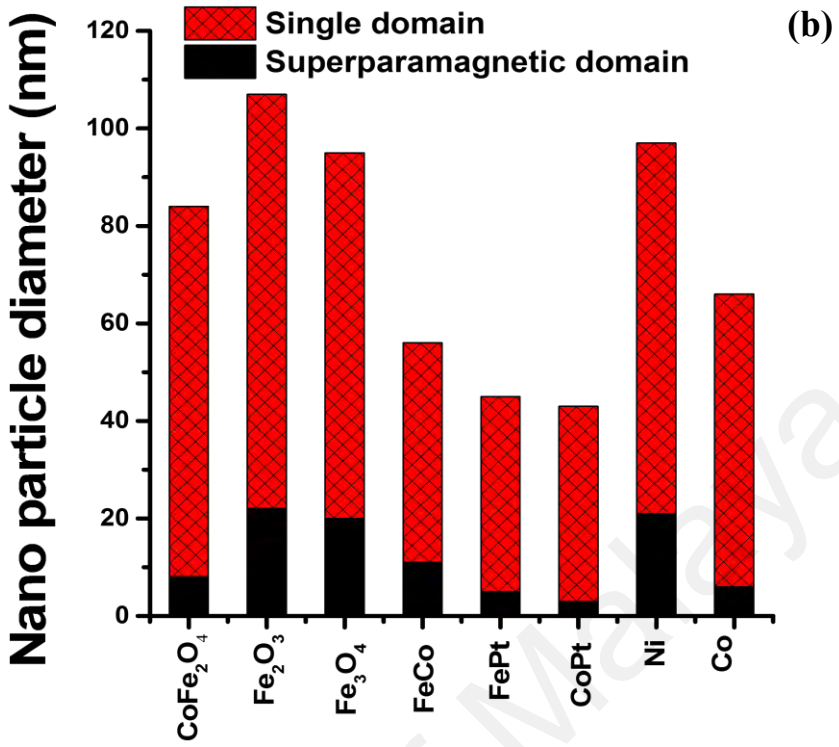

Fig. 2.8: Size effect on magnetic characteristics (a) Magnetic domain with size (Jeong, Teng, Wang, Yang, & Xia, 2007) (b) Different magnetic material with their magnetic domains as a function of size (Krishnan, 2010).

Table 2.12: Size as a design parameter for different magnetic materials.

Magnetic Nanoparticle	Size (nm)	Magnetic parameter			References
		Ms (emu/g)	Coercivity (G)	Tb (K)	
Fe_3O_4	6.60	71.00	16.00	203.00	(Caruntu, Caruntu, & O'Connor, 2007)
	11.60	77.00	15.00	264.00	
	17.80	83.00	3.00	>300.00	
Fe_3O_4	4.20	75.00	318.00	19.00	(Noh *et al.*, 2012)
	7.40	70.00	270.00	28.00	
	8.10	65.00	70.00	49.00	
	17.00	82.00	364.00	275.00	

University of Malaya

	45.00	92.00	340.00	275.00	
Fe_3O_4	4.90	60.40	-	33.90	(Pereira *et al.*, 2012)
	6.30	64.80	-	56.20	
	8.60	58.00	-	96.00	
$CoFe_2O_4$	4.20	30.60	-	89.40	(Pereira *et al.*, 2012)
	4.80	46.00	-	149.20	
	18.60	48.80	-	286.40	
$CoFe_2O_4$	2.80	30.60	-	89.40	(Peddis *et al.*, 2008)
	2.90	46.00	-	149.20	
	6.70	48.80	-	286.40	
$MnFe_2O_4$	9.30	57.10	-	397.70	(Pereira *et al.*, 2012)
	11.70	54.60	-	91.00	
	59.50	35.20	-	96.60	
$HoMnO_3$	30.00	0.30	382.00	50.00	(T. Han, Tsai, & Wei, 2011)
	200.00	0.10	0.00	70.00	

Table 2.13: Size and shape as a design parameter for different magnetic material.

Magnetic Nanoparticle	Shape	Size (nm)	Ms (emu/g)	Coercivity (G)	TB
Fe_3O_4 with γFe_2O_3	Cube	12	40	0	-
	Rod	12	18	4.4	-
	Sphere	12	80	0	-
	Octahedron	12	80	0	-
γFe_2O_3	Sphere	14	75	30	235
	Cube	12	75	33	190
Fe_3O_4	Cube	8	40	0	60
	Sphere	8.5	31	0	100
FePt	Cube	11.8	2.5	164	50
	Octopod	12	2.0	1461	95
	Cuboctahedron	6.8	0.1	11	20
$CoFe_2O_4$	Sphere	10	80	16000	275
	Cube	8	80	9500	275

University of Malaya

2.4.5 Economic impact of molecular modeling and simulation to catalysts development for energy application

The economic impact of molecular modeling in context of catalyst development for energy application extends a platform for developing new materials whose properties are yet to be explored. This increases the know-how and stronger focus in industry. Molecular modeling describes behavior of material at atomistic or molecular level in contrast to continuum-based modeling where atomistic level phenomena are neglected (Maginn, 2009). In line with the above background, the economic impact depends on the levels of the material as shown in Fig 2.9 (bulk materials and engineering, self-organized structures, molecular structures and electronic process). This is expanded on the material are first design structurally, then molecular minimization using molecular mechanics and then conformational analysis of the molecule (Ringan & Grayson, 1994)

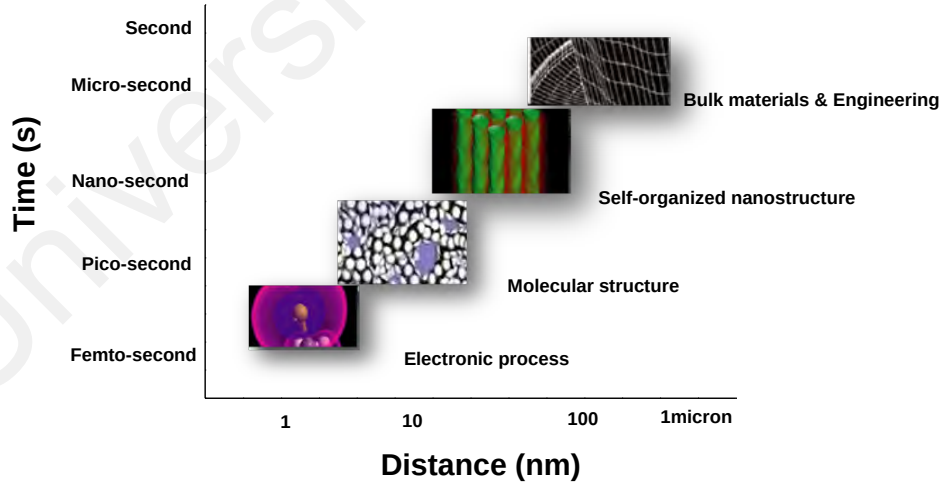

Fig. 2.9: Multi-scale modeling schematics (Ringan & Grayson, 1994)

University of Malaya

CHAPTER 3: MATERIALS AND METHODS/METHODOLOGY

3.1 Research Materials

All chemicals were purchased from Merck Millipore and Chemo-lab Malaysia. Detail outline is given in table 3.1.

Table 3.1: Some chemicals used for the research study.

S/N		Brand		Purity w/w %
	Precursors			
1	Iron III chloride hexahydrate	R&M		99
2	Iron II chloride tetrahydrate	R&M		99
3	Nickel II nitrate hexahydrate	Sigma Aldrich		99
4	Ruthenium chloride	R&M		99
5	Tetraethyl orthosilicate	Aldrich		98
	Reactants			
1	Furfural	R&M		99
2	Vanillin	Merck		99
	Some solvents			
1	Heptane	Riendemann chemicals	Schimdt	99
2	Ammonia	Riendemann chemicals	Schimdt	25
3	Acetone	Emsure		98
4	Ethanol	Riendemann chemicals	Schimdt	99

3.2 Equipments

The equipment associated with the catalyst synthesis includes; Wisestire hotplate stirrer with digital timer function feedback control, Nabertherm furnace; static environment with automatic temperature controller, and Carbolite furnace; dynamic environment with automatic temperature controller. The equipment used for studying physical properties of the catalyst includes; Lakeshore 7400 series, 7407 model with 7 inch electromagnet vibrating sample magnetometer (VSM), Micrometrics TriStar II 3020 adsorption apparatus, JEOL JEM-3010 HRTEM and FEI Quanta 400 FESEM. Those isolated for the catalyst chemical property includes; TPDRO 1100 series setup

University of Malaya

equipped with a thermal conductive detector, einishaw InVia Raman spectroscope, Bruker S4-Explorer X-ray fluorescence and X-ray photoelectron spectroscope; ULVAC-PHI Quantera II with a 32-channel spherical capacitor energy analyzer under vacuum (1 x 10-6 Pa).

3.3 Theory and experimentation

3.3.1 Catalyst design and molecular modeling

A simple repeating unit of the magnetic catalyst molecule was built based on the design constrain of producing magnetic nanomaterial within the super paramagnetic domain (< 20 nm). This was achieved on Gaussian 09 computational platform using mechanics method and universal force field (UFF) functional. Prior vibrational spectroscopy analysis of the catalyst major linkages was recorded as a guide for the experimental synthesis process and manipulation to the catalyst surface atom structural periodicity for outstanding performance.

3.3.2 Catalyst preparation

Magnetic $Fe(MFe)O_4$-SiO_2 nanoparticle catalyst was synthesized through the facile co-precipitation method at ambient condition. In the typical synthesis procedure, aqueous solution of $FeCl_3.6H_2O$ and $FeCl_2.4H_2O$ in ratio of 3:2 was prepared to generate in-situ magnetic nanoferrite at pH 10 using NH_3 aq. The resulting mixture was stirred at 600rpm for 1h followed by adding 15 wt % TEOS, and then stirred further for 24h. Afterwards, an aqueous solution of M, (M = Ni from $Ni(NO_3).6H_2O$ or Ru from $RuCl_3$) was introduced dropwise and the pH was adjusted to ~10. The overall mixture was stirred at 600rpm for 12h until $Fe(MFe)O_4$-SiO_2 was formed. The resulting catalyst was washed with deionized water and then with HCl and finally with acetone to exclude all necessary impurities. Finally, the catalyst was dried at 60 ^oC at 1^oC/min ramping in static environment. Fig 3.1 presents synopsis of the catalyst synthesis process.

University of Malaya

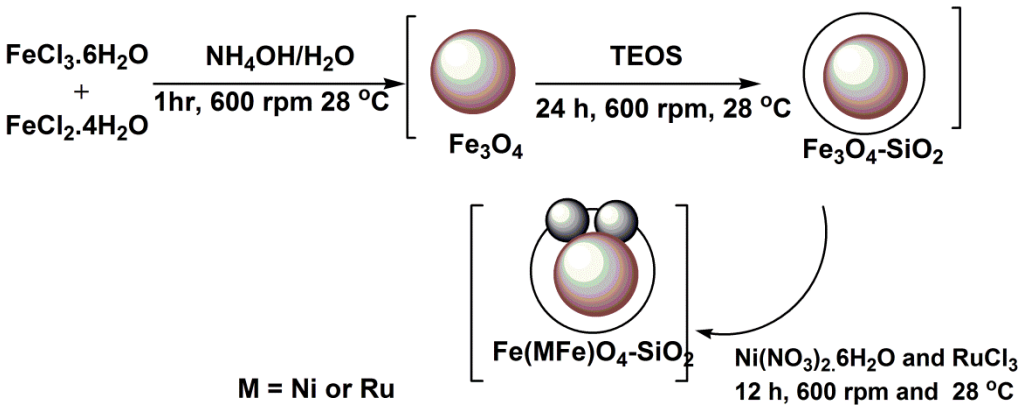

Fig. 3.1: One-pot synthesis of the magnetic $Fe(MFe)O_4{-}SiO_2$ nanoparticles catalyst.

3.3.3 Catalyst characterization

Thermal gravimetric and differential thermal analysis (TG-DTA) of the dried $Fe(MFe)O_4$-SiO_2 catalyst was performed using Perkin Elmer with 10 ^oC/min ramping. The magnetic properties of $Fe(MFe)O_4$-SiO_2 and bulk NiO as well as RuO_3 samples were measured using a Lakeshore 7400 series, 7407 model with a 7 in. electromagnet vibrating sample magnetometer (VSM). The analysis was conducted at room temperature in the field sweeping from - 10 kOe to + 10 kOe. The N_2 adsorption-desorption studies were done on Micrometrics TriStar II 3020 BET apparatus using ASTM D 3663-03 test method. The H_2 temperature programmed reduction (H_2-TPR) analysis was conducted on TPDRO 1100 series equipped with a thermal conductivity detector. Approximately 50 mg of $Fe(MFe)O_4$-SiO_2 sample was heated up to 120 ^oC at 10 ^oC/min ramping in 20 mL/min flowing N_2 for 30 min. The sample was then switched to 25 % H_2/ N_2 (V/V, 20mL/min) mixture and heated at 10 ^oC/min ramping to 700 ^oC max for 1h and then cooled to room temperature. Fourier transform infrared (FT-IR) spectra of $Fe(MFe)O_4$-SiO_2 as well as NiO and RuO_3 were measured at range 400 cm^{-1} to 4000 cm^{-1} wavelength region on Bruker FTIR IFS 66/S with a resolution of 4 cm^{-1}. This was complimented further with Raman measurement on Reinishaw InVia Raman spectroscope with 514 nm excitation sources of Ar^+ laser and 0.01Mv power. X-ray fluorescence (XRF) analysis of the catalyst sample was done on Bruker S4-

University of Malaya

Explorer. Powder X-ray diffraction (XRD) analyses were conducted on Bruker D8 advance instrument operated at room temperature with Cu Kα radiation and X-ray wavelength of 1.5406 Å. The Bragg's angle range was set from 10 to 80 ^{o} with a step size of 0.03 ^{o} and an acquisition time of 1s/step at 40 kV and 40 mA. The catalyst surface morphology was analyzed with atomic force microscope (AFM) on Bruker Nano-scope V Multimode 8, field emission scanning electron microscopy (FESEM) on FEI Quanta 400 and JEOL JEM-3010 High resolution transmission electron microscopy (HRTEM). Ammonia desorption analysis was performed employing a conventional TCD±TPD equipment using 200 mg catalyst. The samples were activated inside the TPD reactor at 400 ^{o}C for 1 h, followed by adsorption of ammonia at 150 ^{o}C in order to diminish the extent of physical adsorption. Besides this caution, a further removal of still physically adsorbed ammonia was carried out by purging the sample at 150 ^{o}C for 48 h at 30 cm^3/min.h of high purity helium (99.9999 %). The H_2-temperature programmed reduction (H_2-TPR) analysis was conducted on TPDRO 1100 series setup (Fig. 3.2b) equipped with a thermal conductive detector. Approximately 50 mg of the Fe(MFe)O_4-SiO_2 sample was heated up to 120 °C at a rate of 10 °C/min in N_2 (20 mL/min) for 30 min to make it water free. The sample was then switched to a 25% H_2/N_2 (V/V, 20 mL/min) mixture and then cooled to room temperature. The measurements were carried out in a N_2 environment at a programmed temperature up to 700 °C at a rate of 10 °C/min. TPD of ammonia was performed by heating the sample from 150 ^{o}C up to 600 ^{0}C, at 10 ^{o}C/min rates and under 30 cm^3/min helium flow rate. Finally, X-ray photoelectron spectroscopy (XPS) analysis of Fe(MFe)O_4-SiO_2 catalyst was studied on ULVAC-PHI Quantera II with a 32-channel spherical capacitor energy analyzer under vacuum (1 x 10-6 Pa) using Monochromatic Al Kα radiation (1486.8eV) and natural energy width of 680meV.

University of Malaya

3.3.4 Catalyst activation

The $Fe(MFe)O_4$-SiO_2 catalyst was activated on CRD multiple parallel pretreatment system with capacity of 240 mg/capsule encapsulating unit (Fig. 3.2a). The unit was operated maximum at 600 ^oC and modulated via an ESA VT60 temperature controller along with 5 bars maximum pressure controlled work station. The gas line was primed with N_2 for 30 min to ensure air free environment. In a typical experiment, 60 mg of $Fe(MFe)O_4$-SiO_2 magnetic catalyst was activated at 500 ^oC, 1 ^oC/min ramping for 3h under 10 mL/min H_2 flow. The activation condition in this case is in accordance with the reduction conversion factor obtained from TPR experiments using 50 mg of $Fe(MFe)O_4$-SiO_2 at 448 ^oC maximum for 1h.

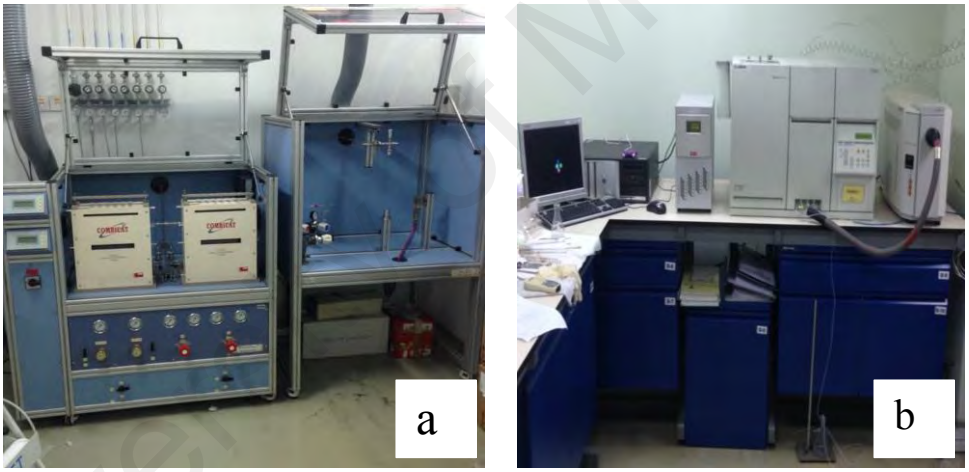

Fig. 3.2: Image view of (a) catalyst activation unit, (b) Temeprature programmed reduction.

3.3.5 Catalyst activity studies

The activity of the magnetic nano particle catalyst was investigated for the hydrogenation of biomass derived furfural and vanillin in an automated 100mL (42 mm ID) capacity autoclave reactor. The reactor is made of Hast-alloy material C 276 by Cambridge reactor design Ltd. The reactor is equipped with mechanical stirrer, proportional integral (PI) pressure and temperature controllers, gas detectors for leak check. Prior to the commencement of the reaction, the H_2 cylinder set at 30bar dosing

pressure was connected to the reactor. Afterwards, it was sealed and purged with inert N_2 and then H_2 to exclude air. In a typical experiment, 60 mg of the activated $Fe(MFe)O_4$-SiO_2 catalyst was placed sealed in a catalyst bulb and fixed onto the reactor catalyst bulb holder. This was followed by loading into the reactor, 20 % (V/V) furfural in heptane solvent and ensured it is air tight. The reactor was heated and allowed for isothermal stabilization to different desired set point reaction temperatures and H_2 pressures. After completion of the reaction for the specified time, the autoclave reactor was cooled to 35 ^{o}C and depressurized to atmospheric pressure. The products were collected for qualitative analysis on gas chromatography, Agilent 6890N with 5973 MSD, auto sampler, and HP-5 capillary column (1.5µm × 30m × 530µm). Also, quantitative measurements of the identified products were done on Agilent 6890N (G152O) GC-FID using DB-WAX column (30m × 0.530µm).

$$\text{Conversion \%} = \frac{\mathbf{m(reactant)_{in} - m(reactant)_{out}}}{\mathbf{m(reactant)_{in}}} \times \mathbf{100} \qquad \text{Equation 3.1}$$

$$\text{Selectivity \%} = \frac{\mathbf{mC_p}}{\mathbf{\sum mC_p}} \times \mathbf{100} \qquad \text{Equation 3.2}$$

`**Fig. 3.3:** (a) Autoclave batch reactor (b) GC-FID.

University of Malaya

Table 3.2: Operation limits on autoclave reactor (a)

Condition/Variables	Type	Limits	Units
Experimental Id			
Catalyst Mass	Real	0-10	gram
Catalyst ID	Text	0-15	characters
Reactant mass	Real	0-10	gram
Reactant ID	Text	0-15	characters
Gas ID	Text	0-15	characters
Leak check conditions			
Set point pressure	Real	0-250	Bar
Time	Integer	0-60	min
Reaction condition			
Set point Temperature	Real	0-250	^{o}C
Set point pressure	Real	0-250	Bar
Stirring	Boolean	On-off	N/A
Stirring speed	Integer	0-1500	RPM
Reaction time	Integer	0-500	minute

Table 3.3: Operation limits on autoclave reactor (b)

Condition/Variables	Type	Limits	Units
Post processing conditions			
Reactant melting point	Real	0-250	^{o}C
Product flash point	Real	0-250	^{o}C
End point temperature	Real	0-250	^{o}C
Stirring	Boolean	On-off	N/A
Stirring speed	Integer	0-1500	rpm
Purge time	Integer	0-60	minutes
Alarm condition			
Temperature High alarm	Real	0-300	^{o}C
High alarm set point	Real	0-250	^{o}C
High High alarm	Real	0-300	^{o}C
Low Alarm	Real	0-300	^{o}C
Low Low Alarm	Real	0-300	^{o}C
Pressure High Alarm	Real	0-270	Bar
High High Alarm	Real	0-270	Bar
Low Alarm	Real	0-270	Bar
Low Low Alarm	Real	0-270	Bar

University of Malaya

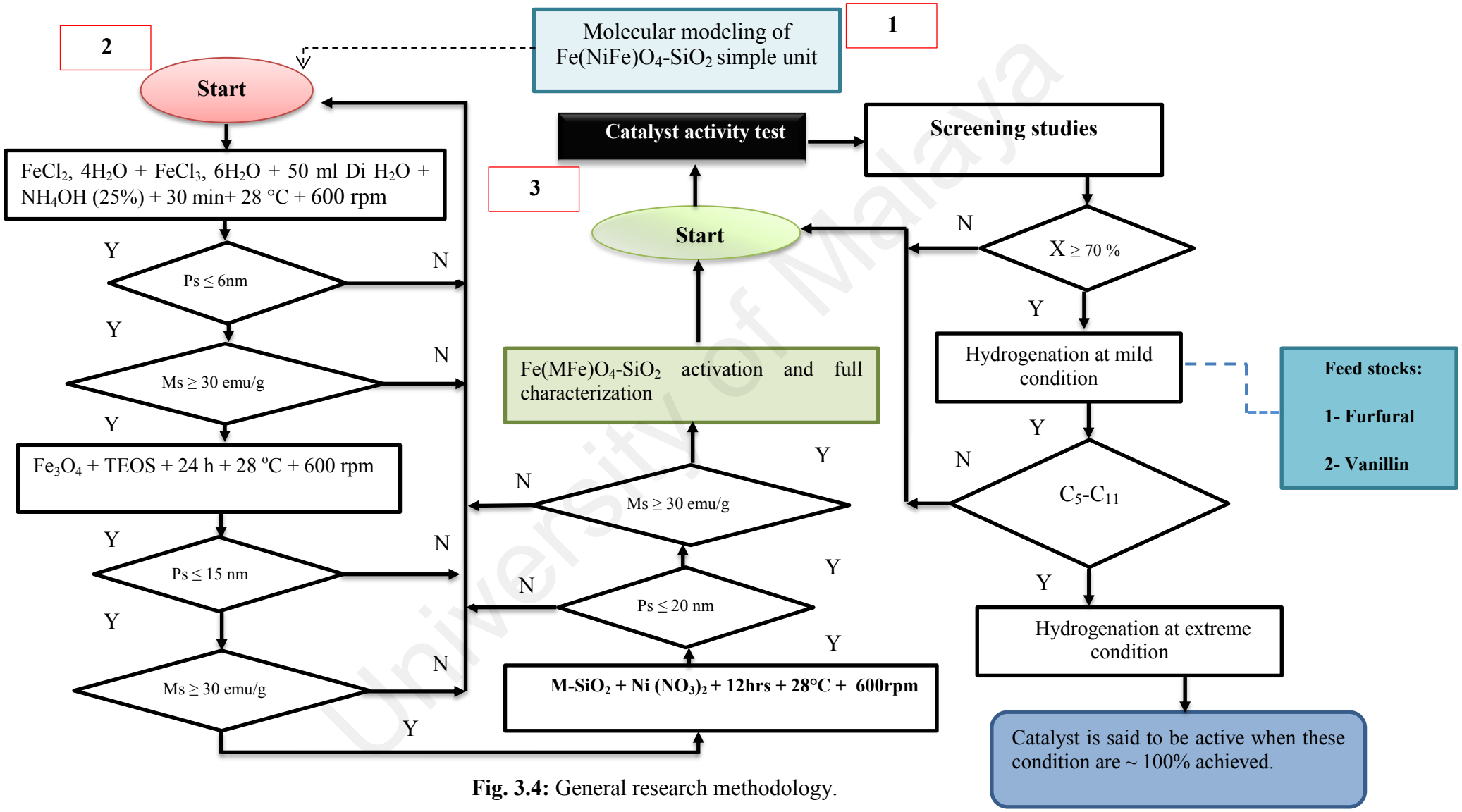

Fig. 3.4: General research methodology.

University of Malaya

CHAPTER 4: RESULTS AND DISCUSSION

4.1 Molecular model of simple $Fe(MFe)O_4$-SiO_2 repeating unit

Using the mechanic method and universal force field functional, simple repeating unit of $Fe(MFe)O_4$-SiO_2 catalyst was built and optimized on optimization job type module in Gaussian software platform. This procedure was developed prior to synthesis process. On frequency module, vibrational spectroscopy of the metal point charge linkages were evaluated and result tabulated and corroborated with experimental values as seen in table 4.1. The observed, 27 computed vibrational modes agreed with experiment ones and confirmed that the synthesized material was the intended. In addition, negative wave numbers indicates that the potential energy surface is minimum and suggestive to confirm the meta-stable nature of the catalyst. The Z-matrix representing the Cartesian internal coordinate for the simple repeating $Fe(MFe)O_4$-SiO_2 catalyst unit are given in the appendix.

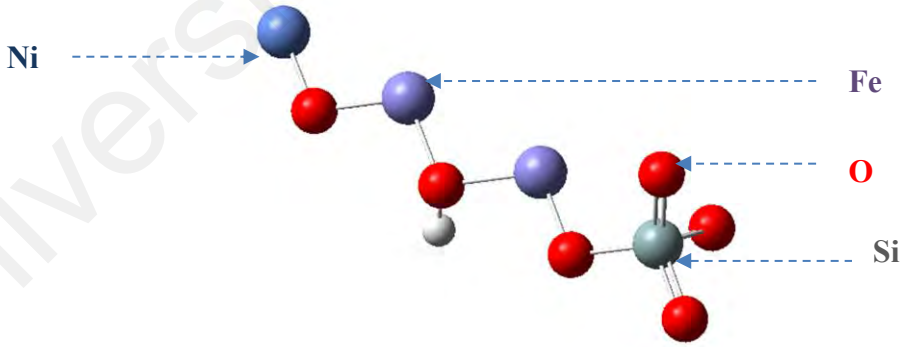

Fig. 4.1: Molecular model of simple repeating unit of $Fe(MFe)O_4$-SiO_2 nanoparticle catalyst.

University of Malaya

Table 4.1: Corroboration of experimental and simulated vibrational modes for $Fe(MFe)O_4$-SiO_2 nanoparticle catalyst.

S/N	Simulation		Raman experiment	
			*400 ^oC	*500 ^oC
	WN (cm^{-1})	Assignment	WN (cm^{-1})	WN (cm^{-1})
1	-239.55	Out of plane twisting of Ni-O-Fe	-	-
2	-68.42	In plane bending of Ni-O-Fe-O-Si	-	-
3	-40.91	In plane bending of Ni-O-Fe-O	-	-
4	32..97	Scissoring bending of Ni-O-Fe	-	-
5	128.21	Bending of Fe-O-Fe	-	-
6	134.09	Outward stretching of Ni-O-Fe-O-Si	133.25	138.96
7	167.32	Stretching of Ni-O-Fe	-	-
8	199.70	bending of Fe-O-Si	194.79	211.00
9	239.78	Stretching of Ni-O-Fe-O-Si	-	235.34
10	265.40	Rocking of O-Si-O Fe-O-Si	269.27	261.11
11	415.36	Stretching of O-Si	343.22	354.39
12	542.96	Stretching of Fe-O-Si	-	492.51
13	561.33	Out of plane twisting of Ni-O-Fe	566.00	-
14	590.81	In plane bending of Ni-O-Fe-O-Si	-	-
15	604.99	In plane bending of Ni-O-Fe-O	-	-
16	722.13	Scissoring bending of Ni-O-Fe	712.34	708.00
17	764.73	Bending of Fe-O-Fe	-	-
18	810.96	Outward stretching of Ni-O-Fe-O-Si	-	-
19	855.49	Stretching of Ni-O-Fe	856.24	852.76
20	867.27	bending of Fe-O-Si	-	-
21	905.41	Stretching of Ni-O-Fe-O-Si	-	-
22	940.29	Rocking of O-Si-O Fe-O-Si	942.13	
23	1214.40	Stretching of O-Si	1208.95	
24	1231.73	Stretching of Fe-O-Si	-	-
25	1232.70	Out of plane twisting of Ni-O-Fe	1246.25	
26	1523.56	In plane bending of Ni-O-Fe-O-Si	1425.13	1400
27	3734.34	In plane bending of Ni-O-Fe-O	-	-

*400 ^oC & 500 ^oC = heat treatment temperature of $Fe(MFe)O_4$-SiO_2 catalyst (M = Ni)

University of Malaya

4.2 $Fe(MFe)O_4$-SiO_2 catalyst characterization

4.2.1 Thermo gravimetric (TGA) for $Fe(MFe)O_4$-SiO_2 nanoparticle catalysts

During the analysis, temperature was increased from 30 to 750 ^oC at 10^{o}C/min heating rate and 8mg of samples were measured for each experiment in order to avoid mass transfer limitations. The TGA-DTG curves for 8 mg $Fe(NiFe)O_4$-SiO_2 pre-activated catalyst are shown in Fig. 4.2 and 4.3. The total weight loss over the temperature range from 37 to 700 ^oC was found to be 5.8505 %, which is equal to 0.4034 mg. However, the first weight loss peak over the temperature range of 37-180 ^oC was assigned to loss of coordinated or crystalline water present on the catalyst surface. The noticed sharp weight loss at around 370 ^oC can be assigned also to dissociation of $(NO_3)_2$ from Ni $(NO_3)_2$ precursor. The last weight loss observed in the range of 450-550 ^oC indicates the dissociation of chlorides from $FeCl_2$ and $FeCl_3$. This thermochemical behavior of the catalyst described by TGA curve was consistent with DTG curve. In conclusion, the prepared catalyst is stable (> 93 %) up to 700 °C because only 5.8505% weight loss was found from TG-DTA study.

Similar effect was observed in the TGA-DTG curves for 8 mg $FeRuFeO_4$-SiO_2 pre-activated catalyst are shown in Fig 4.3.. The total weight loss over the temperature range from 37 to 700 ^oC was found to be ~8.4841%, which is equal to 0.554 mg. However, the first weight loss peak over the temperature range of 37-200 ^oC was assigned to loss of coordinated or crystalline water present on the catalyst surface. The noticed sharp weight loss at around 350 ^oC indicates the dissociation of chlorides from $FeCl_2$ and $FeCl_3$ and $RuCl_3$ precursors. This thermochemical behavior of the catalyst described by TGA curve was consistent with DTG curve. In conclusion, the prepared catalyst is stable (91.513%) up to 700 °C because only 8.4841% weight loss was found from TG-DTA study.

University of Malaya

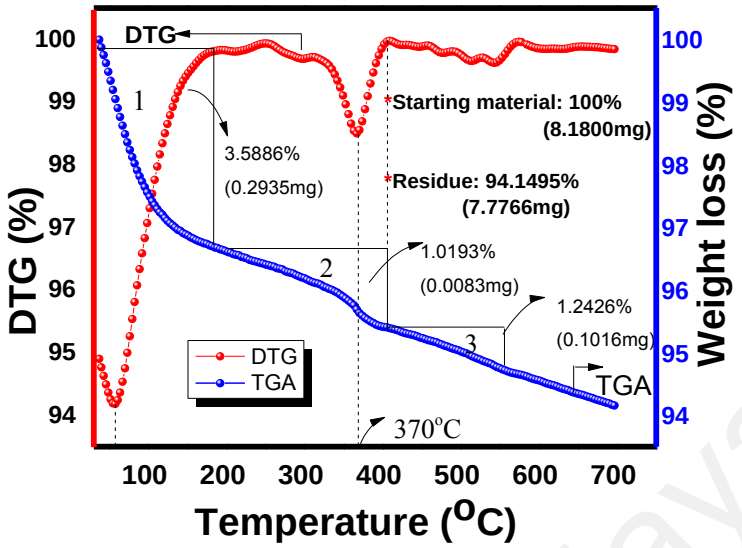

Fig. 4.2: TG-DTA analysis of mesoporous magnetic $Fe(NiFe)O_4$-SiO_2 nanoparticle catalyst.

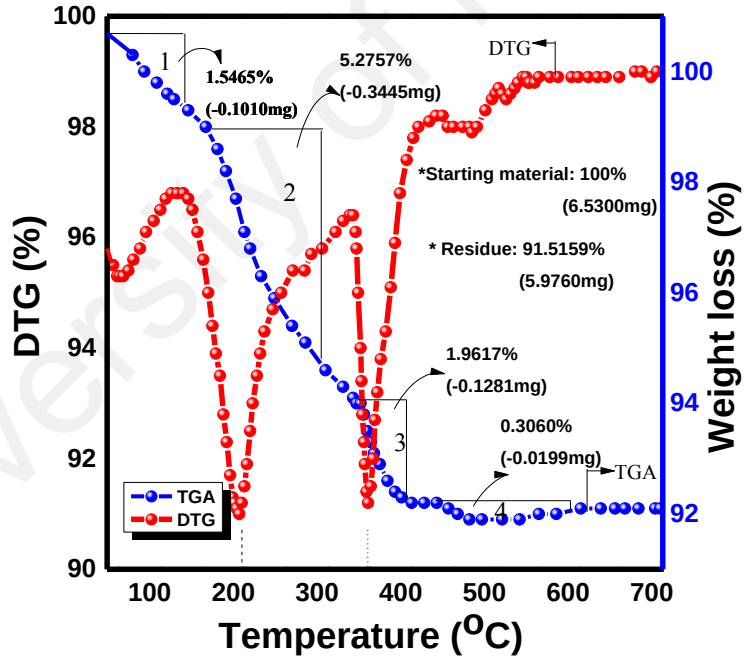

Fig. 4.3: TG-DTA analysis of mesoporous magnetic $Fe(RuFe)O_4$-SiO_2 nanoparticle catalyst.

University of Malaya

4.2.2 Vibrating sample magnetometer (VSM) for $Fe(MFe)O_4$-SiO_2 catalysts

One of the attractive features of $Fe(NiFe)O_4$-SiO_2 nanoparticles catalyst is its magnetic anisotropy, which is significantly different from the conventional catalysts. VSM analysis of $Fe(NiFe)O_4$-SiO_2 nanoparticles was done. Fig 4.4 presents the hysteresis measurement at room temperature in the applied field sweeping from -10 to 10kOe of reduced $Fe(NiFe)O_4$-SiO_2 nanoparticles catalyst. The obtained results indicate super-paramagnetic property of $Fe(NiFe)O_4$-SiO_2 and $Fe(RuFe)O_4$-SiO_2 nanoparticles catalyst. The saturation magnetization (Ms) of $Fe(NiFe)O_4$-SiO_2 catalyst for instance was found to be 39.834 emu/g, whereas reference Fe_3O_4-SiO_2 core-shell architecture exhibits at about 45.67 emu/g. This decrease in Ms indicates successful incorporation of Ni^{2+} at the octahedral O_D site in the $Fe(NiFe)O_4$-SiO_2 inverse spinel structure. This is in good agreement with 5.8136 G coercivity of $Fe(NiFe)O_4$-SiO_2, which is significantly low compared with that of 27.323 G coercivity of reference Fe_3O_4-SiO_2 (Fig 4.4c). Therefore, the decrease in Hc and Ms is a clear indication of distortion in magnetocrystalline anisotropy contribution by Fe^{3+} as a result of Ni^{2+} occupying octahedral Fe^{3+} sites. As a consequence, the displaced Fe^{3+} occupies the vacant octahedral oxygen sites. However, the possibility of Ni $^{2+}$ leaching in contrast to conventional ones used for the similar application would be expected to very low due to the magnetic interaction of Ni $^{2+}$ and Fe_3O_4. These observations are good agreement with previously published results. These results also reveal that the catalyst has no NiO (anti-ferromagnetism as seen in the Fig 4.4b) impurities. This indicates that electronic structure of all Ni $^{2+}$ is perturbed to form a strong bond at the octahedral site in contrast to a conventional non-magnetic catalyst, in which the electronic structure of Ni $^{2+}$ is barely perturbed upon adsorption. In the conventional case, the active metals are typically physisorbed based on metal

University of Malaya

support interaction effects only. Reduction in Hc and Mc is an indication of Ni incorporation into the lattice structure of Fe_3O_4 dispersed in SiO_2. The catalyst has magnetic remanence 0.5042 emu/g as shown in Fig 4.4c. This observation indicates that the $Fe(MFe)O_4$-SiO_2 catalyst has magnetic property even at room temperature when no magnetic field is applied.

Generally as represented in Fig 4.5, low Ms values are related to the particle with smaller size. This is attributed to the surface distortion due to interaction of transition metal ions in the spinel lattice with oxygen atoms otherwise known as point charges. Ms values for $Fe(NiFe)O_4$-SiO_2 are smaller than $Fe(RuFe)O_4$-SiO_2, in extrinsic terms because the ionic radius of Ru is greater than Ni thus, particle size of the former is evidently larger than the later. The Ms together with the particle size indicates that $Fe(RuFe)O_4$-SiO_2 and $Fe(NiFe)O_4$-SiO_2 are in the super paramagnetic domain around less than 20 nm particle size. However, heat treatment happens to be one of the approaches to tune the catalyst particle size as shown in this study.

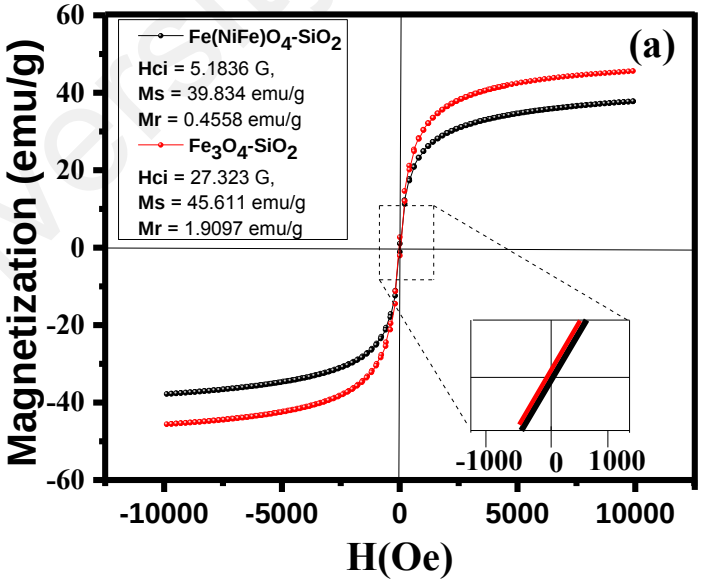

University of Malaya

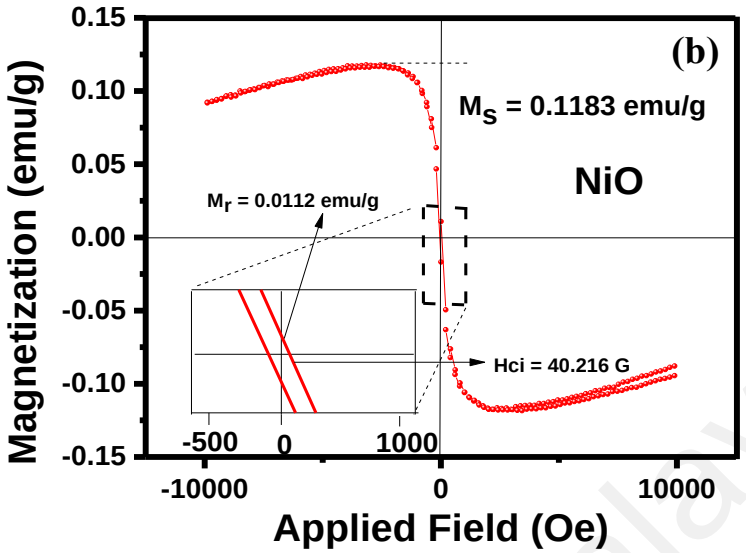

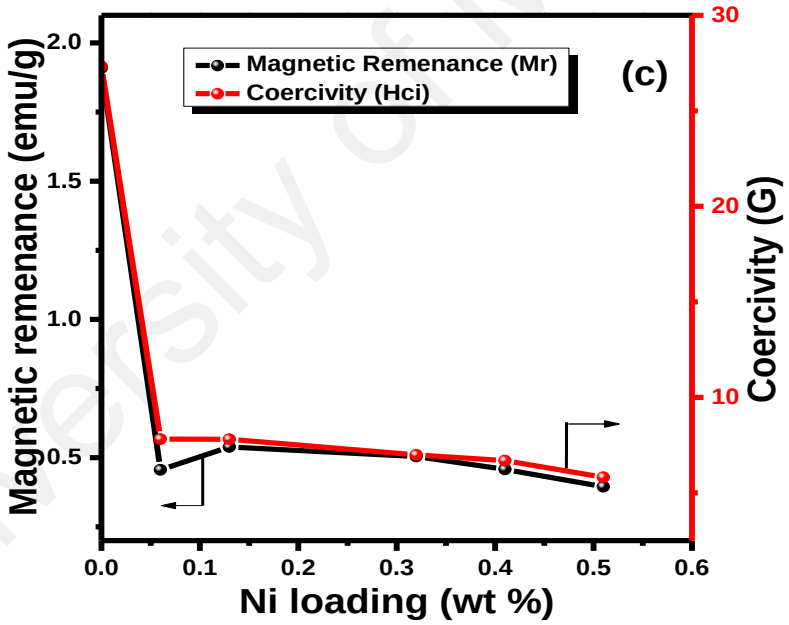

University of Malaya

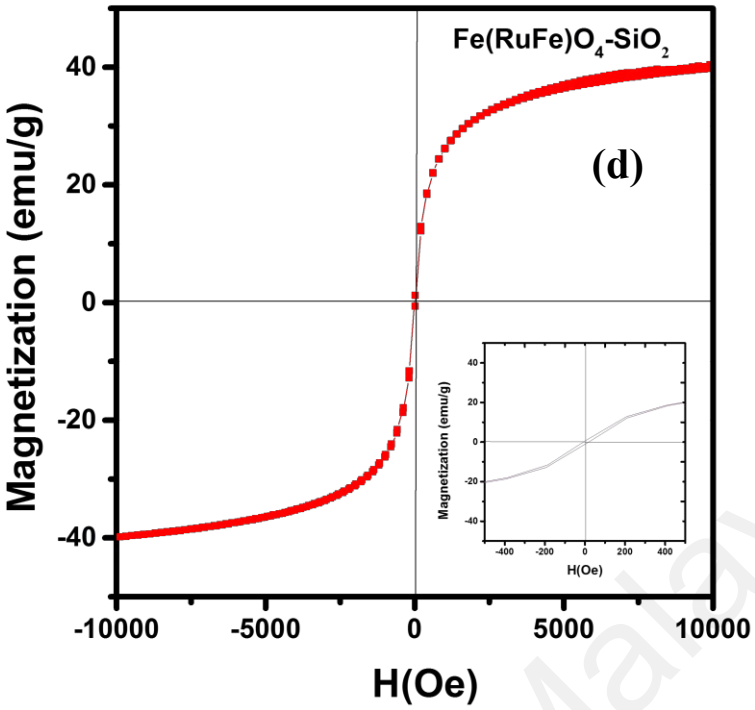

Fig. 4.4: Super-paramagnetic hysteresis loops for (a) $Fe(NiFe)O_4$-SiO_2 catalyst, (b) bulk nickel oxide and (c) effect of Ni loading on magnetic Remanence (Mr) and coercivity (Hci) of the $Fe(NiFe)O_4$-SiO_2 catalyst (d) $Fe(RuFe)O_4$-SiO_2 catalyst.

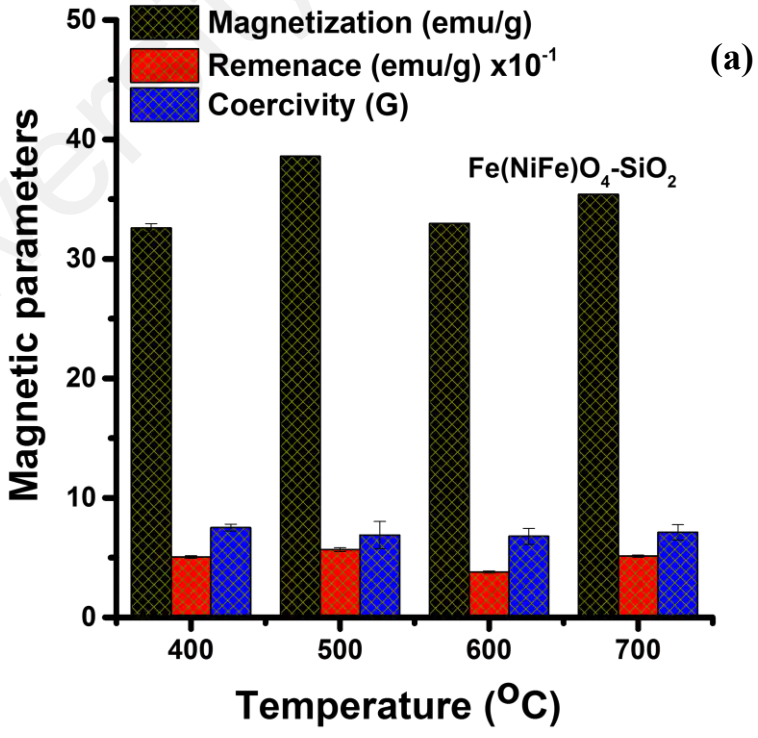

University of Malaya

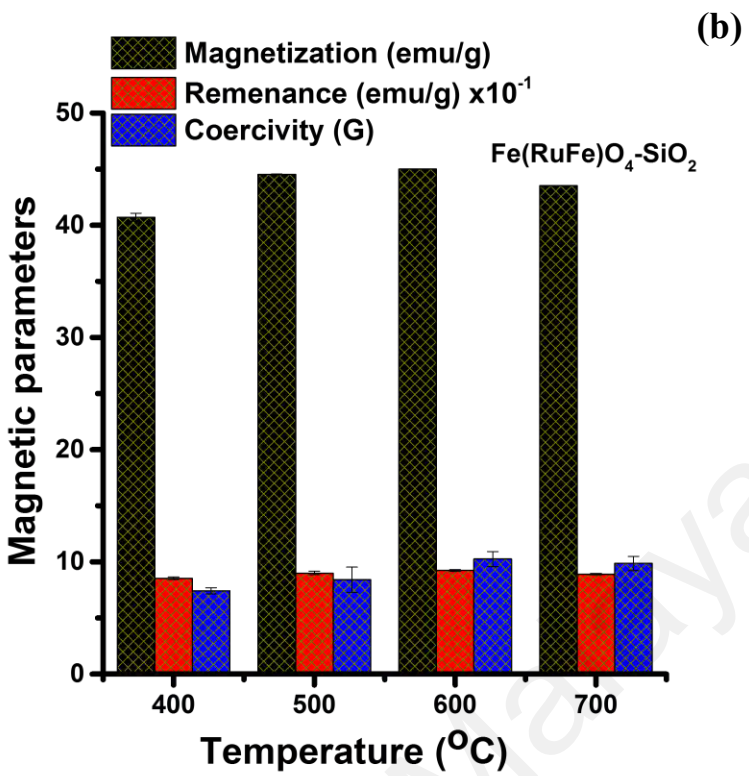

Fig. 4.5: Distribution of (a) $Fe(NiFe)O_4$-SiO_2, magnetic parameters (Magnetization Ms, Magnetic Remanence Mr, and coercivity Hc) with temperature and (b) $Fe(RuFe)O_4$-SiO_2, magnetic parameters (Magnetization Ms, Magnetic Remanence Mr, and coercivity Hc) with temperature.

4.2.3 X-Ray diffraction (XRD) for $Fe(MFe)O_4$-SiO_2 catalysts

The XRD analysis was conducted in order to identify the phases present in the $Fe(MFe)O_4$-SiO_2 catalyst as well as their lattice parameter, and particle. This is shown in Fig 4.6 and 4.7 where XRD pattern for ~0.5wt% Ru in $Fe(RuFe)O_4$-SiO_2 and ~0.5wt% Ni $Fe(NiFe)O_4$-SiO_2 catalyst were revealed. In Fig. 4.6, the diffraction patterns for Fe_3O_4-SiO_2 reference materials after activation at 500 ^oC for 3 h were indexed at 30.51, 35.62, 43.94, 57.46, and 62.86°. These patterns correspond to crystallographic planes (200), (103), (240), (341) and (064), respectively. Similarly, the diffraction patterns of $Fe(NiFe)O_4$-SiO_2 was indexed at 35.68, 57.37 and 63.01°. According to JCPDF/ICDD: 0875-003, the patterns corresponds to 100, 33 and 53% of $Fe(NiFe)O_4$-SiO_2 on the (311), (511) and

University of Malaya

(440) crystallographic planes, respectively. The $Fe(NiFe)O_4$-SiO_2 nanoparticles catalyst formed a cubic crystal structure with lattice constant a_0 = 8.34 Å and d-spacings: d (311) = 0.265 nm, d (511) = 0.171 nm and d (440) = 0.15 nm. These information revealed that nickel species occupy the octahedral sites to form $Fe(NiFe)O_4$-SiO_2 whilst its diffraction pattern as seen earlier is in contrast to 44.3, 51.4 and 76.1° metallic nickel phase which occur at (111), (200), (220) planes according to JCPDS 65-0380 (Ding *et al.,* 2015). Furthermore, the XRD results confirm that Ni^{2+} and Fe^{3+} did not form alloy which has diffraction peaks at 45.6, 64.99 and 82.3° that correspond to (110), (200) and (211) crystallographic planes, respectively (Ci *et al.,* 2015). The estimated particle size of $Fe(NiFe)O_4$-SiO_2 on the (311), (511) and (440) planes was found to be ~13.3, 14.4 and 14.8 nm, respectively, with an average size of 14.2 nm. It is interesting to highlight this size against 14.4 nm obtained from HRTEM analysis. Evidently, the size of this nanoparticle catalyst is close to the quantum regime (2-10 nm). This observation therefore indicates that energy level quantization may occur close to the 3D confinement to facilitate proper quantum transports, and ultimately enhance the catalytic function of the active phase. In contrast, a similar $NiFe_2O_4$ material that was synthesized by sol-gel and oxalic acid co-precipitation methods exhibit much larger particle size in the range of 20 and 50 nm, respectively. This observation indicates the significance of one-pot synthesis method used in the present study to obtain smaller size magnetite nanoparticles catalyst. The XRD results, therefore, conclude that $Fe(NiFe)O_4$ crystal incorporation in SiO_2 from Fe_3O_4 is an indicative lattice distortion by doping of Fe^{3+}octahedral sites with Ni^{2+} ions. Furthermore, this result is in good agreement with the VSM analysis, which evidenced a decrease in the coercivity of the $Fe(NiFe)O_4$-SiO_2 catalyst after the Ni incorporation (Fig. 4.4).

University of Malaya

As an extension to study how heat tune the surface atom energetics of $Fe(MFe)O_4$-SiO_2 catalyst, Fig. 4.7 shows the diffraction patterns of four $Fe(RuFe)O_4$-SiO_2 and $Fe(NiFe)O_4$-SiO_2 samples each that was heat treated (HTs) at 400, 500, 600 and 700^oC. These were indexed at 2θ values of ~ 30.20 °, 35.73 °, 43.75 °, 53.60 °, 57.62 °, 63.15 ° and ~ 30.48 °, 35.64 °, 43.49 °, 53.81 °, 57.32 °, and 63.11 ° respectively to show the crystallinity of the final HTs samples. According to reference code: 96-900-6923, these peaks corresponds to a cubic crystal structure having group space F-43m and lattice constant a_0 = b = C = 8.34 Å, d-spacings: d (311) = 0.265 nm, d (511) = 0.171 nm and d (440) = 0.15 nm. One significant observation from this analysis is the crystallite size variation with the corresponding heat treatment temperatures. The sizes for $Fe(RuFe)O_4$-SiO_2 and $Fe(NiFe)O_4$-SiO_2 catalyst were ~12.5 nm, ~ 14.2 nm, ~18.9 nm, ~13.4 nm and ~12.6 nm, ~14.5 nm, ~19.8 nm, ~13.6 nm respectively. These were obtained from the X-ray diffraction broadening of the strongest (311) plane employing Scherer's expression in High-Score Plus to estimate the crystallite sizes of all the HTs samples in the range. In addition these values are indicative that the catalysts are all in the super-paramagnetic domain because their crystallite size < 20 nm. The phase identification of these catalyst material revealed ~ 3% crystalline Fe_3O_4 but predominantly $Fe(NiFe)O_4$-SiO_2 phases were observed with amount ~ 97%. Similarly, ~ 7% crystalline Fe_3O_4 but predominantly $Fe(RuFe)O_4$-SiO_2 with ~ 93% was recorded.

As shown in Fig 4.7, the corresponding crystallographic planes for $Fe(NiFe)O_4$-SiO_2 and $Fe(RuFe)O_4$-SiO_2 catalyst agreed with the visualized ones from the HRTEM imagery.

University of Malaya

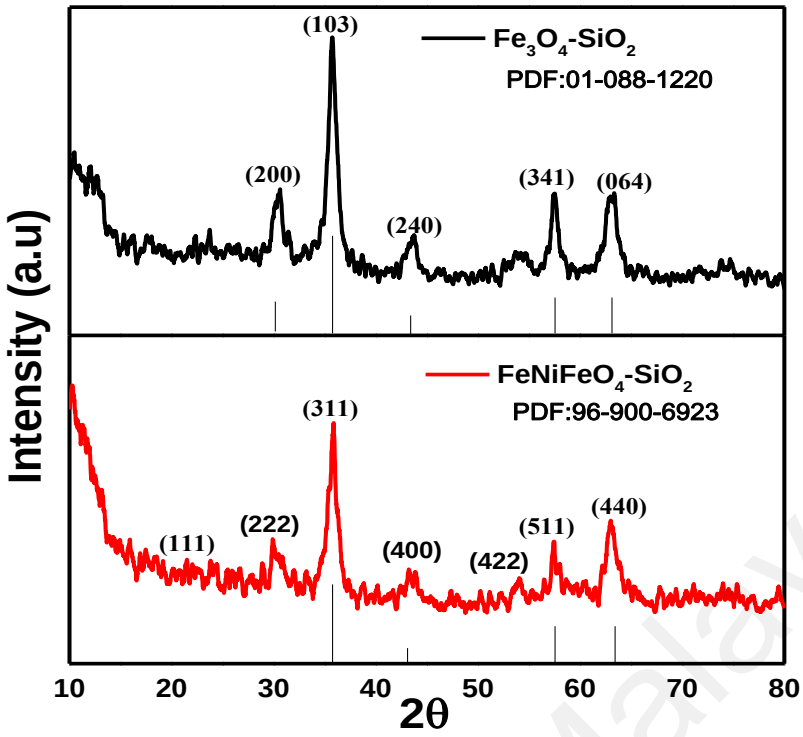

Figure 4.6: XRD patterns of mesoporous magnetic Fe(NiFe)O_4-SiO_2 nanoparticles.

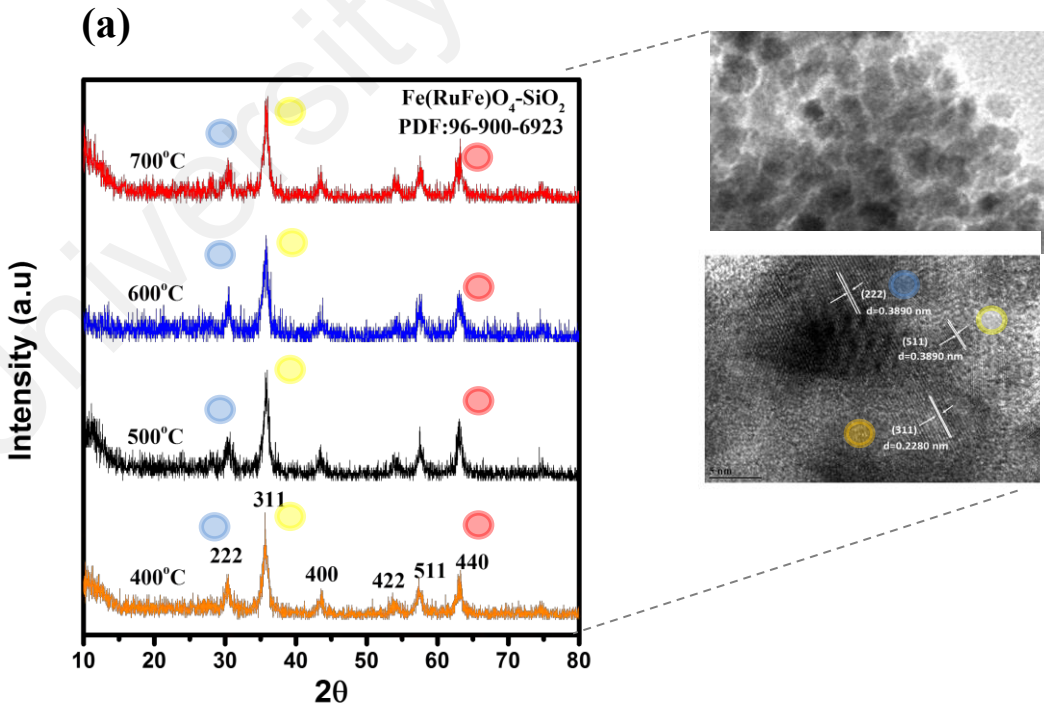

University of Malaya

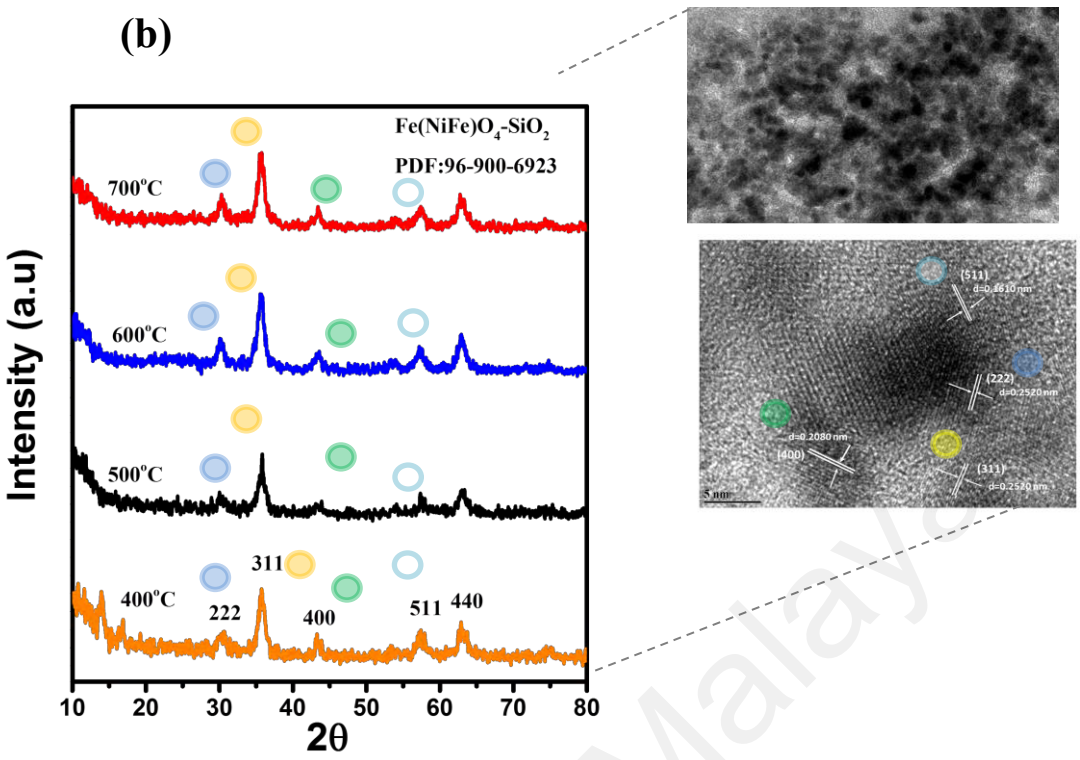

Fig. 4.7: Distribution of XRD patterns of (a) $Fe(RuFe)O_4$-SiO_2 and (b) $Fe(NiFe)O_4$-SiO_2 catalysts with temperature.

4.2.4 N_2 adsorption-desorption and distribution of $Fe(MFe)O_4$-SiO_2 nanoparticle textural property with temperature

The N_2 adsorption-desorption isotherm and pore size distribution of $Fe(NiFe)O_4$-SiO_2 are shown in Fig. 4.8 and further complimented by $Fe(RuFe)O_4$-SiO_2 catalyst that was heat treated at 400 °C, 500 °C, 600 °C and 700 °C under 1 °C /min ramping and 3h holding time. However, prior to analysis, the entire sample was degassed at 300 °C for 3 h because it has been evidenced in this study that 300 °C until 400 °C has no observable state change effect on the catalyst. The obtained N_2 adsorption-desorption isotherm can be classified as Type IV isotherm with H1-type hysteresis. The specific surface area of $Fe(NiFe)O_4$-SiO_2 treated at 500 °C was found to be 259 m^2/g among others.

University of Malaya

Fig. 4.9 (a) and (b) shows the hysteresis loop and distribution of textural properties for both $Fe(NiFe)O_4$-SiO_2 and $Fe(RuFe)O_4$-SiO_2 nano particle catalysts that was heat treated over 400, 500, 600 and 700^oC temperatures. The estimated Biot number (Bi) for these particles was 264.10 > 1 and indicates non-uniform heat distribution fields within the mesoporous matrix of the catalyst nanoparticle. Subsequently, in tables 4.2 and 4.3, the CFSE-Nu^{2+} and CFSE-Ru^{3+} > CFSE Fe^{3+} suggests the inverse spinnel shape of the catalyst, we therefore suggest in addition axial heat distribution over the grain scales of $Fe(MFe)O_4$-SiO_2 structures**.** The Nusselt number for the static environment fluid around the particles being 100.14 further justify the Biot number and indicates more active convection with typical turbulent flow of hot air around the $Fe(MFe)O_4$-SiO_2 particle.

The dimensionless numbers; Biot = hL_p/K_p and Nusselt = hL_p/K_f are built with length and temperature scales that characterize the flow and thermal conditions around the catalyst nanoparticles. They are relevant in showing heat transfer phenomena as fundamental rationale for the distribution in textural properties of $Fe(MFe)O_4$-SiO_2 catalyst in this study. The information from BET analysis as shown in Fig. 4.9 (a) and (b) and (c) and the magnitude of the dimensionless numbers are indicative of direct response to the heat treatments. Proper account on the rationale guiding these distributions is hinged on capillary condensation, capillary evaporation and tensile strength effect phenomena as indicative of heat effect on the particles. Therefore, we observed numerically close surface area attributes for 400 ^oC (~ 61.05 m^2/g), 600 ^oC (~ 57.03 m^2/g) and 700 ^oC (~56.5 m^2/g) heat treatment of $Fe(NiFe)O_4$-SiO_2 catalyst however, at 500 ^oC, a superior surface area of ~259 m^2/g (Halilu et al., 2016) was recorded. The pore volume and size was in the range 0.21-0.9 m^3/g and 6.8-10.9 nm respectively. Controlling this process is indeterminate, however, the maximum recorded area confirmed that surface area was maximized in order to compensate for surface atom energetics in contrast to 400 ^oC 600 ^oC and 700 ^oc whose surface area were

University of Malaya

minimized to compensate for surface atom energetics. Different observation were recorded for $Fe(RuFe)O_4$-SiO_2 at 400 ^oC (~110 m^2/g), and 700 ^oC (~ 116 m^2/g) whose surface area was maximized and at 500 ^oC (~ 96 m^2/g), and 600 ^oC (~ 82 m^2/g), surface area was minimized to compensate for surface atom energetics. In this case, the catalyst pore size and volumes are in the range 7.4-8.7nm pore size and 0.22-0.35 m^3/g respectively.

Fig. 4.9 (c) shows the surface density distribution for $Fe(MFe)O_4$-SiO_2 catalysts. The surface densities (SD) of $Fe(RuFe)O_4$-SiO_2 < SD of $Fe(NiFe)O_4$-SiO_2. This is attributed to the difference in ionic radii; Ru ionic radii ~0.82 nm and Ni ionic radii ~0.69 nm. These observations revealed that surface density of surface atoms is inversely related to ionic radii (IR) (SD $\propto$ 1/IR) and also inversely related to specific surface area (SA) (SD $\propto$ 1/IR). Evidenced from surface unsatisfied bonds that seek surface relaxation and reconstruction as indicative of surface defect on heating, the observation was prominent. This phenomenon involves rearrangement of surface atoms and was driven by the desire to reduce surface free energy. In this case, relaxation was simply a little and subtle rearrangement of surface layers based on the energetics of the solid surface as a commonplace for metal surfaces. Relaxation is adjustment in the atomic layer spacing perpendicular to the crystal surface. In this case, there is no change in the periodicity parallel to the surface. On the other, reconstruction of surface atoms as shown in Fig. 4.9 (c) involves displacements of surface atoms and also involves change in periodicity of the surface structure. These two phenomena which BET analysis reveal in corroboration with AFM analysis on the catalysts topography in Appendix H, preempt the proposal of terrace site or edge sites on the catalyst surface.

University of Malaya

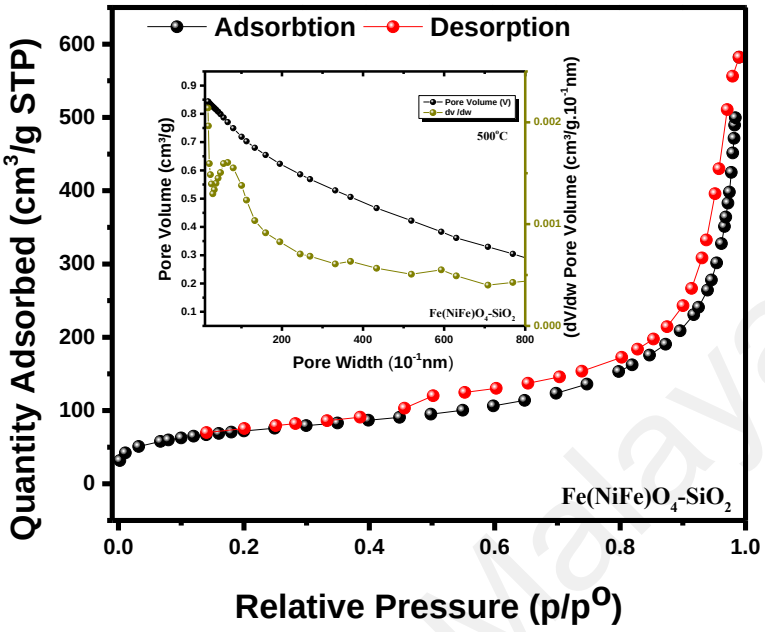

Fig. 4.8: Nitrogen adsorption-desorption curve for $Fe(NiFe)O_4$-SiO_2 nanoparticles catalyst.

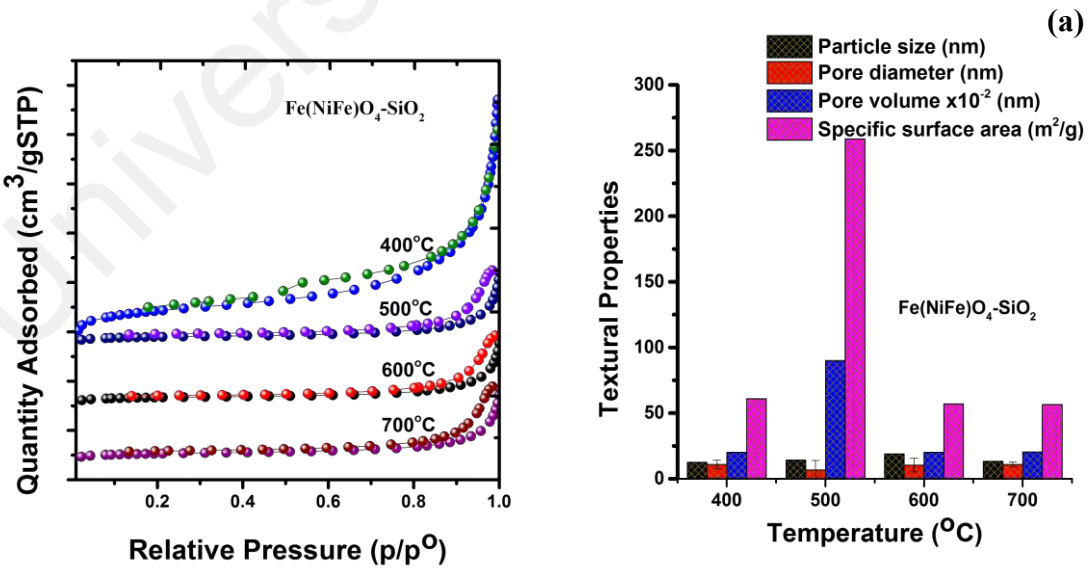

University of Malaya

(b)

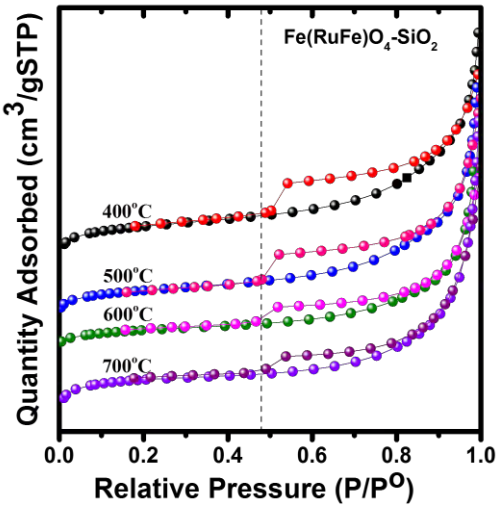

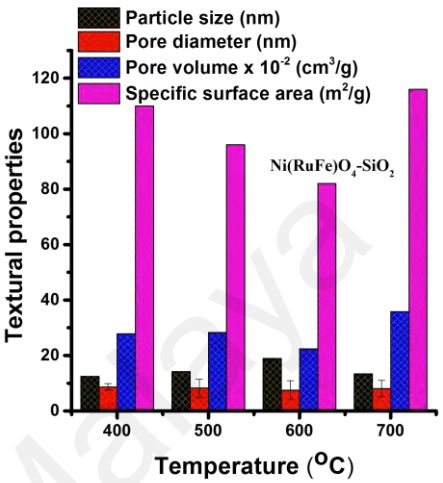

(c)

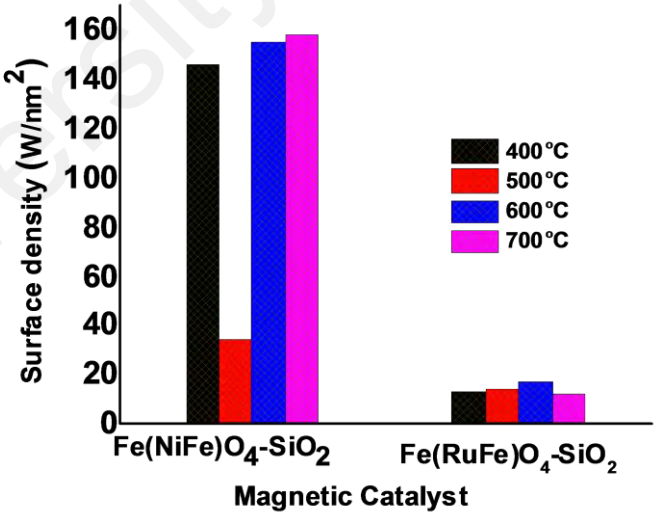

University of Malaya

(d)

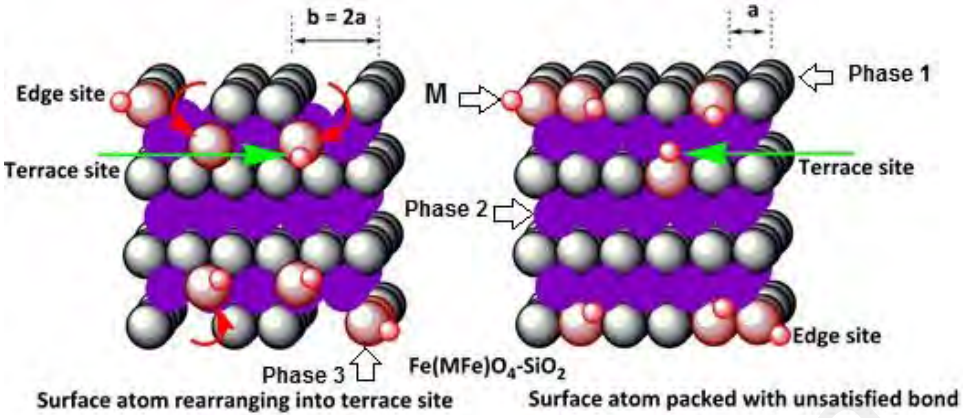

Fig. 4.9: (a) Nitrogen adsorption-desorption curve of $Fe(NiFe)O_4$-SiO_2 nanoparticles (b) Nitrogen adsorption-desorption curve of $Fe(RuFe)O_4$-SiO_2 nanoparticles (c) Surface density distribution for $Fe(NiFe)O_4$-SiO_2 and $Fe(RuFe)O_4$-SiO_2. (d) Surface atom rearrangement as a response to heat treatment. All analysis was done at 77k. M = Ni or Ru, Phase 1 = un-bonded SiO_2 or Fe_3O_4, Phase 2 = SiO_2 or Fe_3O_4 on basal plane and Phase 3 = Fe_3O_4- SiO_2.

4.2.5 High resolution transmission electron microscopy (HRTEM) for $Fe(MFe)O_4$-SiO_2 catalysts.

The HRTEM images of mesoporous magnetic $Fe(NiFe)O_4$-SiO_2 and $Fe(RuFe)O_4$-SiO_2 catalyst have been determined as shown in Fig. 4.10 (a) and (b) respectively. The image therein is made up of global and local regions that contain highly dispersed metal active phase for $Fe(NiFe)O_4$ and $Fe(RuFe)O_4$ nanoparticle catalyst. The global white region indicates silica, while the local dark spot corresponds to $Fe(NiFe)O_4$ or $Fe(RuFe)O_4$ respectively. The lattices fringes of magnetic $Fe(NiFe)O_4$-SiO_2 catalyst can be clearly observed in Fig. 4.10 (a) and (b). The estimated lattice d-spacing for $Fe(NiFe)O_4$-SiO_2 were found to be ~0.179 nm, 0.268 nm, and 0.152 nm, which correspond to (511), (311), and (440), respectively. Similarly $Fe(RuFe)O_4$-SiO_2 the estimated lattice d-spacings for $Fe(RuFe)O_4$-SiO_2 were found to be ~0.252 nm, 0.257 nm, 0.208 nm and 0.161 nm, which correspond to (222), (311), (400), and (511) planes respectively.

University of Malaya

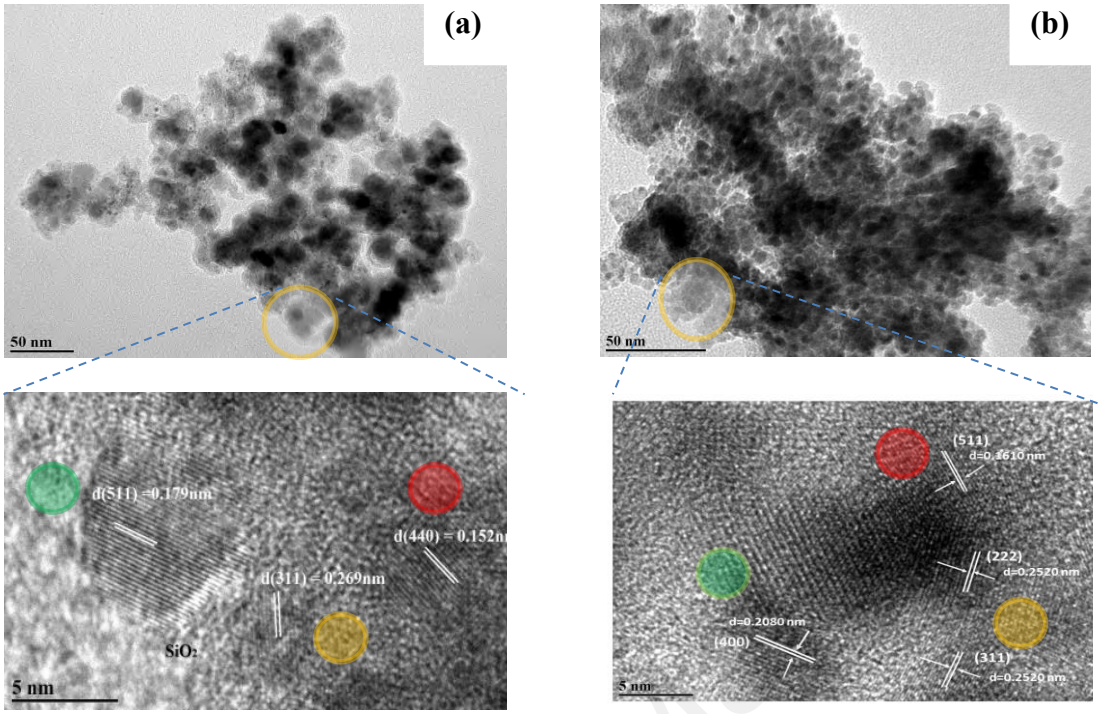

Fig. 4.10: (a) HRTEM image of mesoporous Fe(NiFe)O_4-SiO_2 nanoparticles and lattice fringes display and (b) HRTEM image of mesoporous Fe(RuFe)O_4-SiO_2 nanoparticles and lattice fringes display.

4.2.6 Field emission scanning electron microscopy (FESEM) for Fe(MFe)O_4-SiO_2 nanoparticle catalysts

Fig. 4.11 shows field emission scanning electron microscopy and energy dispersive X-ray (EDX) spectrometry of reference Ni-SiO_2 and Fe(MFe)O_4-SiO_2 nanoparticle catalyst. The active components Ni and Ru are not visible due to the fact that it is completely chemosorbed thereby forming a single phase. The morphology for Fe(MFe)O_4-SiO_2 confirms the planes observed from HRTEM analysis for the catalysts. From the HRTEM (Fig 4.10) measurement of the lattice fringes in relation to XRD d-spacing values (Fig. 4.5, 4.6 and 4.7); the EDX (Fig. 4.11) elemental analysis confirmed the presence of Ni, Si and O in Ni-SiO_2. Similarly, the presence of Ni, Fe, O, Si was also confirmed from the EDX analysis of Fe(NiFe)O_4-SiO_2. Accordingly, Ru, Fe, Si, O were identified in Fe(RuFe)O_4-SiO_2 catalyst.

University of

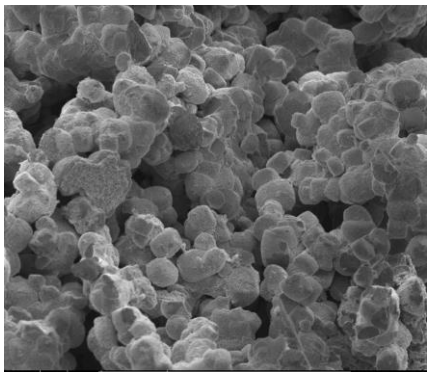

(a)

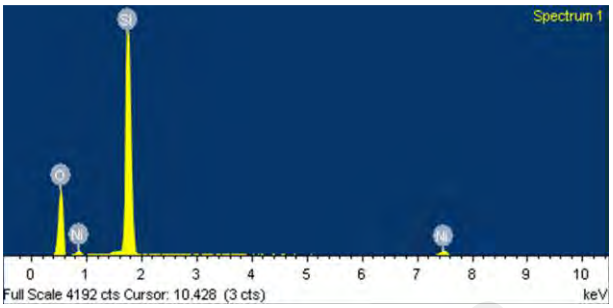

Ni-SiO_2

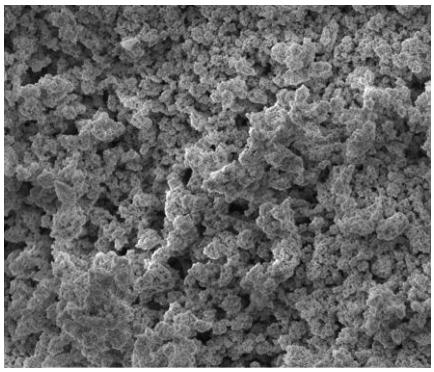

(b)

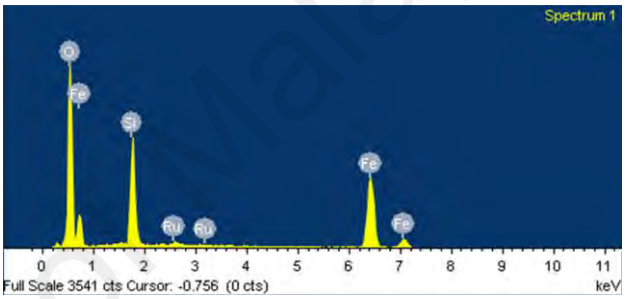

$Fe(RuFe)O_4$-SiO_2

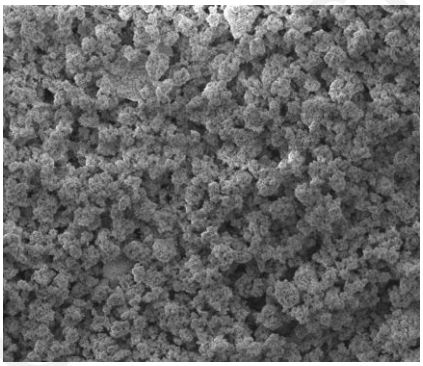

(C)

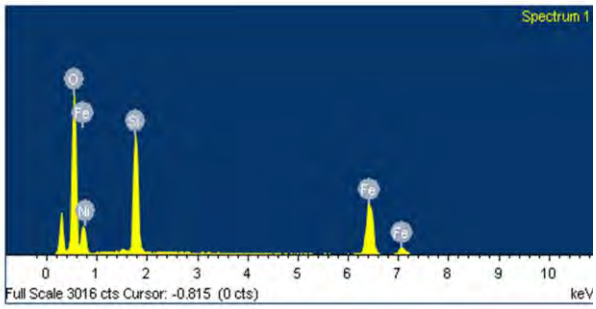

$Fe(NiFe)O_4$-SiO_2

Fig. 4.11: FESEM-EDX image of (a) Ni-SiO_2 (b) $Fe(RuFe)O_4$-SiO_2 and (b) $Fe(NiFe)O_4$-SiO_2 nanoparticles catalyst.

University of Malaya

4.2.7 FT-IR and Raman for $Fe(MFe)O_4$-SiO_2 catalyst

FT-IR as presented in Fig. 4.12(a), and Raman specttra in 4.12(b) and 4.12(c) revealed the chemical structure of the magnetic $Fe(MFe)O_4$-SiO_2 nanoparticles catalyst. The wavenumbers from FT-IR and Raman spectra modes are presented in Tables 4.2 and 4.3. Starting with $Fe(NiFe)O_4$-SiO_2 as shown in Fig. 4.12a, the bands centered at ~1082 and 808 cm^{-1} can be assigned to asymmetric and symmetric vibrations of -Si-O-Fe silica, respectively. These values confirm the formation of amorphous silica matrix. The possible perturbation occurring at octahedral site in the inverse spinel structure due to the replacement of Fe^{3+} by Ni^{2+} ions can be explained by red shifted Ni^{2+}-O bands at 460 cm^{-1}. Evidently, this observation can be confirmed with the standard FT-IR spectra of NiO noticed at ~ 451.57, 428.55, 415.74 and 407.99 cm^{-1} (Fig. 4.12a). Additionally, for an iron inverse spinel structure, higher wavenumber (500-600 cm^{-1}) bands and lower wavenumber (450-385 cm^{-1}) bands were noticed, which correspond to the vibration of O-M_{Td}-O at the tetrahedron site and stretching in the O-M_{ost}-O octahedron sites; where M_{Td} and M_{ost} represent metal at tetrahedral and octahedral sites, respectively. Therefore, the observed bands at ~ 567 and 648 cm^{-1} for $FeNiFeO_4$-SiO_2 were related to the vibrations of O-Fe_{Td}-O at the tetrahedral. Conclusively, this analysis was able to reveal the presence of silica matrix that serves as a shell to the core magnetite (Fe_3O_4). The presence of Fe_3O_4 was also confirmed by the vibrations O-Fe^{3+}_{Td}-O and the noticed red shifted O-Ni^{2+}_{oct}-O at 460 cm^{-1} suggests nickel incorporation on Fe_3O_4 at the octahedral sites.

Raman technique as structure sensitive tool confirmed the observations noticed from FT-IR analysis of magnetic $Fe(NiFe)O_4$-SiO_2 nanocatalyst. The Raman spectrum of the catalyst shows six Raman active modes; A_{1g}, E_g, $T_{2g}(1)$, $T_{2g}(2)$,

University of Malaya

T_{2g} (3) and TO-LO, along with three modes for silica (Fig 4.12b). T_{2g} (3) mode centered at 598 cm^{-1} is assigned to symmetric stretching of oxygen atoms along Ni-O bonds in the octahedral coordination, and this is an indication of a high degree of disorderliness in bond length. T_{2g} (2) centered at 500 cm^{-1} is due to asymmetric stretching of Fe (Ni) and O at the octahedral coordination. The reason for the formation of these bands is that Ni^{2+} has higher ionic radius (0.69 nm) compared to Fe^{3+} (0.49 nm), thus incorporation of Ni^{2+} into the Fe_3O_4 structure creates a local structural distribution in Fe/Ni-O bond length. Therefore, T_{2g} (2) and T_{2g} (3) correspond to vibrations of the octahedral group. T_{2g} (1) centered at 240 cm^{-1} is due to translational movement of the tetrahedral Fe^{3+} together with four oxygen atoms. A_{1g} centered at ~ 718 cm^{-1} is due to symmetric vibration of Fe-O along the tetrahedral coordination. E_g band centered at ~ 450 cm^{-1} is due to symmetric bending of oxygen with respect to the metal ion. The longitudinal and transverse optical vibrations (LO-TO) centered at 1310 cm^{-1} are due to Si-O-Fe asymmetry vibration. However, the silica siloxane bridge has Raman features at 800 cm^{-1}. This complimented, also, with the broad band at ~ 1070 and ~ 915 cm^{-1} as a typical characteristic of $Si\text{-}O^-$ and $Si\ (\text{-}O^-)_2$ functionalities. The observation of these bands indicates perturbation due to the formation of Fe-O-Si as a result of more Si-OH hydroxyl group's consumption. The observed results obviously indicate strong tetrahedral vibrational coupling of fayalite-like Fe_3O_4-SiO_2. This corresponds to the X-ray diffraction of Fe_3O_4-SiO_2 at planes (200), (103), (240), (341) and (064) in $Fe(NiFe)O_4$-SiO_4 according to Fig 4.6.

University of Malaya

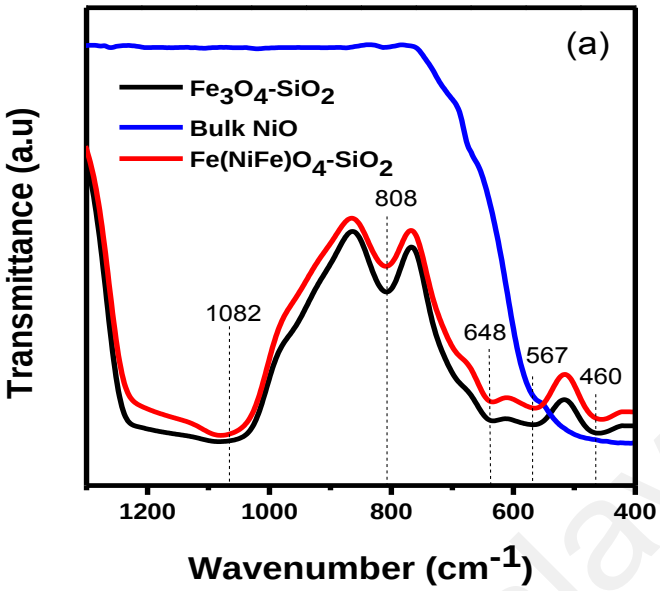

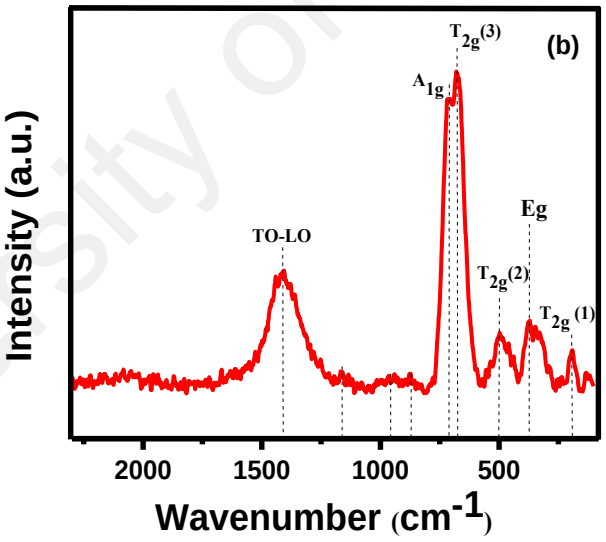

University of Malaya

(c)

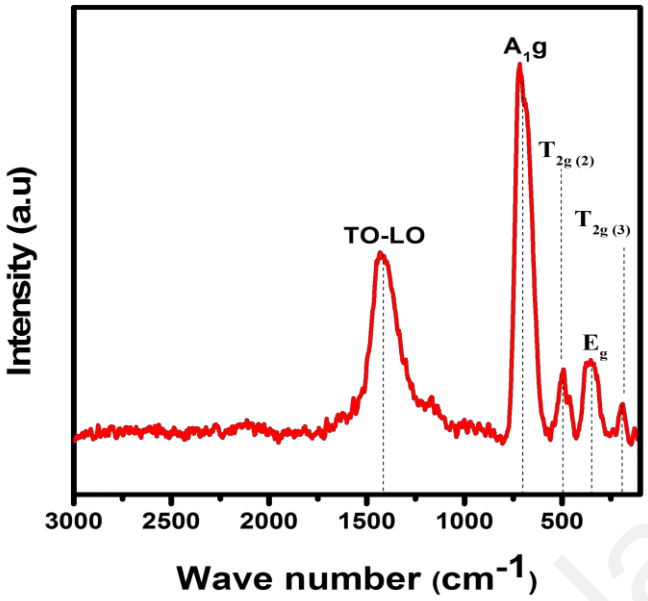

Fig. 4.12: (a) FTIR spectrum for $Fe(NiFe)O_4$-SiO_2 and (b) Raman spectrum of $Fe(NiFe)O_4$-SiO_2 (c) Raman spectrum of $Fe(RuFe)O_4$-SiO_2.

4.2.8 H_2- TPR for $Fe(MFe)O_4$-SiO_2 catalyst reducibility

The H_2-TPR results presented in Fig. 4.13 confirm the integrity of $Fe(NiFe)O_4$-SiO_2 catalyst for hydroprocessing reaction via a non-hydrogen spillover route. The analysis was focused on the reduction of active metal M^{n+} specifically Ni^{2+}, and testing the reducibility of metal oxide (Fe_3O_4 and SiO_2) support materials. The H_2-TPR profiles of $Fe(NiFe)O_4$-SiO_2, SiO_2, and Fe_3O_4 reveal that the cationic Si of SiO_2 is non-reducible. Bulk Fe_3O_4 shows a large peak at around 643 ^oC with the consumption of 2452 µmol/g, indicating the conversion of Fe_3O_4 to FeO. Also, the inactivated $Fe(NiFe)O_4$-SiO_2 catalyst exhibited three reduction peaks centered at 408, 448 and 611 ^oC while consuming 4972 µmol/g H_2. This observation suggests reduction of Ni^{2+} to Ni^{+}, Ni^{+} to Ni^{o} and Fe_3O_4 to FeO, respectively. The reduction temperature range for Ni^{2+} in $Fe(NiFe)O_4$-SiO_2 lies between 400-500 ^oC. Since SiO_2 is non-reducible metal oxide up to 700 ^oC and Fe_3O_4 is only reducible at > 600 ^oC, spillover of hydrogen over SiO_2, Fe_3O_4 or Fe_3O_4-SiO_2 at < 600 ^oC hydro-processing temperature is energetically highly

University of Malaya

impossible. This is due to the fact that spillover implies hydrogen acts as a proton when dissociated by active metal and then donates an electron to support cation that are reducible in a very low activation energy process. Conversely, these support materials are non-reducible at 250 ^{o}C, which is the process condition in this present study, and that implies high activation energy for electron transfer from hydrogen atom to either cationic Si in SiO_2 or Fe in Fe_3O_4. In this regard, according to valence bond theory, hydrogen is passive to form a chemical bond with atoms that have saturated bonds, such as Si and Fe in oxide states. Consequently, appreciable energy beyond 700 ^{o}C up to 1115-1630 ^{o}C for instance will cause a SiO_2 reduction after that hydrogen spillover prevails. However, this is condition apparently higher than reported temperature of 400 ^{o}C for hydroprocessing. Conclusively, SiO_2 is passive to reduction because 0 mol/g H_2 was consumed over 30-700 ^{o}C at 10 ^{o}C/min ramping in 10 mL/min flow of H_2. This implies unpaired electrons in hydrogen atom orbital require high energy to have the right symmetry of interaction with the orbitals of the Si in SiO_2 to form a dissociative bond. Hence, the presence of grain boundaries observed at around (311) and (511) plane of the active phase containing nickel from HRTEM image of $Fe(NiFe)O_4$-SiO_2 is suggested to be in the form of surface defects that tune the structural superiority of the catalyst for the hydrogenation of furfural at the edge sites to selectively yield the furfuryl alcohol. The estimated surface density (34.331W/nm^2) of the $Fe(NiFe)O_4$-SiO_2 catalyst is also informatively high enough to aid suggestion of another form of external surface defect where surface octahedral nickel atoms have unsatisfied bonds and high surface energy than the bulk. Consequently surface relaxation and reconstruction involving change in periodicity of surface structure and small coordinated movement of atoms in the topmost layer to reduce the unsatisfied bond results in external surface defect. Concurring with this symmetry, dissociated hydrogen atom is suggested to be transported via molecular or eddy diffusion around the spatial domain of the active Ni

University of Malaya

metal while considering the stereochemistry of the substrate. This is because 1200 rpm, one of the process parameters used in this study, is enough to create a chaotic flow regime in line with the Kolmogorov length scales that serves as a parameter for eddy diffusion. The temperature range 90-250 ^{o}C is also another parameter that may improve the fugacity of the H_2 gas phase and therefore induces molecular diffusion.

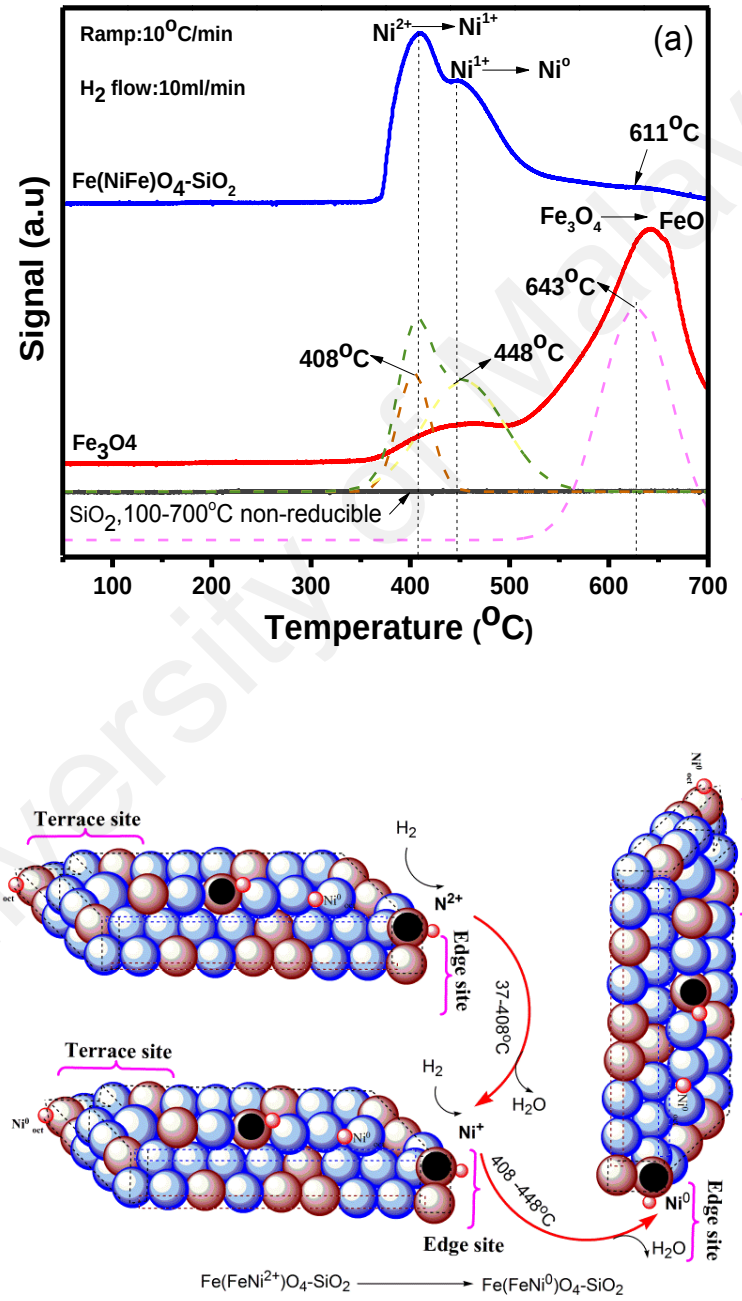

Fig. 4.13: (a) H_2-TRP profile of $Fe(NiFe)O_4$-SiO_2 and (b) mechanism of $Fe(NiFe)O_4$-SiO_2 reducibility.

University of Malaya

4.2.9 NH_3-TPD analysis for $Fe(MFe)O_4$-SiO_2 catalysts

The NH_3-TPD profile in Fig 4.14 indicates ammonia desorption peaks at 350 ^oC and 400^oC for $Fe(NiFe)O_4$-SiO_2; 310 ^oC and 405 ^oC for $Fe(RuFe)O_4$-SiO_2. These peaks are assigned to chemosorb NH_3 on medium and strong acid sites and the desorption temperature range is similar to the report one in literature; 280-330 ^oC and 380-500^oC is attributed to medium and strong acid sites (Ghoreishi & Yarmo, 2013)

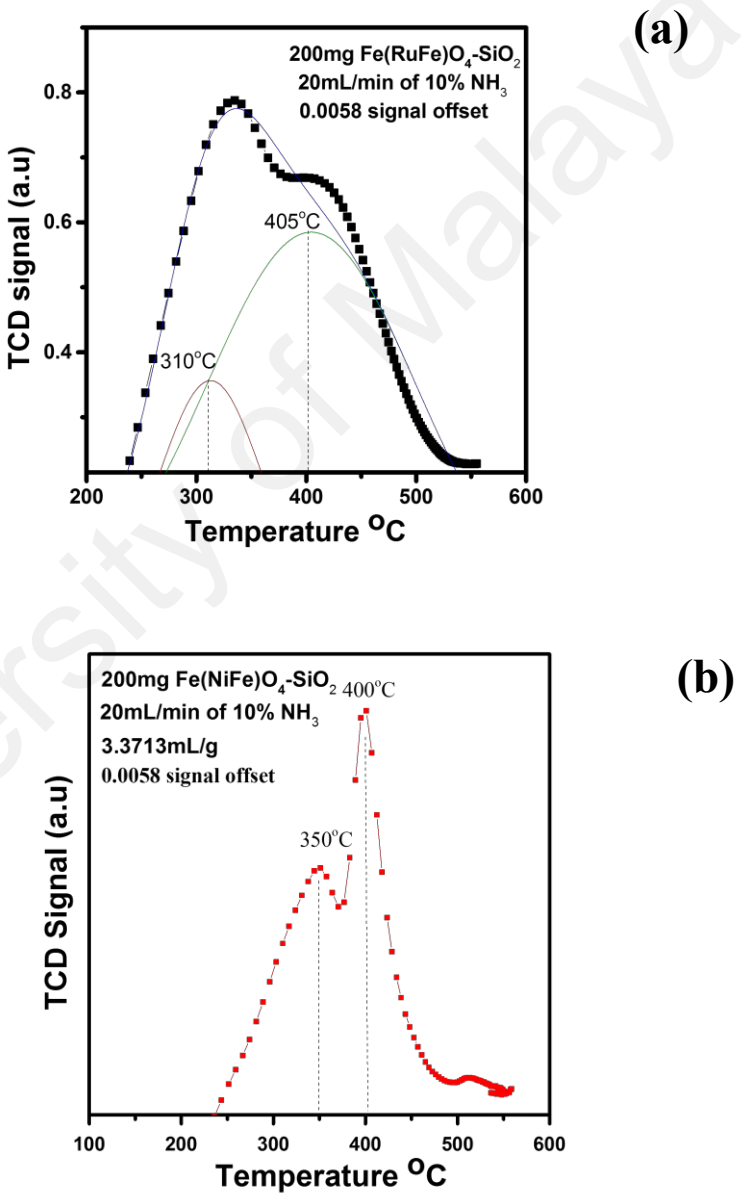

Fig. 4.14: (a) Deconvoluted NH_3-TPD profile of $Fe(RuFe)O_4$-SiO_2 and (b) NH_3-TPD Profile of $Fe(NiFe)O_4$-SiO_2.

University of Malaya

4.2.10 X-ray photoemission spectroscopy (XPS) for $Fe(MFe)O_4$-SiO_2 catalyst

Insights into the stochastic of surface atoms in $Fe(MFe)O_4$-SiO_2 catalysts could be better understood via a surface sensitive analysis, such as X-ray photoelectron spectroscopy. This is because the co-ordinations of Fe^{n+}, M^{n+} (M = Ni and Ru), and Si^{4+} to O^{2-} point charges to form $Fe(MFe)O_4$-SiO_2 involve the bonding orbitals and anti-bonding orbitals present in the bulk and at the surface nodes, respectively. Since the synthesized magnetic catalysts have polyatomic structure, the delocalization of electrons from O^{2-} point charges to coordinate with Fe^{n+}, M^{n+} and Si^{4+} is possible, thus forming an inverse spinel structure. In this regard, a survey scan as shown in Fig 4.15 (a) and (b) confirms the presence of Fe, Si, Ni, Ru, and O surface atoms in the magnetic $Fe(MFe)O_4$-SiO_2 catalysts.

Fig 4.15(c) confirms the presence of active metals (M = Ni and Ru) in magnetic $Fe(MFe)O_4$-SiO_2 catalysts by identifying the peaks centered at binding energies of ~280.74 and 284.59 eV for Ru; ~852.52 eV, 854.72 eV and 856.1eV for Ni 2p. The first peak corresponds to Ru^{3+} $3d_{5/2}$ and Ru^{3+} $3d_{1/2}$; Ni $2p_{3/2}$.

Fig 4.15 (d) shows the Fe 2p XPS spectra of magnetic $Fe(MFe)O_4$-SiO_2 catalysts. Two binding energies can be found at about 724.44 (Fe $2p_{1/2}$) and 711.09 eV (Fe $2p_{3/2}$) for $Fe(RuFe)O_4$-SiO_2 and ~724.57 (Fe $2p_{1/2}$) and 711.40 eV (Fe $2p_{3/2}$) eV for $Fe(NiFe)O_4$-SiO_2. These binding energies can be assigned to Fe^{3+} and Fe^{2+}, respectively, providing insights on stoichiometric formation of a Fe_3O_4 phase in $Fe(MFe)O_4$-SiO_2 catalysts. The absence of a satellite peak at ~718.78 eV for $Fe(NiFe)O_4$-SiO_2 and $Fe(RuFe)O_4$-SiO_2 spectra reveals that no free γ-Fe_2O_3 hematite impurities are present in magnetic $Fe(RuFe)O_4$-SiO_2 catalysts, in line with the literature reports (Monti *et al.,* 2012). However, the noticed binding energies at around ~709 and ~712 eV indicate the

University of Malaya

existence of both Fe^{2+} and Fe^{3+}, respectively, reconfirming the formation of a Fe_3O_4 phase in the developed magnetic $Fe(MFe)O_4$-SiO_2 nanocatalyst.

In Fig 4.15(e), two strong Si 2p signals are found at ~102 and 103 eV, indicating the presence of Si. Since Si is tetravalent coordinated species, we suggest that the point charge delocalization at specific Si node enhances the formation of Si-O-Fe linkages as indicated in the binding energies at around 103 and 102 eV for siloxane (Si-O-Si) linkages. These observations suggest transient stoichiometric formation of a SiO_2 phase during condensation to $Fe(MFe)O_4$-SiO_2 catalysts.

Fig 4.15(f) confirms the presence of O^{2-} point charges in $Fe(MFe)O_4$-SiO_2 catalysts. The presence of O^{2-} 1s peak at ~530.86 eV indicates either octahedral or tetrahedral coordination to magnetite, whereas the peak at ~532.86 eV can be assigned to siloxane coordination. These binding energies reveal that delocalized point charge in polyatomic $Fe(MFe)O_4$-SiO_2 has coordination with Fe^{n+} and Si^{n+}. However, O^{2-} point charges have low crystal field splitting of an octahedral coordinated ion, like Br^-, Cl^-, F^-, SO_4^{2-}, which is enough to limit the d-electron to spin and reside in the d_{xy}, d_{xz}, and d_{yz} orbitals.(Grosvenor, Kobe, Biesinger, & McIntyre, 2004) Expanding further in the case of $Fe(MFe)O_4$-SiO_2 catalysts, the Fe^{3+} cations have high spin and Fe^{2+} cations contain either high spin or low spin depending on the point charge. Since low spin Fe^{2+} species cannot have multiple splitting, only a single Fe $2p_{3/2}$ peak representing at around 720 and 705 eV exists. The binding energy of Fe $2p_{3/2}$ photoelectron is dependent on the electronegativity of the ligand. As the electronegativity of the ligand increases, the binding energy of Fe $2p_{3/2}$ (Fe^{3+}) increases. This is because the increased positive character of Fe $2p_{3/2}$ reduces overall shielding effect of Fe^{3+} nucleus, hence higher amount of energy is required to promote a Fe 2p electron to the Fermi level.

University of Malaya

Consequently, when a different ligand from O^{2-} is employed in the matrix of $Fe(MFe)O_4$-SiO_2, these phenomena are expected.

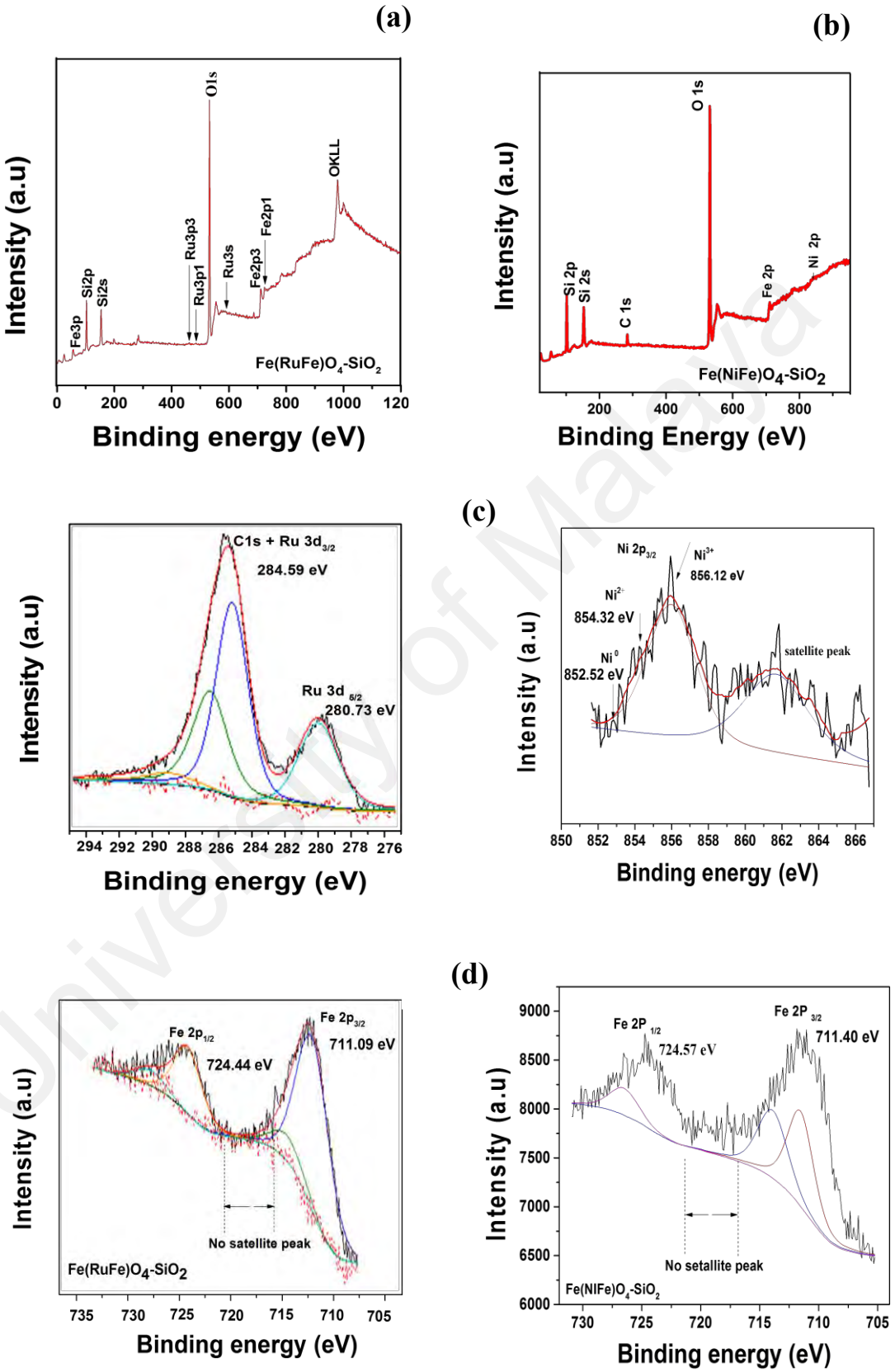

University of Malaya

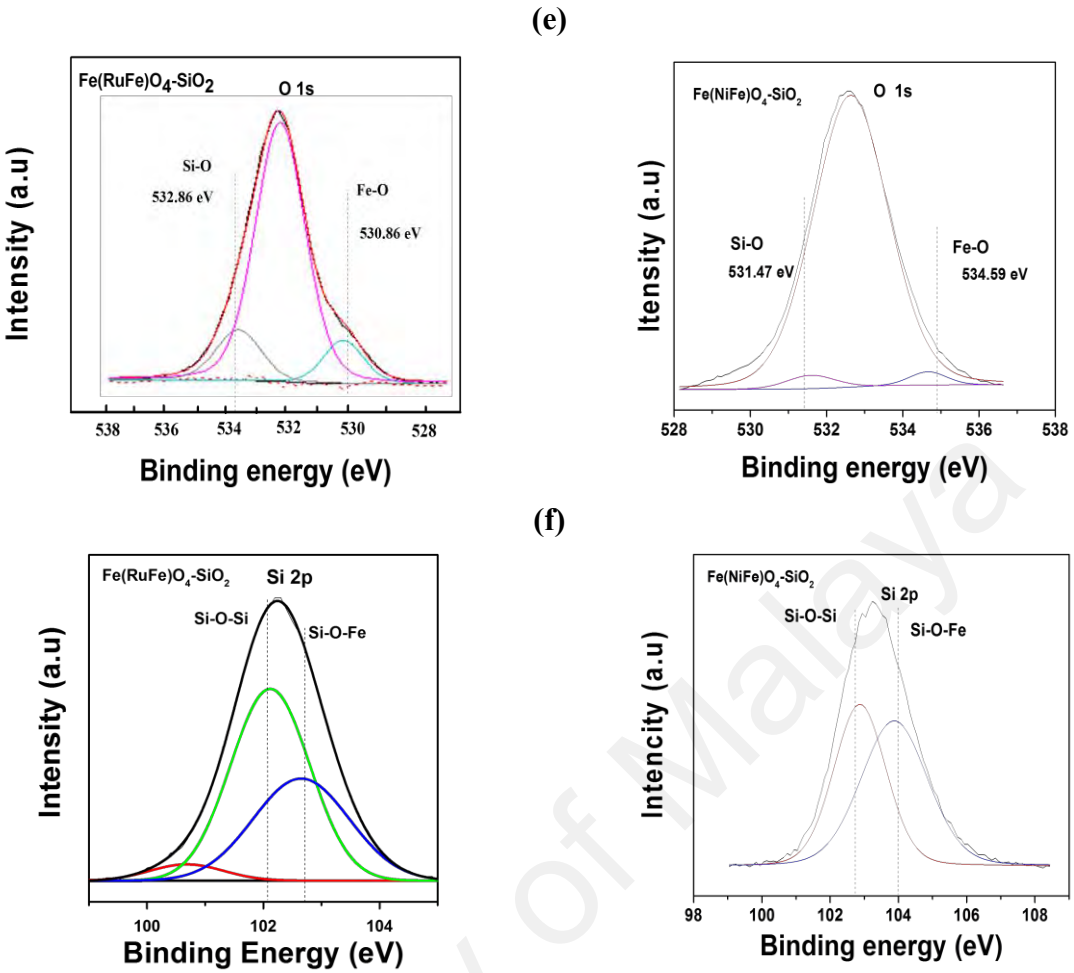

Fig. 4.15: (a) Survey spectra of $Fe(RuFe)O_4$-SiO_2 catalyst, (b) survey spectra of $Fe(NiFe)O_4$-SiO_2 catalyst, (c) Ru 3d spectrum of $Fe(RuFe)O_4$-SiO_2 and Ni 2p of $Fe(NiFe)O_4$-SiO_2 catalyst, (d) Fe 2p spectra of $Fe(MFe)O_4$-SiO_2 (M = Ru and Ni) catalysts, (e) O 1s spectra of $Fe(MFe)O_4$-SiO_2 (M = Ru and Ni) catalysts and (f) Si 2p spectra of $Fe(MFe)O_4$-SiO_2 (M = Ru and Ni) catalysts.

4.3 $Fe(MFe)O_4$-SiO_2 catalyst activity

4.3.1 Screening studies

The screening studies was undertaken in order to isolate the working catalyst for the experiments. First, five different Ni loadings (0.02, 0.31, 0.41, 0.51wt %) in $Fe(NiFe)O_4$-SiO_2 were prepared and their activity is as shown in Fig 4.16 (a). Under the vapour phase hydrogenation of furfural to furfuryl alcohol at 250 ^oC, 5 bar, 1200 rpm, and 4 h the activity was measured. The conversion increases as Ni loading was increased and 0.51wt% Ni in $Fe(NiFe)O_4$-SiO_2 gave the highest

University of Malaya

performance. This loading was used throughout the study. Secondly, the reaction time was screened in the range (1h, 2h, 3h, 4h and 5h). 4h reaction time was selected because it gave minimum error as shown in Fig 4.16 (b). Equally, the reactions were also conducted without $Fe(NiFe)O_4$-SiO_2 catalyst and with Fe_3O_4-SiO_2 as well as un-activated $Fe(NiFe)O_4$-SiO_2 catalyst; all gave no observable conversion of furfural to any product at that 90 ^oC to 150 ^oC and 20 bar.

Fig. 4.16 presents the effect of time during vapor phase hydrogenation of furfural to furfuryl alcohol. During the process, time was varied from 1h until 5h. In all these time, concentration of furfural was reducing because conversion was increasing. However, through the other activity test for other parameter such as pressure, temperature catalyst amount, reactant amount, 4 h reaction time was selected by adjusting other parameter to compensate for the time.

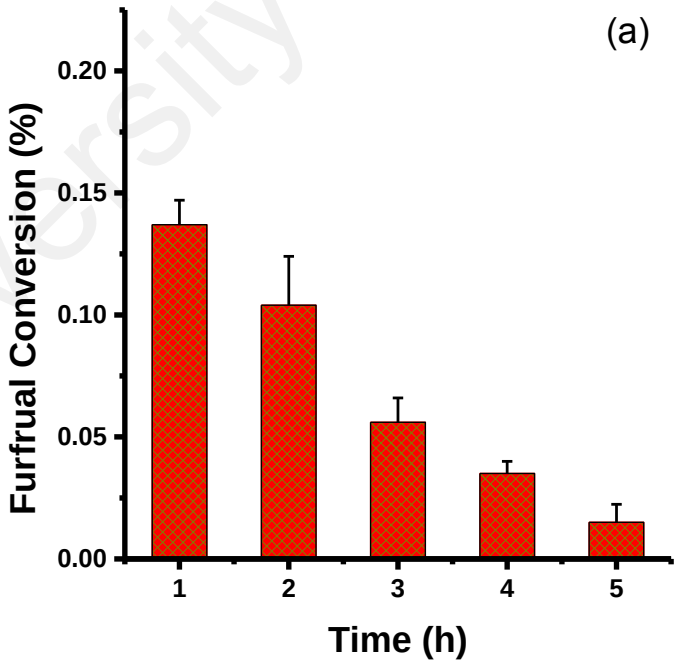

University of Malaya

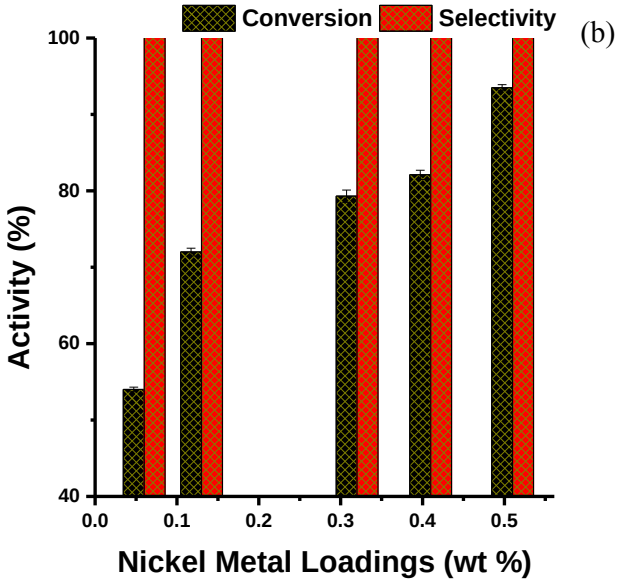

Fig. 4.16: **(a) Screening time (b) Screening nickel loading.**

4.3.2 Effect of pressure and temperature during hydrogenation of furfural over $Fe(NiFe)O_4$-SiO_2 catalyst

The effect of H_2 pressure and reaction temperature was studied for the hydrogenation of furfural to furfuryl alcohol for 4 h and the results are presented in Fig. 4.17 (a) and 4.17 (b), respectively. The furfural conversion is considerably dependent on the H_2 pressure and temperature. In contrast, the selectivity of furfural (~100%) remains the same at all the reaction conditions. The effect of hydrogen pressure on furfural hydrogenation was studied while fixing the temperature at 250 °C for hydrogen pressure of 1 to 20 bar at 20 V/V% furfural concentration and 60 mg $Fe(NiFe)O_4$-SiO_2 nanocatalyst. As shown in Fig. 4.17 (a), the conversion of furfural increases when the H_2 pressure increase from 1 to 5 bar and then, the conversion of furfural decreases with the increase of H_2 pressure. As well, the effect of reaction temperature was studied in the range of 90 to 250 °C at 20 bar H_2 pressure for 4 h (Fig. 4.17b). When the temperature increase from 90, 150, 180 to 250 °C, a decrease in the conversion of furfural was found in the trend of 94.3, 93.6, 92.9 and 92.6%, respectively, for 60 mg

University of Malaya

magnetic $Fe(NiFe)O_4$-SiO_2 nanocatalyst. Fig. 4.17 indicates that 90 °C, 20 bars and 250 °C, 5 bars combinations gave the best furfural conversions with ~94.3 and 93.5%, respectively. These phenomena are justified from molecular and eddy diffusion enhancement at higher and lower conditions of H_2 pressure and temperature on the catalyst surface. The former, guided by kinetic theory, is influenced quantitatively by high temperature where the low pressure is required. The latter, guided by turbulence phenomena, is induced further by 1200 rpm revolution, which creates higher pressure and internal heating, therefore low temperature is required.

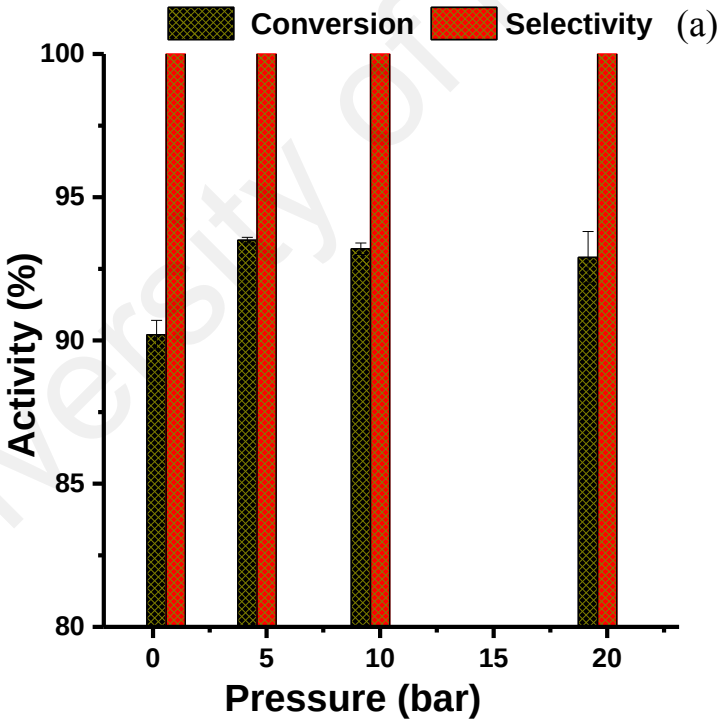

University of Malaya

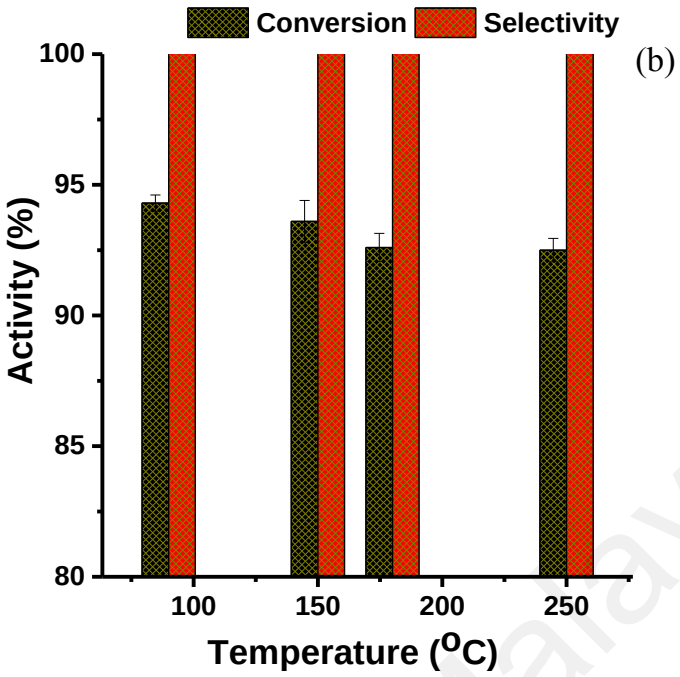

Fig. 4.17: (a) Effects of hydrogen partial pressure (250 °C and 60 mg catalyst); (b) reaction temperature (20 bar and 60 mg catalyst) on conversion of furfural and selectivity towards furfuryl alcohol for 20 V/V% furfural concentration. Standard deviations from GC analysis of furfural conversion and furfuryl selectivity are ± 3 and ± 2, respectively.

4.3.3 Effect of catalyst amount and reactant concentration during hydrogenation of furfural over $Fe(NiFe)O_4$-SiO_2 catalyst.

The effect of catalyst amount, furfural concentration, and Ni loading on the conversion of furfural and selectivity towards furfuryl alcohol was studied using heptane as a solvent and the results are presented in Fig. 4.18 (a), 4.18 (b), and 4.18 (c), respectively. The conversion of furfural increases from 92.9 to 95% as the catalyst amount increases from 20 to 60 mg (Fig. 4.18 (a). Interestingly, 100% selectivity towards furfuryl alcohol was obtained at all catalyst loadings. These results indicate that more number of active sites are availble for the reaction at higher catalyst loadings, hence a higher conversion of furfural.

University of Malaya

In contrast, the conversion of furfural decreases as the volume of furfural in heptane increases for 60 mg magnetite $Fe(NiFe)O_4$-SiO_2 nanocatalyst (Fig. 4.18b). This is justified by the fact that the available active nickel sites for furfural hydrogenation gradually decrease with the increase of furfural concentration. Therefore, the number of molecules for a known volume of furfural and the number of particles for a known amount of catalyst with Ni active phase are highly related. Therefore, a decrease in furfural conversion with its volume increases could be attributed to the fact that there are no additional active sites to transform the carbonyl functionality in furfural at higher furfural concentration.

The activity of the catalyst increases with the increase of Ni loading from 0 to 0.51 wt. % during the screening process. This indicates that higher numbers of active phase Ni species are available to dissociate H_2 into proton and hydride at higher Ni loading, hence high conversion of furfural. Concurrently, excess amount of Ni is not essential for this reaction because 0.51 wt% Ni loading catalyst gives 94.3% conversion of furfural and 100% selectivity of furfuryl alcohol. This is against 5 wt.% Ni/SiO_2 activity that was reported to give a wide range of products due to ring opening through decarbonylation step as seen in Fig. 4.19 (Sitthisa & Resasco, 2011) Therefore, low nickel content in $Fe(NiFe)O_4$-SiO_2 is insightful that high amount of Ni metal is not necessary to obtain appreciable activity in furfural hydrogenation. This indicates the superior selectivity of magnetic $Fe(NiFe)O_4$-SiO_2 nano catalyst over the conventional Ni/SiO_2 in the hydrogenation of furfural to obtain high yields of the desired products.

University of Malaya

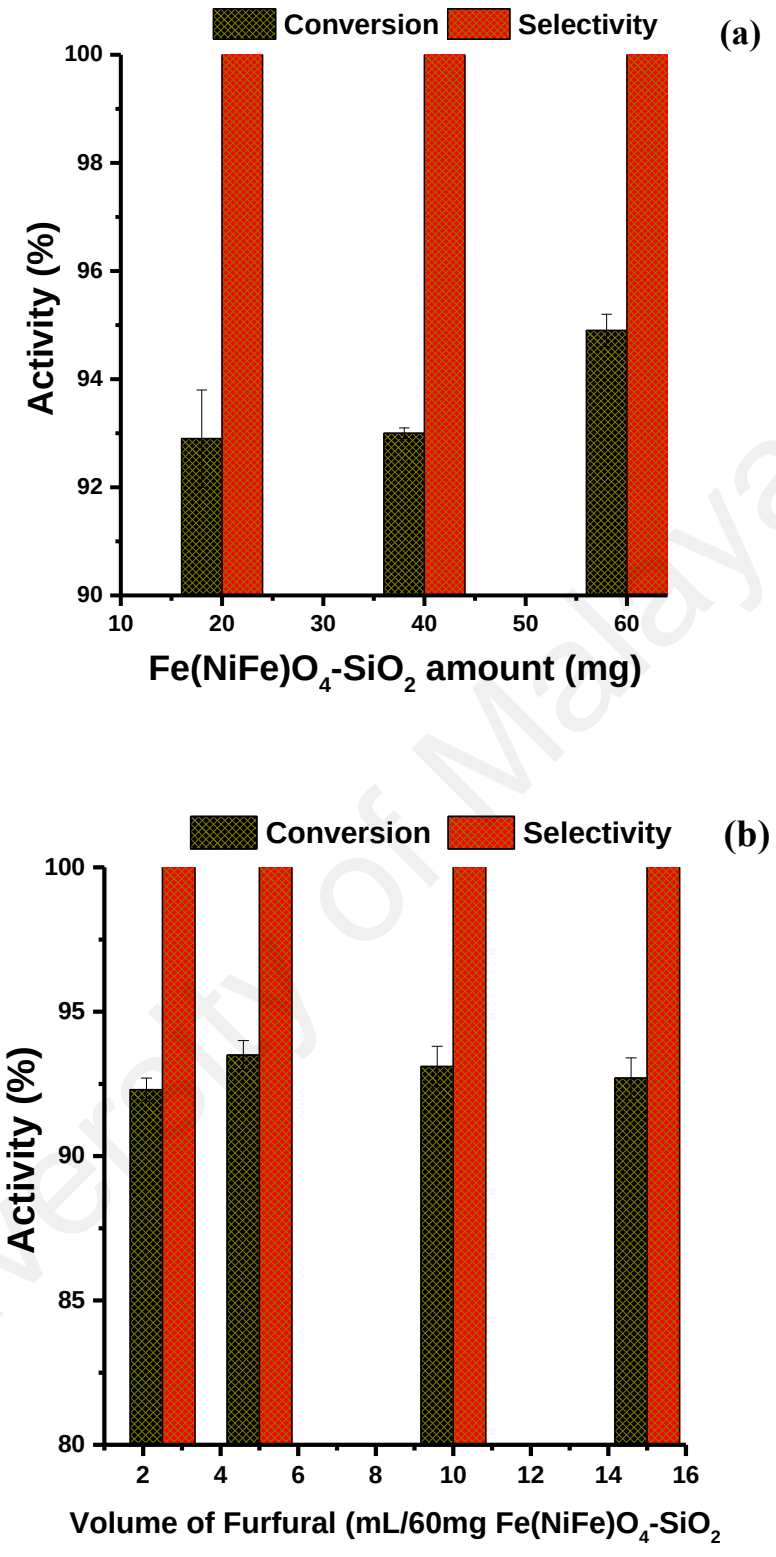

Fig. 4.18: Effect of (a) catalyst amount, (b) quantity of furfural, and (c) Ni loading on the catalytic efficiency of magnetic $Fe(NiFe)O_4$-SiO_2 nanoparticles for the hydrogenation of furfural at 20 bar, 250 °C, 4 h, and 1200 rpm. Standard deviations from GC analysis of furfural conversion and Furfuryl selectivity are ± 3 and ± 2, respectively.

University of Malaya

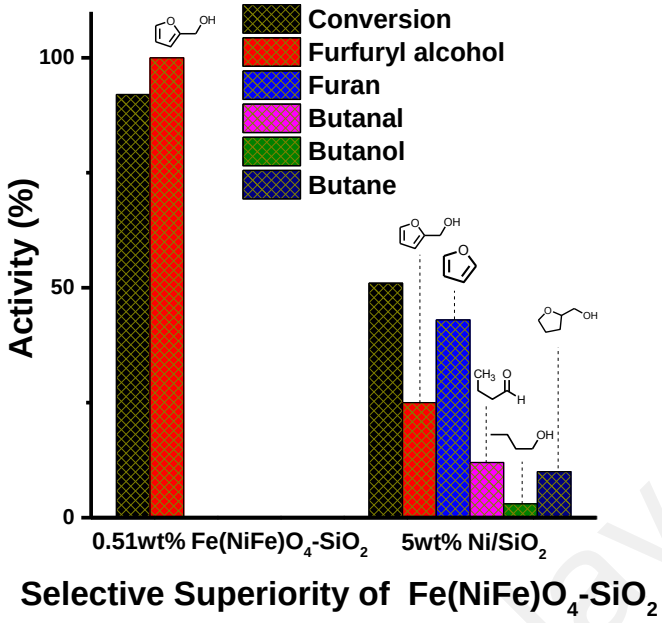

Fig: 4.19: Selective superiority of magnetic 0.51 wt% $Fe(NiFe)O_4$-SiO_2 nanoparticle catalyst to 5 wt% Ni/SiO_2 in the hydrogenation of furfural.

4.3.4 Synergy between distributions of $Fe(MFe)O_4$-SiO_2 nanoparticle size with catalytic activity.

$Fe(MFe)O_4$-SiO_2 where M = Ni, have been demonstrated to be active in selective hydrogenation of furfural to furfuryl alcohol at 20 bar, 90 ^oC and 5bar, 250 ^oC conditions respectively (Halilu et al., 2016). However, Fig 5.8 shows an extension of the studies on the activity of $Fe(MFe)O_4$-SiO_2 at 250 ^oC and 90bar. Gross distributions of products were obtained for different $Fe(MFe)O_4$-SiO_2 catalyst and were attributed to the structural superiority of the catalysts. No two crystallite size gave same activity. This is attributed to catalyst surface defect that was evidenced in our previous studies (Halilu et al., 2016), and extended in this study. As seen previously, all the catalysts have different surface density and it is a form of defect that could aid suggestion on presence of edge and terrace sites on each catalyst surface. This is typically due to surface atom rearrangement in this case. In this regard, some reactions steps were postulated to take place at the edge, while others at the terraces sites. The mechanism

University of Malaya

which guides these processes has a first stage for vanillin postulated to take place at the edge. These involve formation of vanillyl alcohol, while the last five stages were postulated to take place at the terrace sites. These involve formation of cyclohexanone, cyclohexanol, cyclohexane guaiacol, and phenol as potential fuel grade molecules. Also, the first stage in the case of furfural hydro-processing have been reported in our previous study and postulated to take place at the edge.

Fig 4.20 and 4.21 show the effect of heat treatment (from at 400, 500, 600 to 700 ^{o}C) on the catalytic performance of Fe(MFe)O_4-SiO_2 catalysts in hydro-processing of vanillin and furfural, respectively. In all the cases, the conversion of vanillin and furfural are ~100% and various products can be found in both hydro-processing reactions. It is indicative from Fig 4.20 that ~56.3 % highest selectivity of cyclohexanone product was found for Fe(NiFe)O_4-SiO_2 catalyst calcined at 400 ^{o}C. Interestingly, the selectivity of cyclohexanone drastically decreased, along with the increase of cyclohexane with corresponding selectivity of 19.99 %, 54.9 % and 53.7% for 500 ^{o}C, 600 ^{o}C and 700 ^{o}C Fe(NiFe)O_4-SiO_2 catalyst treatment temperatures. Compared to all the heat treatments, 32.8% selectivity of cyclohexanol product was found for 700 ^{o}C treated Fe(NiFe)O_4-SiO_2 catalyst. On the other hand, a broad range of products selectivity was found in the case of Fe(RuFe)O_4-SiO_2 catalyst. Except for 500 ^{o}C treated catalyst with 49.8% selectivity towards cyclohexane, 41.8% selectivity of cyclohexanol product was found for Fe(RuFe)O_4-SiO_2 catalyst treated at 700 ^{o}C. Despite the heat treatment employed, a considerable quantity of guaiacol was also formed with selectivity > 10% in hydro-processing of vanillin with the Fe(RuFe)O_4-SiO_2 catalyst.

In the case of hydro-processing of furfural as shown in Fig. 4.21, three major products, such as furfuryl alcohol, tetrahydrofuran, and pentane are formed for magnetic

University of Malaya

$Fe(MFe)O_4$-SiO_2 catalysts. Except for 700 ^oC treated $Fe(NiFe)O_4$-SiO_2 catalyst (pentane is the major product), a high selectivity of tetrahydrofuran is found with the both $Fe(NiFe)O_4$-SiO_2 and $Fe(RuFe)O_4$-SiO_2 catalysts. Among those, the $Fe(RuFe)O_4$-SiO_2 catalyst treated at 600 ^oC shows a high selectivity of tetrahydrofuran in hydro-processing of furfural. The formation of various products in hydro-processing of furfural and vanillin could be due to the surface structural disparities of the catalysts. This is also attributed to catalyst surface defects from unsatisfied bonds, forming the edge and terrace sites on each catalyst surface matrix. In this regard, some reactions steps can be possible at the edge site, while others at the terraces site (Fig 4.24 and 4.25).

(a)

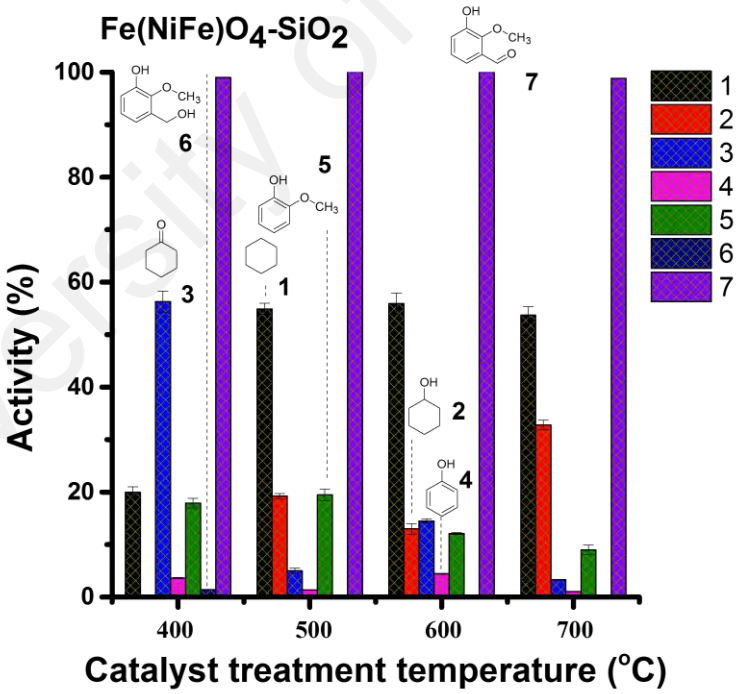

University of Malaya

(b)

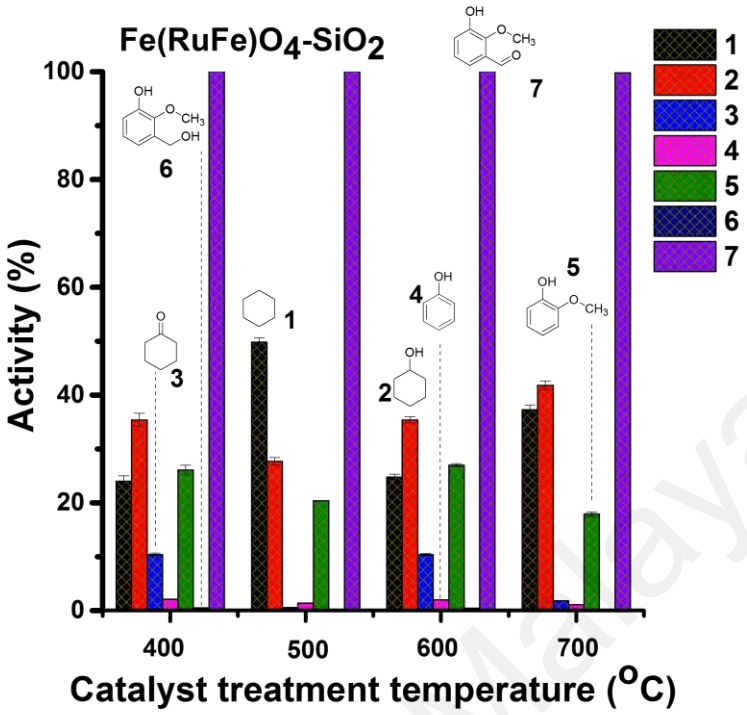

Fig 4.20: Product distribution for hydro-processing of vanillin over (a) $Fe(NiFe)O_4$-SiO_2 and (b) $Fe(NiFe)O_4$-SiO_2 catalysts at 250 °C, 90 bar H_2, 800 rpm, and 5 h. Products: 1 = cyclohexane, 2 = cyclohexanol, 3 = cyclohexanone, 4 = phenol, 5 = guaiacol, and 6 = vanillyl alcohol and 7 = vanillin. Standard deviations from GC analysis of vanillin conversion and product distribution are ± 2 and ± 1%, respectively.

(a)

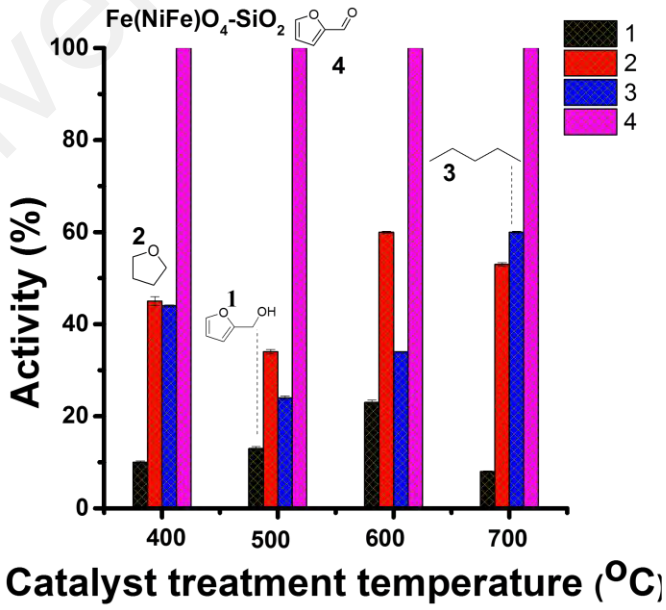

University of Malaya

(b)

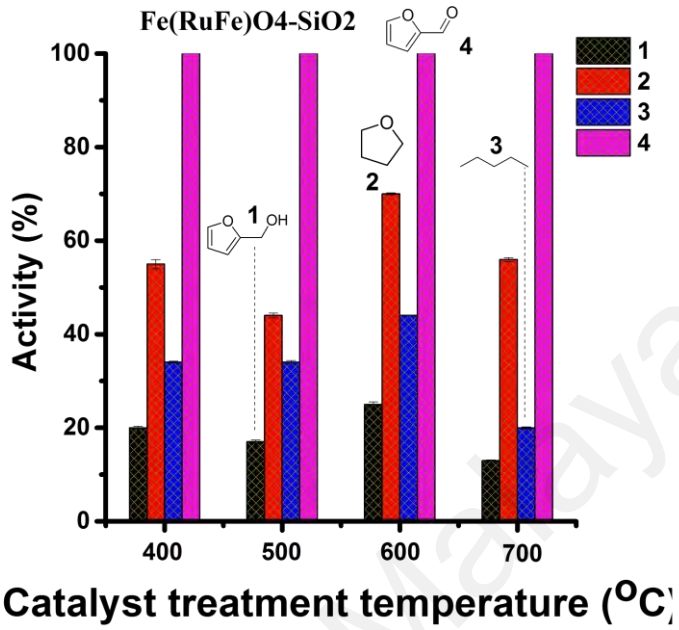

Fig 4.21: Product distribution for furfural hydro-processing over (a) $Fe(NiFe)O_4$-SiO_2 and (b) $Fe(RuFe)O_4$-SiO_2 catalysts at 250°C, 90bar H_2, 800rpm, 5h (1= furfuryl alcohol, 2 = tetrahydrofuran, 3 = pentane, 4 = 100% conversion of furfural) Standard deviations from GC analysis of furfural conversion and product distribution are ± 2 and ± 1, respectively.

4.3.5 Catalyst recoverability and reusability study

$Fe(MFe)O_4$-SiO_2 reusability studies were conducted until six cycles. It is evident that the activity drops sequentially, and this is sufficient to aid suggestion on reactivity of the catalyst up to six cycles. The recoverability of the catalyst is almost 100 % as demonstrated in table 4.2 and appendix A. Due to loss in catalyst active phase reusability decreases.

University of Malaya

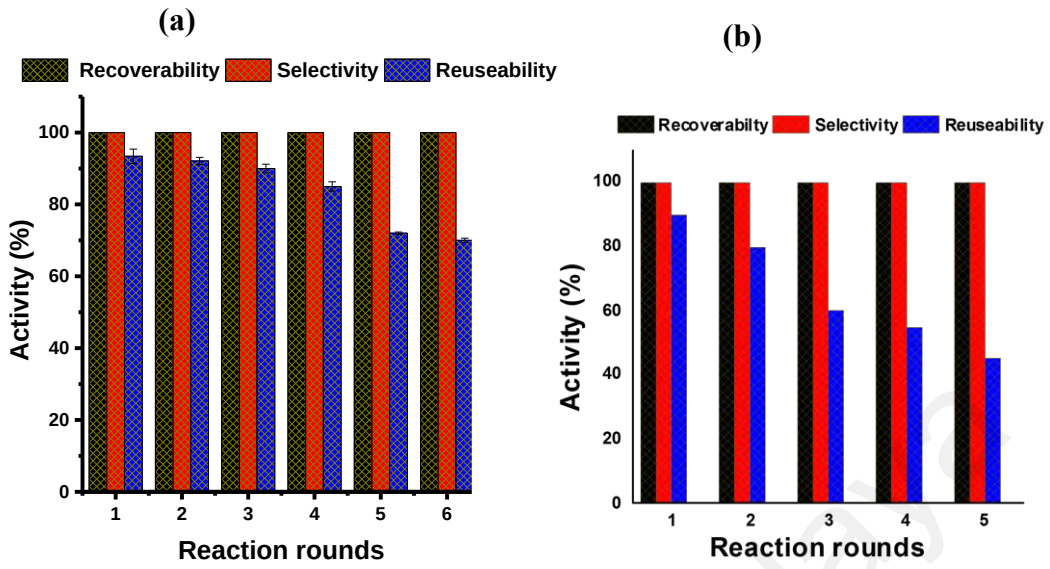

Fig. 4.22: (a) $Fe(NiFe)O_4$-SiO_2 and (b) $Fe(RuFe)O_4$-SiO_2 catalyst recoverability, selectivity and reusability

Table 4.2: Catalyst $Fe(NiFe)O_4$-SiO_2 recoverability

S/N	Weight of catalyst before reaction	Weight of catalyst after reaction
1	60mg	~60mg
2	60mg	~60mg
3	60mg	~60mg
4	60mg	~60mg
5	60mg	~60mg
6	60mg	~60mg

4.4 Proposed mechanisms for surface reaction over $Fe(MFe)O_4$-SiO_2 catalyst

The pathway for the hydrogenation of furfural to furfuryl alcohol over the $Fe(NiFe)O_4$-SiO_2 catalyst was presented in Fig 4.23. As shown in the Figure, Ni metal dissociates hydrogen molecule (H_2) into proton and hydride. The positive character of

University of Malaya

the carbon increases due to the electronegativity difference between the carbon and oxygen. The formed hydride (H^-), a nucleophile, attacks the C (sp^2)-O carbonyl carbon in furfural. Electron moves from the HOMO of the nucleophile into the LUMO of the electrophile. As a result, the electron pair in its HOMO starts to interact with the LUMO (antibonding π) to form a new δ bond. Therefore, trigonal C (sp^2)-O carbon in carbonyl changes to tetragonal C (sp^3)-O hybridized state in Furfuryl alcohol following additional protonation step. This induced mesmeric effect can lead to overall Furfuryl alcohol production. According to Monte Carlo statistical mechanic technique on the conformational equilibrium of furfural, furfuryl carbonyl group rotates along the furan ring. Therefore, adsorption takes place at the furan ring terminal oxygen atom by hydrogen or van der Waals bonding. The H_2-TPR studies reveal that SiO_2 is non-reducible up to 700 ^oC, thus it is a non-reducible support within the hydrogenation condition used in this study. Consequently, the mechanism that propagates hydrogen consumption is energetically highly unlikely to occur via hydrogen spillover on this support material. Therefore, we postulate that surface defects present on Ni metal and molecular diffusion of hydrogen around the spatial domain of Ni metal induces the reaction mechanism.

As an extension, time dependent density functional theory calculations (TD-DFT) estimated using the B3LYP functional revealed that furfural poses 71 alpha molecular orbitals having different excitation energies: 25 are HOMOs and 46 are LUMOs (Figure S1). Similarly, vanillin poses 115 alpha molecular orbitals: 40 are HOMOs and 75 are LUMOs (Appendix G). The prevalent LUMOs in both structures give plenty of room for electronic excitations from the HOMOs at a specific spin. Furfural is observed to be in stable equilibrium state because the curvature of the potential energy surfaces of furfural molecules is upward, hence all the frequencies are positive (Appendix G). Conversely, vanillin was observed to be in an unstable equilibrium state because the

University of Malaya

curvature of the potential energy surfaces of vanillin molecules is downward at an arbitrary vibration frequency of -80.73 cm^{-1} (Appendix G). Therefore, the TD-DFT calculations reveal that HOMOs and LUMOs of furfural have more electronic density distributions to the carbonyl symmetry and also to the π-electrons around the carbonyl symmetry. Similarly, vanillin has high electronic density around the carbonyl symmetry as well as the overall benzene ring. Based preliminary calculations and products distribution in hydro-processing reactions, reaction pathways for hydro-processing of vanillin (Fig 4.24) and furfural (Fig 4.25) at 250 ^{o}C and 90 bar H_2 were postulated. It was found that active metal (M = Ni or Ru) and acid functions of mesoporous magnetic Fe(MFe)O_4-SiO_2 nanocatalyst play a key role in hydro-processing of biomass-derived molecules by interacting with the oxygenates around high electron density region of the carbonyl symmetry and the benzene ring (Fig 4.24 and Appendix G, Fig S1). The hydro-processing of vanillin (Fig 4.24) over magnetic Fe(MFe)O_4-SiO_2 catalysts gives vanillyl alcohol, guaiacol, phenol, cyclohexanone cyclohexanol, and cyclohexane, while furfuryl alcohol, tetrahydrofuran, and pentane are formed in hydro-processing of furfural (Fig 4.24). As shown in Fig 4.24, the transformation of vanillin to a particular product was initiated with four potential C-O bonds having different bond dissociation energies (BDEs) i.e. C(sp^3)-OAr (~262-276 kJ/mol), C(sp^2)-OMe, (~409-421 kJ/mol), C(sp^2)-OH (~466 kJ/mol) and C($_Sp^2$)-O (~732 kJ/mol). Similarly, C(sp^2)-O bond present in furfural induces its transformation into various products as shown in Fig 4.24. In addition to non-hydrogen spillover attributes of Fe(MFe)O_4-SiO_2 catalyst, bond dissociation energies (BDE) of the feedstock substrates and textural properties of tuned magnetic Fe(MFe)O_4-SiO_2 catalysts could play a key role in the transformation of furfural and vanillin into various products.

On the basis of BDEs, it can be suggested that the bond cleavage order during hydrogenolysis or hydro-deoxygenation of vanillin follows: C(sp^3)-OAr < C(sp^2)-OMe

University of Malaya

< $C(sp^2)$-OH < $C(_Sp^2)$-O, while considering high electron density distribution around the carbonyl symmetry. The BDEs correspond to the temperature of ~138-145, ~215-222, ~245, and ~385 ^oC, respectively. However, the bond cleavage will follow direct C-O cleavage with the attack of hydrogen at the ipso position (-OH) and meso ($-OCH_3$) followed by hydrogenation at the ortho position and then dehydration step. This reaction pathway is initiated by tautomerization as shown in Fig 4.24. The hydroxyl group can also be deuterated through H/D exchange as reported previously. Similar trends are also possible for hydro-processing of furfural by considering the electron density distribution around the carbonyl functionality that encourage the furfural for hydrogen attack and subsequent decarbonylation at 250 ^oC and 90 bar H_2 operating conditions.

In line with this background, the formation of fuel grade components from vanillin, such as cyclohexanol and cyclohexane is possible from the formation of phenol from guaiacol. It is therefore plausible to note that phenol in the presence of Lewis acid site forms phenoxide because one of the carbon in the aromatic ring becomes highly electrophilic and thereby receptive to electrophiles, such as H^+ which is obtained from the dissociation of H_2 over metal active phase in $Fe(MFe)O_4$-SiO_2 catalysts. As shown NH_3 TPD section previously, there is an obvious evidence of acidic strength occurring at 310 ^oC and 405 ^oC, 350 ^oC and 400 ^oC for $Fe(RuFe)O_4$-SiO_2 and $Fe(NiFe)O_4$-SiO_2 catalysts, respectively. In this regard, the phenoxide species diffuse towards the metal (Ru or Ni) active phase where hydrogen is adsorbed and then dissociated to facilitate saturation of the aromatic double bonds to produce cyclohexanone. The intermediate cyclohexanone formed can directly react with the Lewis acid site again and then protonated to form cyclohexanol. Therefore, the formed cyclohexanol get attached to Lewis acid site at the OH terminal and follows deoxygenation through dehydration step due to acidic strength of the catalysts to form cyclohexene. Finally, the cyclohexene is hydrogenated into cyclohexane. The formation of a single catalyst grain surface as

University of Malaya

evidenced by atomic force microscopy analysis coupled with the surface density distributions of the catalysts; we postulated the presence of terrace and edge sites on the catalyst surface and confirmed this postulation via BET as corroborated with AFM analysis (Appendix H). It is therefore suggested that the adsorption and reaction steps that guides THF formation from furfural is due to the participation at the terrace site (Fig 4.25). Also, the formation of furfuryl alcohol is due to the participation at the edge site. However, pentane can be formed due to ring opening at the terrace site. XRD studies reveal that small percentage of Fe_3O_4 phase is present in the developed magnetic catalysts and the predominant phase is crystalline $Fe(MFe)O_4$-SiO_2. Owing to the oxophilicity nature of Fe in Fe_3O_4, it tends to attract point charges (O^{2-}, O-functionalities) from the substrate and then interacts with the Lewis acidity of $Fe(MFe)O_4$-SiO_2, which can enhance the adsorption of organic substrates on the catalyst surface.

Corroborating the above information from computational analysis point of view with the product distribution after hydro-processing reactions, the proposed reaction path way that converts Furfural and vanillin to fuel grade molecules involves gross participation of metal (M = Ni or Ru) and acid functions of the heat tuned mesoporous magnetic $Fe(MFe)O_4$-SiO_2 catalyst interacting with the oxygenates around the high electron density region of the carbonyl symmetry and the benzene ring. The reaction proceeded at 250 ^oC and 90 bar over $Fe(MFe)O_4$-SiO_2 to yield furfuryl alcohol, tetrahydrofuran, pentane, as in furfural substrate and vanillyl alcohol, guaiacol, phenol, cyclohexanone cyclohexanol, and cyclohexane as in vanillin substrate likewise. These transformations was motivated with the four potential C-O bonds in Vanillin having different bond dissociation energy (BDE) i.e. $C(sp^3)$-OAr (~262-276 kJ/mol), $C(sp^2)$-OMe, (~409-421 kJ/mol), $C(sp^2)$-OH (~466 kJ/mol) and $C(_Sp^2)$-O (~732 kJ/mol) as shown in Scheme 1. Also, $C(sp^2)$-O in Furfural motivates furfural transformation into

University of Malaya

the stated molecules (Scheme 2). Bond dissociation energy (BDE) of the feedstock substrates, tuned Fe(MFe)O_4-SiO_2 catalyst textural properties are some of the superior attributes that aid the transformation process.

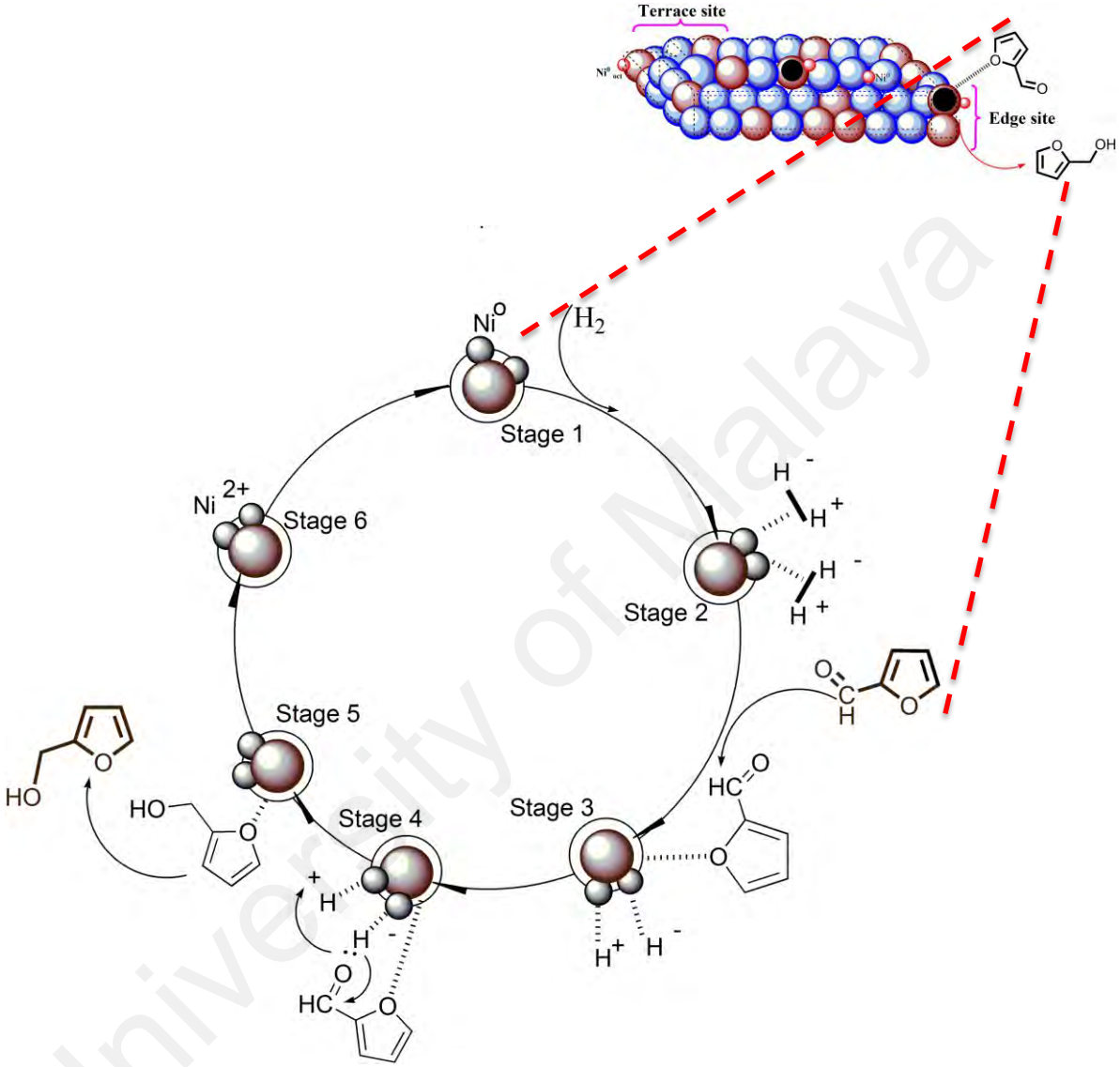

Fig 4.23: The proposed mechanism of selective hydrogenation of furfural over Fe(NiFe)O_4-SiO_2 catalyst at mild condition; 250 ^{o}C, 5 bar.

University of Malaya

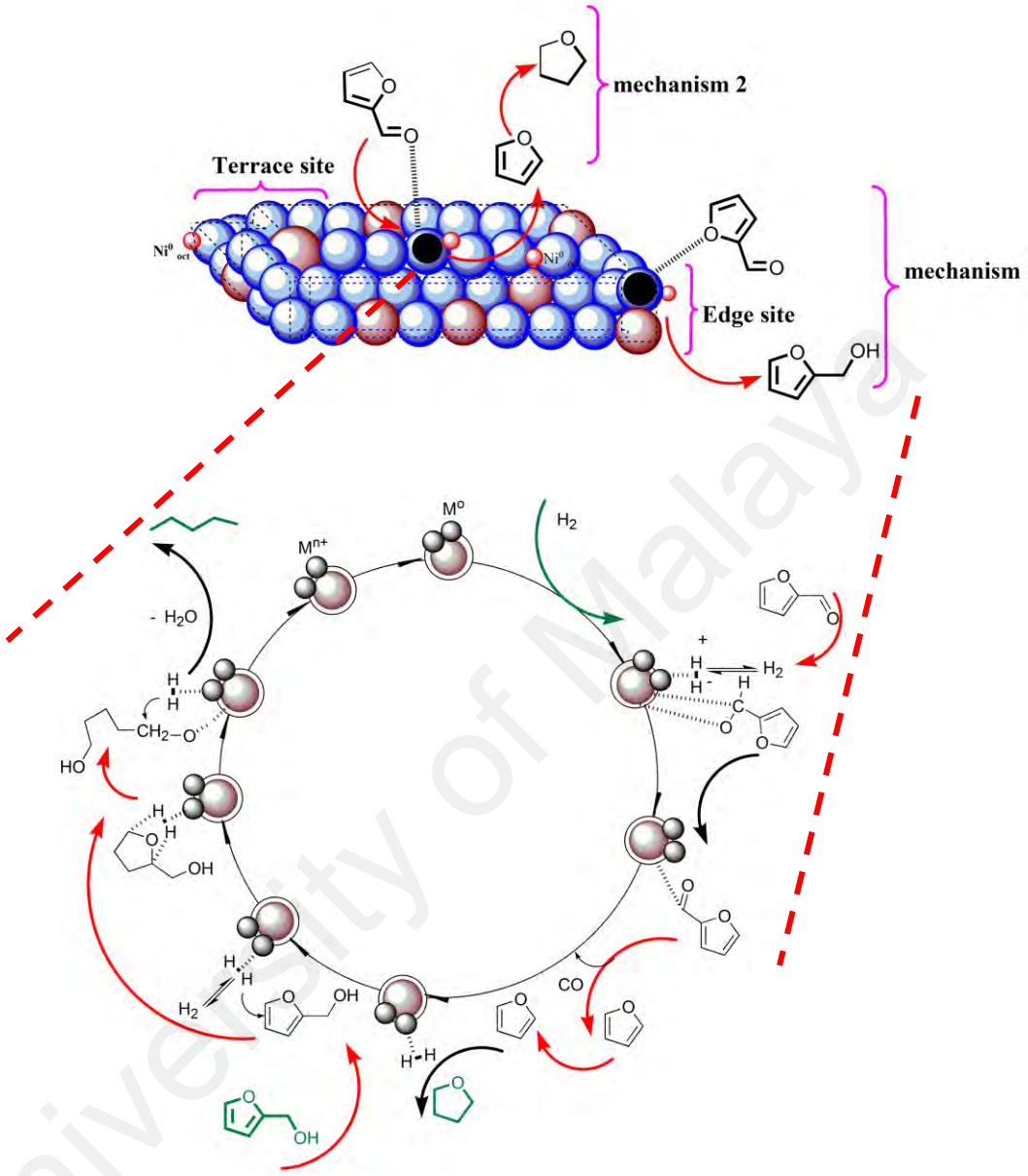

Fig. 4.24: Proposed path way for vanillin hydro-processing at 250°C, 90bar.

University of Malaya

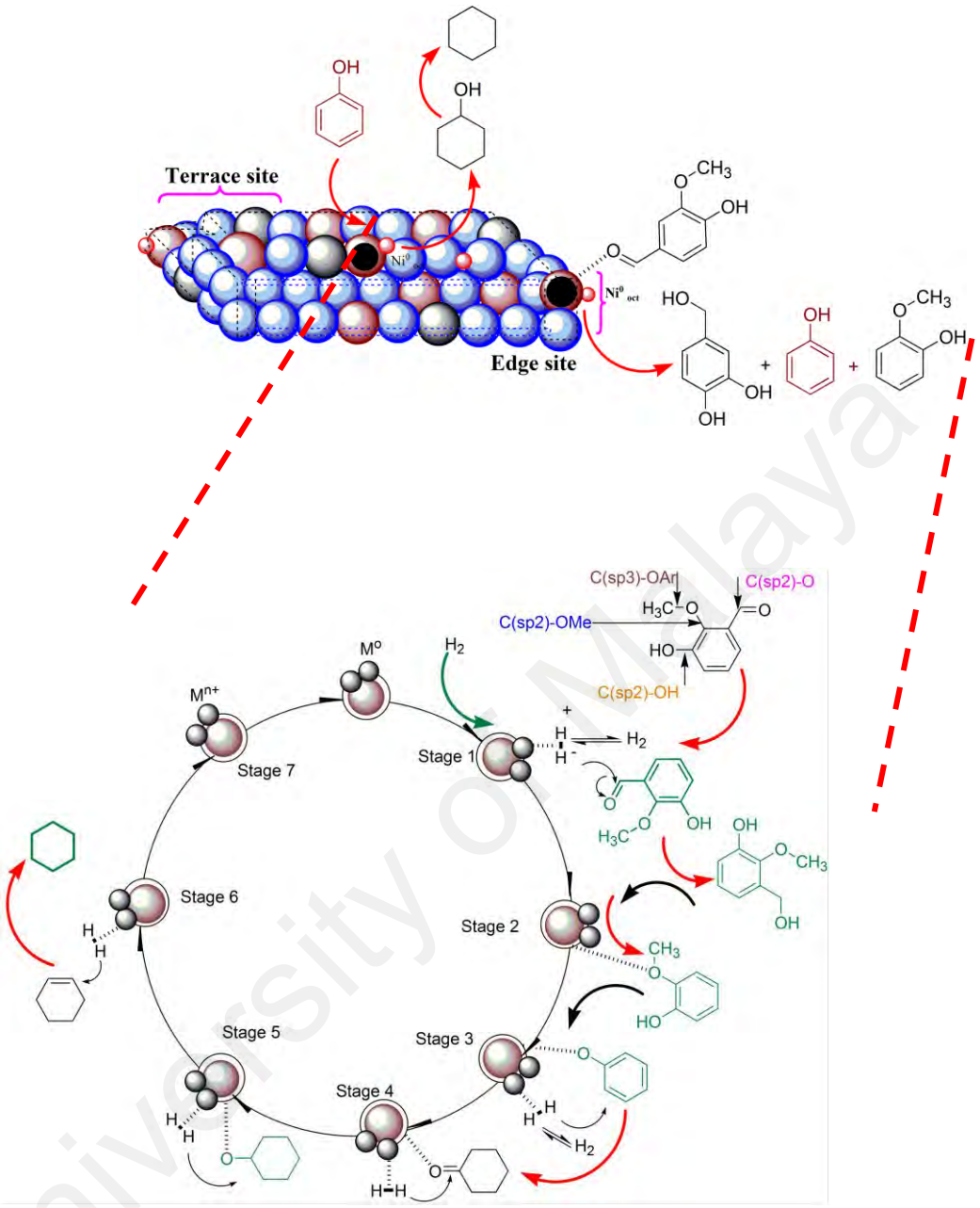

Fig. 4.25: Proposed path way for vanillin hydro-processing at 250°C, 90bar.

University of Malaya

CHAPTER 5: CONCLUSION AND FUTURE WORK

5.1 Conclusion

5.1.1 Conclusion on catalyst potentials

It is insightful to recall that this study was undertaken to solve energy problem via heterogeneous catalysis using renewable feedstock aimed to mitigate issues associated with fossil derived ones. We are glad to report in conclusion, a novel magnetic $Fe(MFe)O_4$-SiO_2 catalyst that was developed using a one-pot co-precipitation synthesis methodology at ambient condition. The catalyst development was guided by *ab initio* computation and was used as a proof of concept on hydrogenation of model compounds such as furfural and vanillin to biofuel molecules. The physical, chemical, magnetic, morphological, and structural properties of the catalyst were systematically investigated using a number of analytical techniques. The catalyst being able to target aldehyde functionality is indicative of mitigating ageing problem of biofuel. Also, the issue of photo-chemical smog formation due to the presence of aldehyde in biofuel is also solved. However, from the cyclic hydrocarbon obtained, along with other product distributions, energy density of biofuel is also enhanced. In a nutshell, environmental, energy and process issues have been solved in this study from the information obtained for the catalytic activity of $Fe(MFe)O_4$-SiO_2 nano particle catalyst. This study is limited with the fact that model compound were used to represent biofuel. Slight variation may be experienced when real biofuel is employed. One thing still remains amidst the prospective variation; the catalyst is active in targeting specific oxygenates and converting them to biofuel molecule. In addition, the following specific observations were noticed from the study:

1. The research questions on reducing aldehyde emission from lignocellulose biofuel, increasing biofuel energy density and shelf life, eliminating

University of Malaya

leaching, reduction of operational cost during hydro-processing, have been demonstrated and confirm in this study. This is evident from the catalyst being active in converting aldehydes (furfural and vanillin) into stable fuel molecules, having magnetic anisotropy, chemosorbed active component at octahedral sites and confirmed by the OSPE.

2. The developed magnetic $Fe(NiFe)O_4$-SiO_2 catalyst has excellent reducing capacity, which is highly useful for any hydro-processing via a non-hydrogen spillover route. This is due to the fact that the reducing capacity for fayalite Fe_3O_4-SiO_2 is energetically highly unlikely at hydrogenation condition of 250 ^oC in the present study.
3. The indication of Ni incorporation was evidenced from the decrease in magnetic coercivity (Hc) and magnetization (Ms). The developed magnetic $Fe(NiFe)O_4$-SiO_2 catalyst showed an appreciable magnetic Remanence via VSM analysis. This makes magnetic recoverability for the $FeNiFeO_4$-SiO_2 catalyst easy.
4. Ni metal function is responsible for the transformation of carbonyl C (sp^2)-O to C (sp^3)-O. Activity results reveal that 90 °C and 20 bar; 250 °C and 5 bar are found to be the best combinations for the hydrogenation of furfural over $Fe(NiFe)O_4$-SiO_2 catalyst.
5. A probable mechanism was proposed via a non-spillover mechanism for the hydrogenation of furfural over $Fe(NiFe)O_4$-SiO_2 catalyst. This process involves hydrogen dissociation into proton and hydride on Ni metal. The hydride ion acts as the nucleophile which increases the positive character of carbonyl C (sp^2)-O and subsequent protonation of highly electronegative (-O). These phenomena were found to take place around the spatial domain of Ni metal.

University of Malaya

6. The high selectivity of $Fe(NiFe)O_4$-SiO_2 towards Furfuryl alcohol is attributed to the unique octahedral structural positioning of nickel active metal, which creates a spatial domain that allows interaction at the carbonyl groups only.

5.1.2 Conclusion on surface atom energetics for the catalyst

On the platform of expanding the catalytic active phase surface atom structural frontiers, combined fundamental and phenomenological approach were further corroborated as an insights on new approach of tuning textural properties of template free mesoporous magnetic $Fe(MFe)O_4$-SiO_2 nanocatalyst. This is supportive to the idea of making the catalyst robust for real time application as an extension of the ordinary application to model compounds. Therefore, the surface atom modified catalyst was used in vanillin hydro-deoxygenated on $Fe(NiFe)O_4$-SiO_2 and $Fe(RuFe)O_4$-SiO_2 through primary hydrogenation to vanillyl alcohol. Likewise, Furfural is hydro-deoxygenated also through primary decarboxylation to THF, and ring opening to pentane. Some specific observations were noticed under these auspices:

1. The expressed Biot and Nusselt dimensionless numbers for $Fe(NiFe)O_4$-SiO_2 being 264 > 1 and 100.14 > 1 confirms a non-uniform heat transport during heat treatment of the catalyst. This is indicative of axial heat transport for a high aspect ratio shape whilst no radial heat transport that prevails.
2. The crystal field stabilization energy (CFSE) of M = Ni and Ru; CFSE-Ru^{3+} ~-10.7618×10^{-11} eV, CFSE-Ni^{2+}~ -7.43888×10^{-11} eV being greater than CFSE Fe^{2+} ~ -4.03578×10^{-10}eV and Fe^{3+} ~0eV is indicative that $Fe(NiFe)O_4$-SiO_2 is inverse spinel in its structure.

University of Malaya

3. The octahedral site preference energy (OSPE) for M = Ni and Ru, $OSPENi^{2+}$ > OSPE Ru^{3+} is indicative that Ni ion have more affinity than Ru for the octahedral site. This could be attributed to their ionic radii difference as well as difference in d-electron numbers. Therefore ionic radii and n-valence nature of the ion affects the OSPE.
4. The surface density (SD) of 400 ^{o}C, 500 ^{o}C, 600 ^{o}C and 700 ^{o}C for $Fe(NiFe)O_4$-SiO_2 catalyst > $Fe(RuFe)O_4$-SiO_2 catalyst. SD-Ru ~12.85, 14.69, 17.53 and 12.23 W/nm^2 > surface $Fe(NiFe)O_4$-SiO_2 catalyst recorded much higher surface density values of 146, 34.33, 155.37, and 157.74 W/nm^2 corresponding to heat treatments (HTs). The SD is dependent on ionic radii of octahedral metal, the high the radii, the lower the surface density and vice visa.
5. Delocalization of O^{2-} point charges have been confirm for polyatomic $Fe(MFe)O_4$-SiO_2 catalyst at siloxane coordination binding energy of 530.86 eV and 532.86 eV for octahedral or tetrahedral magnetite coordination.
7. Ni and Ru metal function as well as acid function based on bond dissociation energy (BDE) consideration is responsible for the transformation of C(sp^3)-OAr (~262-276kJ/mol), C(sp^2)-OMe, (~409-421kJ/mol), C(sp^2)-OH (~466kJ/mol) and C($_{S}p^2$)-O (732kJ/mol) fuel grade molecules at 250 ^{o}C, 90bar operating conditions.

5.2 Suggestion on future work

We are glad to collaborate with whoever wishes to take this study to the next level. This is because there are still more needed to be done. Some of our suggestions are seen as follows:

University of Malaya

1- There are other synthesis methods such as hydrothermal and Micro-emulsion method that could be employed to synthesis the novel $Fe(MFe)O_4$-SiO_2 catalyst material. It is plausible to carryout comparative studies in this regard using other methods different from co-precipitation.

2- The catalyst material could be tested further in hydrothermal liquefaction of micro-algae, CO_2 methanation, hydro-deoxygenation and many more other hydro-processing reactions. This confidence is derived from the unique reducibility properties of $Fe(MFe)O_4$-SiO_2 the catalyst. It could also be extended further in an integrated system of photo-bio refinery systems because it is capable of dissociating the hydrogen produced from the process.

3- In line with the fact that the catalyst is active in hydro-processing of furfural and vanillin, this study did not exhaust all the potential lignocellulose biomass oxygenates. Therefore we encourage that other oxygenate should be tested on the catalyst.

University of Malaya

REFERENCES

AB, J. M., Vetere, V., & Ruggera, J. (2009). Bimetallic PtSn Catalyst for the Selective Hydrogenation of Furfural to Furfu· 1184· 石油化工 PETROCHEMICAL TECHN0LOGY 2014 年第 43 卷 ryl Alcohol in Liquid-Phase. *Catal Commun, 10*(13), 1665-1669.

Abnisa, F., Arami-Niya, A., Daud, W. W., Sahu, J., & Noor, I. (2013). Utilization of oil palm tree residues to produce bio-oil and bio-char via pyrolysis. *Energy Conversion and Management, 76*, 1073-1082.

Agarwal, A. K. (2007). Biofuels (alcohols and biodiesel) applications as fuels for internal combustion engines. *Progress in energy and combustion science, 33*(3), 233-271.

Ahmadi, S., Zhang, X., Gong, Y., Zhu, W., & Sun, C. Q. (2016). Catalytic and Magnetic Behaviors of Excessively-Charged Ag, Cu, Pt, and Rh Atomic Clusters. *The Journal of Physical Chemistry C*.

Akash, B., Muchmore, C., & Lalvani, S. (1994). Coliquefaction of coal and newsprint-derived lignin. *Fuel processing technology, 37*(3), 203-210.

Alvira, P., Tomás-Pejó, E., Ballesteros, M., & Negro, M. (2010). Pretreatment technologies for an efficient bioethanol production process based on enzymatic hydrolysis: a review. *Bioresource technology, 101*(13), 4851-4861.

Application Furfural. (1939). *Industrial and Engineering Chemistry, News Edition, 17*(21), 691. doi: 10.1021/cen-v017n021.p691

Ardiyanti, A., Gutierrez, A., Honkela, M., Krause, A., & Heeres, H. (2011). Hydrotreatment of wood-based pyrolysis oil using zirconia-supported mono-and bimetallic (Pt, Pd, Rh) catalysts. *Applied Catalysis A: General, 407*(1), 56-66.

Asmadi, M., Kawamoto, H., & Saka, S. (2011). Pyrolysis and Secondary Reaction Mechanisms of Softwood and Hardwood Lignins at the Molecular Level. In T. Yao (Ed.), *Zero-Carbon Energy Kyoto 2010* (pp. 129-135): Springer Japan.

Ateş, F., Pütün, E., & Pütün, A. (2004). Fast pyrolysis of sesame stalk: yields and structural analysis of bio-oil. *Journal of analytical and applied pyrolysis, 71*(2), 779-790.

University of Malaya

Badger, P. (2002). Ethanol from cellulose: A general review. *Trends in new crops and new uses*, 17-21.

Baerns, M. (2013). *Basic principles in applied catalysis* (Vol. 75): Springer Science & Business Media.

Baijun, L., Lianhai, L., Bingchun, W., Tianxi, C., & Iwatani, K. (1998). Liquid phase selective hydrogenation of furfural on Raney nickel modified by impregnation of salts of heteropolyacids. *Applied Catalysis A: General, 171*(1), 117-122.

Bej, S. K. (2002). Performance evaluation of hydroprocessing catalysts A review of experimental techniques. *Energy & Fuels, 16*(3), 774-784.

Bridgwater, A., & Peacocke, G. (2000). Fast pyrolysis processes for biomass. *Renewable and Sustainable Energy Reviews, 4*(1), 1-73.

Bridgwater, A. V. (2011). Upgrading fast pyrolysis liquids. *Thermal processing of biomass: conversion into fuels, chemicals and power. Chichester: Wiley*, 157-188.

Bridgwater, A. V. (2012). Review of fast pyrolysis of biomass and product upgrading. *Biomass and bioenergy, 38*, 68-94.

Brozek, C., & Dincă, M. (2014). Cation exchange at the secondary building units of metal–organic frameworks. *Chemical Society Reviews, 43*(16), 5456-5467.

Brunner, E. (1985). Solubility of hydrogen in 10 organic solvents at 298.15, 323.15, and 373.15 K. *Journal of chemical and Engineering Data, 30*(3), 269-273.

Bykova, M., Ermakov, D. Y., Kaichev, V., Bulavchenko, O., Saraev, A., Lebedev, M. Y., & Yakovlev, V. (2012). Ni-based sol–gel catalysts as promising systems for crude bio-oil upgrading: Guaiacol hydrodeoxygenation study. *Applied Catalysis B: Environmental, 113*, 296-307.

Caruntu, D., Caruntu, G., & O'Connor, C. J. (2007). Magnetic properties of variable-sized Fe3O4 nanoparticles synthesized from non-aqueous homogeneous solutions of polyols. *Journal of Physics D: Applied Physics, 40*(19), 5801.

Carvalheiro, F., Duarte, L. C., & Gírio, F. M. (2008). Hemicellulose biorefineries: a review on biomass pretreatments.

University of Malaya

Chen, X., Li, H., Luo, H., & Qiao, M. (2002). Liquid phase hydrogenation of furfural to furfuryl alcohol over Mo-doped Co-B amorphous alloy catalysts. *Applied Catalysis A: General, 233*(1), 13-20.

Chen, Z., Zhang, W., Xu, J., & Li, P. (2015). Kinetics of xylose dehydration into furfural in acetic acid. *Chinese Journal of Chemical Engineering, 23*(4), 659-666.

Choi, Y. (2015). A manipulation of pyrolysis reaction pathways for selective bio-oil composition.

Choudhary, T., & Phillips, C. (2011). Renewable fuels via catalytic hydrodeoxygenation. *Applied Catalysis A: General, 397*(1), 1-12.

Choura, M., Belgacem, N. M., & Gandini, A. (1996). Acid-catalyzed polycondensation of furfuryl alcohol: mechanisms of chromophore formation and cross-linking. *Macromolecules, 29*(11), 3839-3850.

Chundawat, S. P., Beckham, G. T., Himmel, M. E., & Dale, B. E. (2011). Deconstruction of lignocellulosic biomass to fuels and chemicals. *Annual review of chemical and biomolecular engineering, 2*, 121-145.

Ci, S., Mao, S., Hou, Y., Cui, S., Kim, H., Ren, R., . . . Chen, J. (2015). Rational design of mesoporous NiFe-alloy-based hybrids for oxygen conversion electrocatalysis. *Journal of Materials Chemistry A, 3*(15), 7986-7993.

Climent, M. J., Corma, A., & Iborra, S. (2014). Conversion of biomass platform molecules into fuel additives and liquid hydrocarbon fuels. *Green Chemistry, 16*(2), 516-547.

Connolly, T. J., Considine, J. L., Ding, Z., Forsatz, B., Jennings, M. N., MacEwan, M. F., . . . Sutherland, K. (2010). Efficient Synthesis of 8-Oxa-3-aza-bicyclo [3.2. 1] octane Hydrochloride†. *Organic Process Research & Development, 14*(2), 459-465.

Czernik, S., & Bridgwater, A. (2004). Overview of applications of biomass fast pyrolysis oil. *Energy & Fuels, 18*(2), 590-598.

Demirbas, A. (2009). Biorefineries: current activities and future developments. *Energy Conversion and Management, 50*(11), 2782-2801.

Ding, F., Zhang, Y., Yuan, G., Wang, K., Dragutan, I., Dragutan, V., . . . Wu, J. (2015). Synthesis and Catalytic Performance of Ni/SiO2 for Hydrogenation of 2-

University of Malaya

Methylfuran to 2-Methyltetrahydrofuran. *Journal of Nanomaterials, 2015*, 6. doi: 10.1155/2015/791529

Dunlop, A. (1948). Furfural formation and behavior. *Industrial & Engineering Chemistry, 40*(2), 204-209.

Elliott, D., Beckman, D., Bridgwater, A., Diebold, J., Gevert, S., & Solantausta, Y. (1991). Developments in direct thermochemical liquefaction of biomass: 1983-1990. *Energy & Fuels, 5*(3), 399-410.

Elliott, D. C. (2001). Issues in Value-Added Products from Biomass. *Progress in Thermochemical Biomass ConVersion*, 1186-1196.

Elliott, D. C. (2007). Historical developments in hydroprocessing bio-oils. *Energy & Fuels, 21*(3), 1792-1815.

Elliott, D. C., & Hart, T. R. (2008). Catalytic hydroprocessing of chemical models for bio-oil. *Energy & Fuels, 23*(2), 631-637.

Elliott, D. C., Hart, T. R., Neuenschwander, G. G., Rotness, L. J., Olarte, M. V., Zacher, A. H., & Solantausta, Y. (2012). Catalytic hydroprocessing of fast pyrolysis bio-oil from pine sawdust. *Energy & Fuels, 26*(6), 3891-3896.

Elliott, D. C., Neuenschwander, G. G., & Hart, T. R. (2013). Hydroprocessing bio-oil and products separation for coke production. *ACS Sustainable Chemistry & Engineering, 1*(4), 389-392.

Faba, L., Díaz, E., & Ordóñez, S. (2015). Recent developments on the catalytic technologies for the transformation of biomass into biofuels: A patent survey. *Renewable and Sustainable Energy Reviews, 51*, 273-287.

Fernando, S., Adhikari, S., Chandrapal, C., & Murali, N. (2006). Biorefineries: current status, challenges, and future direction. *Energy & Fuels, 20*(4), 1727-1737.

Furimsky, E. (2000). Catalytic hydrodeoxygenation. *Applied Catalysis A: General, 199*(2), 147-190.

Gajdoš, M., Eichler, A., & Hafner, J. (2004). CO adsorption on close-packed transition and noble metal surfaces: trends from ab initio calculations. *Journal of Physics: Condensed Matter, 16*(8), 1141.

University of Malaya

Gawande, M. B., Branco, P. S., & Varma, R. S. (2013). Nano-magnetite (Fe 3 O 4) as a support for recyclable catalysts in the development of sustainable methodologies. *Chemical Society Reviews, 42*(8), 3371-3393.

Gebre, H., Fisha, K., Kindeya, T., & Gebremichal, T. (2015). SYNTHESIS OF FURFURAL FROM BAGASSE. *International Letters of Chemistry, Physics and Astronomy, 57*, 72.

Genuit, D., Afanasiev, P., & Vrinat, M. (2005). Solution syntheses of unsupported Co (Ni)–Mo–S hydrotreating catalysts. *Journal of Catalysis, 235*(2), 302-317.

Gerçel, H. F. (2002). The production and evaluation of bio-oils from the pyrolysis of sunflower-oil cake. *Biomass and bioenergy, 23*(4), 307-314.

Ghampson, I., Sepúlveda, C., Garcia, R., Frederick, B., Wheeler, M., Escalona, N., & DeSisto, W. (2012). Guaiacol transformation over unsupported molybdenum-based nitride catalysts. *Applied Catalysis A: General, 413*, 78-84.

Ghoreishi, K. B., & Yarmo, M. A. (2013). Sol-gel sulfated silica as a catalyst for glycerol acetylation with acetic acid. *J Sci Technol, 5*, 65-78.

Gírio, F., Fonseca, C., Carvalheiro, F., Duarte, L., Marques, S., & Bogel-Łukasik, R. (2010). Hemicelluloses for fuel ethanol: a review. *Bioresource Technology, 101*(13), 4775-4800.

Goudriaan, F., Naber, J., & Van den Berg, E. (2005). Conversion of biomass residues to transportation fuels with the HTU process: Retrieved 2008-01-12.

Grosvenor, A., Kobe, B., Biesinger, M., & McIntyre, N. (2004). Investigation of multiplet splitting of Fe 2p XPS spectra and bonding in iron compounds. *Surface and Interface Analysis, 36*(12), 1564-1574.

Guerrieri, D. A., Caffrey, P. J., & Rao, V. (1995). Investigation into the vehicle exhaust emissions of high percentage ethanol blends: SAE Technical Paper.

Gupta, V. G., Tuohy, M., Kubicek, C. P., Saddler, J., & Xu, F. (2013). *Bioenergy Research: Advances and Applications*: Newnes.

Halilu, A., Ali, T. H., Atta, A. Y., Sudarsanam, P., Bhargava, S. K., & Abd Hamid, S. B. (2016). Highly Selective Hydrogenation of Biomass- Derived Furfural into Furfuryl Alcohol using a Novel Magnetic Nanoparticles Catalyst. *Energy & Fuels*. doi: 10.1021/acs.energyfuels.5b02826

University of Malaya

Halma, M., Lachenal, D., Marlin, N., Deronzier, A., Brochier, M. C., & Zarubin, M. (2015). H 2 O 2 oxidation of lignin model dimers catalyzed by copper (II)–phenanthroline. *Industrial Crops and Products, 74*, 514-522.

Hammer, B., & Norskov, J. (1995). Why gold is the noblest of all the metals. *nature, 376*(6537), 238-240.

Han, S. S., Jung, H., Jung, D. H., Choi, S.-H., & Park, N. (2012). Stability of hydrogenation states of graphene and conditions for hydrogen spillover. *Physical Review B, 85*(15), 155408.

Han, T., Tsai, M., & Wei, C. (2011). Size effect on magnetic properties of hexagonal HoMnO3 nanoparticles. *Journal of Applied Physics, 109*(7), 07B517.

Heinemann, H. (1954). Hydrocarbons from cellulosic wastes. *Pet. Refiner, 33*(7), 161-163.

Hocking, M. B. (1997). Vanillin: synthetic flavoring from spent sulfite liquor. *Journal of Chemical Education, 74*(9), 1055.

Horáček, J., Homola, F., Kubičková, I., & Kubička, D. (2012). Lignin to liquids over sulfided catalysts. *Catalysis Today, 179*(1), 191-198. doi: http://dx.doi.org/10.1016/j.cattod.2011.06.031

Hronec, M., Fulajtarová, K., & Liptaj, T. (2012). Effect of catalyst and solvent on the furan ring rearrangement to cyclopentanone. *Applied Catalysis A: General, 437*, 104-111.

Hronec, M., Fulajtárova, K., & Mičušik, M. (2013). Influence of furanic polymers on selectivity of furfural rearrangement to cyclopentanone. *Applied Catalysis A: General, 468*, 426-431. doi: http://dx.doi.org/10.1016/j.apcata.2013.08.052

Huang, H.-J., Ramaswamy, S., Tschirner, U., & Ramarao, B. (2008). A review of separation technologies in current and future biorefineries. *Separation and Purification Technology, 62*(1), 1-21.

Huang, J., Liu, C., Tong, H., Li, W., & Wu, D. (2014). A density functional theory study on formation mechanism of CO, CO2 and CH4 in pyrolysis of lignin. *Computational and Theoretical Chemistry, 1045*, 1-9. doi: http://dx.doi.org/10.1016/j.comptc.2014.06.009

University of Malaya

Huang, W., Li, H., Zhu, B., Feng, Y., Wang, S., & Zhang, S. (2007). Selective hydrogenation of furfural to furfuryl alcohol over catalysts prepared via sonochemistry. *Ultrasonics sonochemistry, 14*(1), 67-74.

Ioelovich, M. (2008). Cellulose as a nanostructured polymer: a short review. *BioResources, 3*(4), 1403-1418.

Isahak, W. N. R. W., Hisham, M. W., Yarmo, M. A., & Hin, T.-y. Y. (2012). A review on bio-oil production from biomass by using pyrolysis method. *Renewable and Sustainable Energy Reviews, 16*(8), 5910-5923.

Islam, M. N., Beg, M. R. A., & Islam, M. R. (2005). Pyrolytic oil from fixed bed pyrolysis of municipal solid waste and its characterization. *Renewable Energy, 30*(3), 413-420.

Jacobson, K., Maheria, K. C., & Kumar Dalai, A. (2013). Bio-oil valorization: A review. *Renewable and Sustainable Energy Reviews, 23*, 91-106. doi: http://dx.doi.org/10.1016/j.rser.2013.02.036

Jeong, U., Teng, X., Wang, Y., Yang, H., & Xia, Y. (2007). Superparamagnetic colloids: controlled synthesis and niche applications. *Advanced Materials, 19*(1), 33-60.

Kawamoto, H., Watanabe, T., & Saka, S. (2015). Strong interactions during lignin pyrolysis in wood – A study by in situ probing of the radical chain reactions using model dimers. *Journal of Analytical and Applied Pyrolysis, 113*, 630-637. doi: http://dx.doi.org/10.1016/j.jaap.2015.04.009

Khairi, S., Hara, T., Ichikuni, N., & Shimazu, S. (2012). Highly efficient and selective hydrogenation of unsaturated carbonyl compounds using Ni–Sn alloy catalysts. *Catalysis Science & Technology, 2*(10), 2139-2145.

Kijeński, J., Winiarek, P., Paryjczak, T., Lewicki, A., & Mikołajska, A. (2002). Platinum deposited on monolayer supports in selective hydrogenation of furfural to furfuryl alcohol. *Applied Catalysis A: General, 233*(1), 171-182.

Kim, S., & Dale, B. E. (2005). Environmental aspects of ethanol derived from no-tilled corn grain: nonrenewable energy consumption and greenhouse gas emissions. *Biomass and bioenergy, 28*(5), 475-489.

Koso, S., Furikado, I., Shimao, A., Miyazawa, T., Kunimori, K., & Tomishige, K. (2009). Chemoselective hydrogenolysis of tetrahydrofurfuryl alcohol to 1, 5-pentanediol. *Chemical Communications*(15), 2035-2037.

University of Malaya

Krishnan, K. M. (2010). Biomedical nanomagnetics: a spin through possibilities in imaging, diagnostics, and therapy. *Magnetics, IEEE Transactions on, 46*(7), 2523-2558.

Laita, H., Boufi, S., & Gandini, A. (1997). The application of the Diels-Alder reaction to polymers bearing furan moieties. 1. Reactions with maleimides. *European Polymer Journal, 33*(8), 1203-1211. doi: http://dx.doi.org/10.1016/S0014-3057(97)00009-8

Lange, J. P., van der Heide, E., van Buijtenen, J., & Price, R. (2012). Furfural—a promising platform for lignocellulosic biofuels. *ChemSusChem, 5*(1), 150-166.

Lee, C. R., Yoon, J. S., Suh, Y.-W., Choi, J.-W., Ha, J.-M., Suh, D. J., & Park, Y.-K. (2012). Catalytic roles of metals and supports on hydrodeoxygenation of lignin monomer guaiacol. *Catalysis Communications, 17*, 54-58.

Lee, K., Gu, G. H., Mullen, C. A., Boateng, A. A., & Vlachos, D. G. (2015). Guaiacol hydrodeoxygenation mechanism on Pt (111): Insights from density functional theory and linear free energy relations. *ChemSusChem, 8*(2), 315-322.

Lessard, J., Morin, J.-F., Wehrung, J.-F., Magnin, D., & Chornet, E. (2010). High yield conversion of residual pentoses into furfural via zeolite catalysis and catalytic hydrogenation of furfural to 2-methylfuran. *Topics in Catalysis, 53*(15-18), 1231-1234.

Li, G., Li, N., Wang, X., Sheng, X., Li, S., Wang, A., Zhang, T. (2014). Synthesis of diesel or jet fuel range cycloalkanes with 2-methylfuran and cyclopentanone from lignocellulose. *Energy & Fuels, 28*(8), 5112-5118.

Li, H., Luo, H., Zhuang, L., Dai, W., & Qiao, M. (2003). Liquid phase hydrogenation of furfural to furfuryl alcohol over the Fe-promoted Ni-B amorphous alloy catalysts. *Journal of Molecular Catalysis A: Chemical, 203*(1), 267-275.

Lin, Y.-C., Li, C.-L., Wan, H.-P., Lee, H.-T., & Liu, C.-F. (2011). Catalytic hydrodeoxygenation of guaiacol on Rh-based and sulfided CoMo and NiMo catalysts. *Energy & Fuels, 25*(3), 890-896.

Liu, C., Wang, H., Karim, A. M., Sun, J., & Wang, Y. (2014). Catalytic fast pyrolysis of lignocellulosic biomass. *Chemical Society Reviews, 43*(22), 7594-7623. doi: 10.1039/C3CS60414D.

Liu, C., & Wilson, A. K. (2015). Cleavage of the βO4 linkage of lignin using group 8 pincer complexes: A DFT study. *Journal of Molecular Catalysis A: Chemical, 399*, 33-41. doi: http://dx.doi.org/10.1016/j.molcata.2015.01.013

University of Malaya

Lomascolo, A., Stentelaire, C., Asther, M., & Lesage-Meessen, L. (1999). Basidiomycetes as new biotechnological tools to generate natural aromatic flavours for the food industry. *Trends in Biotechnology, 17*(7), 282-289.

Lowrie, W. (1990). Identification of ferromagnetic minerals in a rock by coercivity and unblocking temperature properties. *Geophysical Research Letters, 17*(2), 159-162.

Lu, J., & Heyden, A. (2015). Theoretical investigation of the reaction mechanism of the hydrodeoxygenation of guaiacol over a Ru (0001) model surface. *Journal of Catalysis, 321*, 39-50.

Lykhach, Y., Staudt, T., Vorokhta, M., Skála, T., Johánek, V., Prince, K. C., . . . Libuda, J. (2012). Hydrogen spillover monitored by resonant photoemission spectroscopy. *Journal of Catalysis, 285*(1), 6-9.

Maginn, E. J. (2009). From discovery to data: What must happen for molecular simulation to become a mainstream chemical engineering tool. *AIChE Journal, 55*(6), 1304-1310.

Mäki-Arvela, P., Hajek, J., Salmi, T., & Murzin, D. Y. (2005). Chemoselective hydrogenation of carbonyl compounds over heterogeneous catalysts. *Applied Catalysis A: General, 292*, 1-49.

Maldas, D., & Shiraishi, N. (1997). Liquefaction of biomass in the presence of phenol and H 2 O using alkalies and salts as the catalyst. *Biomass and bioenergy, 12*(4), 273-279.

Mamman, A. S., Lee, J. M., Kim, Y. C., Hwang, I. T., Park, N. J., Hwang, Y. K., . . . Hwang, J. S. (2008). Furfural: Hemicellulose/xylosederived biochemical. *Biofuels, Bioproducts and Biorefining, 2*(5), 438-454.

Martinez, A. G., Alvarez, R. M., Aguirre, J. A., & Subramanian, L. R. (1986). Mechanism of hydrogenolysis. Part 1. Catalytic hydrogenation of vinyl and aryltrifluoromethanesulphonates. *Journal of the Chemical Society, Perkin Transactions 1*(0), 1595-1598. doi: 10.1039/P19860001595.

Maugé, F., Vallet, A., Bachelier, J., Duchet, J. C., & Lavalley, J. C. (1996). Preparation, Characterization, and Activity of Sulfided Catalysts Promoted by Co(CO)3NO Thermodecomposition. *Journal of Catalysis, 162*(1), 88-95. doi: http://dx.doi.org/10.1006/jcat.1996.0262.

Mavrikakis, M., Hammer, B., & Nørskov, J. K. (1998). Effect of strain on the reactivity of metal surfaces. *Physical Review Letters, 81*(13), 2819.

University of Malaya

Miao, X., Wu, Q., & Yang, C. (2004). Fast pyrolysis of microalgae to produce renewable fuels. *Journal of analytical and applied pyrolysis, 71*(2), 855-863.

Mohammadzadeh, J. S. S., & Zamaniyan, A. (2002). Catalyst Shape as a Design Parameter—Optimum Shape for Methane-Steam Reforming Catalyst. *Chemical Engineering Research and Design, 80*(4), 383-391. doi: http://dx.doi.org/10.1205/026387602317446425.

Mohan, D., Pittman, C. U., & Steele, P. H. (2006). Pyrolysis of wood/biomass for bio-oil: a critical review. *Energy & Fuels, 20*(3), 848-889.

Monti, M., Santos, B., Mascaraque, A., de la Fuente, O. R., Niño, M. A., Menteş, T. O., . . . de La Figuera, J. (2012). Magnetism in nanometer-thick magnetite. *Physical Review B, 85*(2), 020404.

Moon, R. J., Martini, A., Nairn, J., Simonsen, J., & Youngblood, J. (2011). Cellulose nanomaterials review: structure, properties and nanocomposites. *Chemical Society Reviews, 40*(7), 3941-3994.

Mortensen, P. M., Grunwaldt, J.-D., Jensen, P. A., Knudsen, K., & Jensen, A. D. (2011). A review of catalytic upgrading of bio-oil to engine fuels. *Applied Catalysis A: General, 407*(1), 1-19.

Mortensen, P. M., Grunwaldt, J. D., Jensen, P. A., Knudsen, K. G., & Jensen, A. D. (2011). A review of catalytic upgrading of bio-oil to engine fuels. *Applied Catalysis A: General, 407*(1-2), 1-19. doi: 10.1016/j.apcata.2011.08.046

Nagaraja, B., Kumar, V. S., Shasikala, V., Padmasri, A., Sreedhar, B., Raju, B. D., & Rao, K. R. (2003). A highly efficient Cu/MgO catalyst for vapour phase hydrogenation of furfural to furfuryl alcohol. *Catalysis communications, 4*(6), 287-293.

Nakagawa, Y., Takada, K., Tamura, M., & Tomishige, K. (2014). Total hydrogenation of furfural and 5-hydroxymethylfurfural over supported Pd–Ir Alloy catalyst. *ACS Catalysis, 4*(8), 2718-2726.

Nakagawa, Y., Tamura, M., & Tomishige, K. (2013). Catalytic reduction of biomass-derived furanic compounds with hydrogen. *ACS Catalysis, 3*(12), 2655-2668.

Nakagawa, Y., & Tomishige, K. (2010). Total hydrogenation of furan derivatives over silica-supported Ni–Pd alloy catalyst. *Catalysis communications, 12*(3), 154-156.

University of Malaya

Nilsson, A., Pettersson, L., Hammer, B., Bligaard, T., Christensen, C. H., & Nørskov, J. K. (2005). The electronic structure effect in heterogeneous catalysis. *Catalysis letters, 100*(3-4), 111-114.

Noh, S.-h., Na, W., Jang, J.-t., Lee, J.-H., Lee, E. J., Moon, S. H., Cheon, J. (2012). Nanoscale magnetism control via surface and exchange anisotropy for optimized ferrimagnetic hysteresis. *Nano letters, 12*(7), 3716-3721.

Norskov, J. K., Bligaard, T., Rossmeisl, J., & Christensen, C. H. (2009). Towards the computational design of solid catalysts. *Nat Chem, 1*(1), 37-46.

Nørskov, J. K., Bligaard, T., Rossmeisl, J., & Christensen, C. H. (2009). Towards the computational design of solid catalysts. *Nature chemistry, 1*(1), 37-46.

Oasmaa, A., Van De Beld, B., Saari, P., Elliott, D. C., & Solantausta, Y. (2015). Norms, Standards, and Legislation for Fast Pyrolysis Bio-oils from Lignocellulosic Biomass. *Energy & Fuels, 29*(4), 2471-2484.

Osada, M., Sato, T., Watanabe, M., Adschiri, T., & Arai, K. (2004). Low-Temperature Catalytic Gasification of Lignin and Cellulose with a Ruthenium Catalyst in Supercritical Water. *Energy & Fuels, 18*(2), 327-333. doi: 10.1021/ef034026y

Pang, S. H., & Medlin, J. W. (2011). Adsorption and reaction of furfural and furfuryl alcohol on Pd (111): Unique reaction pathways for multifunctional reagents. *ACS Catalysis, 1*(10), 1272-1283.

Patil, P. T., Armbruster, U., Richter, M., & Martin, A. (2011). Heterogeneously catalyzed hydroprocessing of organosolv lignin in sub-and supercritical solvents. *Energy & Fuels, 25*(10), 4713-4722.

Patil, S. K., & Lund, C. R. (2011). Formation and growth of humins via aldol addition and condensation during acid-catalyzed conversion of 5-hydroxymethylfurfural. *Energy & Fuels, 25*(10), 4745-4755.

Patwardhan, P. R., Brown, R. C., & Shanks, B. H. (2011). Understanding the fast pyrolysis of lignin. *ChemSusChem, 4*(11), 1629-1636.

Peddis, D., Mansilla, M., Mørup, S., Cannas, C., Musinu, A., Piccaluga, G., . . . Fiorani, D. (2008). Spin-canting and magnetic anisotropy in ultrasmall $CoFe_2O_4$ nanoparticles. *The Journal of Physical Chemistry B, 112*(29), 8507-8513.

Pereira, C., Pereira, A. M., Fernandes, C., Rocha, M., Mendes, R., Fernández-García, M. P., . . . Araújo, . o. P. (2012). Superparamagnetic MFe2O4 (M= Fe, Co, Mn)

University of Malaya

nanoparticles: tuning the particle size and magnetic properties through a novel one-step coprecipitation route. *Chemistry of Materials, 24*(8), 1496-1504.

Peterson, A. A., Vogel, F., Lachance, R. P., Fröling, M., Antal Jr, M. J., & Tester, J. W. (2008). Thermochemical biofuel production in hydrothermal media: a review of sub-and supercritical water technologies. *Energy & Environmental Science, 1*(1), 32-65.

Petropavlovskii, G., & Kotel'nikova, N. (1979). Microcrystalline cellulose (review). *Khimiia drevesiny*.

Polshettiwar, V., Luque, R., Fihri, A., Zhu, H., Bouhrara, M., & Basset, J.-M. (2011). Magnetically recoverable nanocatalysts. *Chemical reviews, 111*(5), 3036-3075.

Ponec, V. (1997). On the role of promoters in hydrogenations on metals; α, β-unsaturated aldehydes and ketones. *Applied Catalysis A: General, 149*(1), 27-48.

Priefert, H., Rabenhorst, J., & Steinbüchel, A. (2001). Biotechnological production of vanillin. *Applied Microbiology and Biotechnology, 56*(3-4), 296-314.

Prins, R. (2012). Hydrogen spillover. Facts and fiction. *Chemical Reviews, 112*(5), 2714-2738.

Purwanto, Deshpande, R. M., Chaudhari, R. V., & Delmas, H. (1996). Solubility of Hydrogen, Carbon Monoxide, and 1-Octene in Various Solvents and Solvent Mixtures. *Journal of Chemical & Engineering Data, 41*(6), 1414-1417. doi: 10.1021/je960024e

Putla, S., Amin, M. H., Reddy, B. M., Nafady, A., Al Farhan, K. A., & Bhargava, S. K. (2015). MnOx Nanoparticle-Dispersed CeO_2 Nanocubes: A Remarkable Heteronanostructured System with Unusual Structural Characteristics and Superior Catalytic Performance. *ACS applied materials & interfaces, 7*(30), 16525-16535. doi: 10.1021/acsami.5b03988.

Qin, F., Cui, H., Yi, W., & Wang, C. (2014). Upgrading the Water-Soluble Fraction of Bio-oil by Simultaneous Esterification and Acetalation with Online Extraction. *Energy & Fuels, 28*(4), 2544-2553.

Rajagopal, D., & Zilberman, D. (2007). *Review of environmental, economic and policy aspects of biofuels* (Vol. 4341): World Bank Publications.

University of Malaya

Ramsurn, H., & Gupta, R. B. (2012). Production of biocrude from biomass by acidic subcritical water followed by alkaline supercritical water two-step liquefaction. *Energy & Fuels, 26*(4), 2365-2375.

Resende, F. L. P., Fraley, S. A., Berger, M. J., & Savage, P. E. (2008). Noncatalytic Gasification of Lignin in Supercritical Water. *Energy & Fuels, 22*(2), 1328-1334. doi: 10.1021/ef700574k.

Ringan, N. S., & Grayson, L. (1994). Molecular Modelling in the Undergraduate Chemistry Curriculum: The Use of beta-Lactams as a Case Study. *Journal of Chemical Education, 71*(10), 856. doi: 10.1021/ed071p856.

Romano, R. T., & Zhang, R. (2008). Co-digestion of onion juice and wastewater sludge using an anaerobic mixed biofilm reactor. *Bioresource technology, 99*(3), 631-637.

Ruiz, P., Frederick, B., De Sisto, W., Austin, R., Radovic, L., Leiva, K., . . . Wheeler, M. (2012). Guaiacol hydrodeoxygenation on MoS 2 catalysts: influence of activated carbon supports. *Catalysis Communications, 27*, 44-48.

Runnebaum, R. C., Nimmanwudipong, T., Block, D. E., & Gates, B. C. (2011). Catalytic conversion of anisole: evidence of oxygen removal in reactions with hydrogen. *Catalysis letters, 141*(6), 817-820.

Saha, B. C. (2003). Hemicellulose bioconversion. *Journal of Industrial Microbiology and Biotechnology, 30*(5), 279-291.

Sakakibara, A., & Nakayama, N. (1962). Hydrolysis of lignin with dioxane and water. *J. Japan Wood Res. Soc, 8*, 153-156.

Şensöz, S., Angın, D., & Yorgun, S. (2000). Influence of particle size on the pyrolysis of rapeseed (Brassica napus L.): fuel properties of bio-oil. *Biomass and bioenergy, 19*(4), 271-279.

Şensöz, S., Demiral, İ., & Gerçel, H. F. (2006). Olive bagasse (Olea europea L.) pyrolysis. *Bioresource Technology, 97*(3), 429-436.

Seo, G., & Chon, H. (1981). Hydrogenation of furfural over copper-containing catalysts. *Journal of Catalysis, 67*(2), 424-429.

Serrano-Ruiz, J. C., & Dumesic, J. A. (2011). Catalytic routes for the conversion of biomass into liquid hydrocarbon transportation fuels. *Energy & Environmental Science, 4*(1), 83-99.

University of Malaya

Sharma, R. K., Wooten, J. B., Baliga, V. L., Lin, X., Chan, W. G., & Hajaligol, M. R. (2004). Characterization of chars from pyrolysis of lignin. *Fuel, 83*(11), 1469-1482.

Sharma, R. V., Das, U., Sammynaiken, R., & Dalai, A. K. (2013). Liquid phase chemo-selective catalytic hydrogenation of furfural to furfuryl alcohol. *Applied Catalysis A: General, 454*, 127-136.

Shuttleworth, P., Parker, H., Hunt, A., Budarin, V., Matharu, A., & Clark, J. (2014). Applications of nanoparticles in biomass conversion to chemicals and fuels. *Green Chemistry, 16*(2), 573-584.

Sipilä, K., Kuoppala, E., Fagernäs, L., & Oasmaa, A. (1998). Characterization of biomass-based flash pyrolysis oils. *Biomass and bioenergy, 14*(2), 103-113.

Sitthisa, S., & Resasco, D. E. (2011). Hydrodeoxygenation of furfural over supported metal catalysts: a comparative study of Cu, Pd and Ni. *Catalysis letters, 141*(6), 784-791.

Sitthisa, S., Sooknoi, T., Ma, Y., Balbuena, P. B., & Resasco, D. E. (2011). Kinetics and mechanism of hydrogenation of furfural on Cu/SiO_2 catalysts. *Journal of Catalysis, 277*(1), 1-13.

Staš, M., Chudoba, J., Kubička, D., & Pospíšil, M. (2015). Chemical Characterization of Pyrolysis Bio-oil: Application of Orbitrap Mass Spectrometry. *Energy & Fuels, 29*(5), 3233-3240. doi: 10.1021/acs.energyfuels.5b00407.

Stöcker, M. (2008). Biofuels and biomass-to-liquid fuels in the biorefinery: Catalytic conversion of lignocellulosic biomass using porous materials. *Angewandte Chemie International Edition, 47*(48), 9200-9211.

Sun, J., & Liu, H. (2011). Selective hydrogenolysis of biomass-derived xylitol to ethylene glycol and propylene glycol on supported Ru catalysts. *Green Chemistry, 13*(1), 135-142.

Sun, Y., & Cheng, J. (2002). Hydrolysis of lignocellulosic materials for ethanol production: a review. *Bioresource Technology, 83*(1), 1-11.

Tamura, M., Shimizu, K.-i., & Satsuma, A. (2012). Comprehensive IR study on acid/base properties of metal oxides. *Applied Catalysis A: General, 433*, 135-145.

University of Malaya

Tan, S. S., MacFarlane, D. R., Upfal, J., Edye, L. A., Doherty, W. O., Patti, A. F., . Scott, J. L. (2009). Extraction of lignin from lignocellulose at atmospheric pressure using alkylbenzenesulfonate ionic liquid. *Green Chemistry, 11*(3), 339-345.

Tang, X., Zeng, X., Li, Z., Hu, L., Sun, Y., Liu, S., . . . Lin, L. (2014). Production of γ-valerolactone from lignocellulosic biomass for sustainable fuels and chemicals supply. *Renewable and Sustainable Energy Reviews, 40*, 608-620.

Taylor, A. B., Moran, D. P., Bell, A. J., Hodgson, N. G., Myburgh, I. S., & Botha, J. J. (1996). Gasoline/alcohol blends: exhaust emissions, performance and burn-rate in a multi-valve production engine: SAE Technical Paper.

Tike, M. A., & Mahajani, V. V. (2007). Kinetics of liquid-phase hydrogenation of furfuryl alcohol to tetrahydrofurfuryl alcohol over a Ru/TiO2 catalyst. *Industrial & engineering chemistry research, 46*(10), 3275-3282.

Tsai, W. T., Lee, M. K., & Chang, Y. M. (2007). Fast pyrolysis of rice husk: Product yields and compositions. *Bioresource Technology, 98*(1), 22-28. doi: http://dx.doi.org/10.1016/j.biortech.2005.12.005.

Tucker, M. H., Crisci, A. J., Wigington, B. N., Phadke, N., Alamillo, R., Zhang, J., . . . Dumesic, J. A. (2012). Acid-functionalized SBA-15-type periodic mesoporous organosilicas and their use in the continuous production of 5-hydroxymethylfurfural. *ACS Catalysis, 2*(9), 1865-1876.

van Dam, J. E., de Klerk-Engels, B., Struik, P. C., & Rabbinge, R. (2005). Securing renewable resource supplies for changing market demands in a bio-based economy. *Industrial crops and products, 21*(1), 129-144.

Venderbosch, R., & Heeres, H. (2011). *Pyrolysis oil stabilisation by catalytic hydrotreatment*: INTECH Open Access Publisher.

Venderbosch, R. H., Ardiyanti, A. R., Wildschut, J., Oasmaa, A., & Heeres, H. J. (2010). Stabilization of biomass-derived pyrolysis oils. *Journal of Chemical Technology & Biotechnology, 85*(5), 674-686. doi: 10.1002/jctb.2354.

Vertès, A. A., Inui, M., & Yukawa, H. (2008). Technological options for biological fuel ethanol. *Journal of molecular microbiology and biotechnology, 15*(1), 16-30.

Vinueza, N. R., Kim, E. S., Gallardo, V. A., Mosier, N. S., Abu-Omar, M. M., Carpita, N. C., & Kenttämaa, H. I. (2015). Tandem mass spectrometric characterization of the conversion of xylose to furfural. *Biomass and Bioenergy, 74*, 1-5.

University of Malaya

Vorotnikov, V., Mpourmpakis, G., & Vlachos, D. G. (2012). DFT study of furfural conversion to furan, furfuryl alcohol, and 2-methylfuran on Pd (111). *ACS Catalysis, 2*(12), 2496-2504.

Walton, N. J., Mayer, M. J., & Narbad, A. (2003). Vanillin. *Phytochemistry, 63*(5), 505-515.

Wu, J., Shen, Y., Liu, C., Wang, H., Geng, C., & Zhang, Z. (2005). Vapor phase hydrogenation of furfural to furfuryl alcohol over environmentally friendly Cu–Ca/SiO_2 catalyst. *Catalysis communications, 6*(9), 633-637.

Xiu, S., & Shahbazi, A. (2012). Bio-oil production and upgrading research: A review. *Renewable and Sustainable Energy Reviews, 16*(7), 4406-4414.

Yan, K., Liao, J., Wu, X., & Xie, X. (2013). A noble-metal free Cu-catalyst derived from hydrotalcite for highly efficient hydrogenation of biomass-derived furfural and levulinic acid. *RSC Advances, 3*(12), 3853-3856.

Yan, K., Wu, G., Lafleur, T., & Jarvis, C. (2014). Production, properties and catalytic hydrogenation of furfural to fuel additives and value-added chemicals. *Renewable and Sustainable Energy Reviews, 38*, 663-676.

Ying Hao, X.-., Zhou, W., Wang, J.-W., Zhang, Y.-Q., & Liu, S. (2005). A novel catalyst for the selective hydrogenation of furfural to furfuryl alcohol. *Chemistry letters, 34*(7), 1000-1001.

Yu, W., Porosoff, M. D., & Chen, J. G. (2012). Review of Pt-based bimetallic catalysis: from model surfaces to supported catalysts. *Chemical reviews, 112*(11), 5780-5817.

Zacher, A. H., Olarte, M. V., Santosa, D. M., Elliott, D. C., & Jones, S. B. (2014). A review and perspective of recent bio-oil hydrotreating research. *Green Chemistry, 16*(2), 491-515.

Zeitsch, K. J. (2000). *The chemistry and technology of furfural and its many by-products* (Vol. 13): Elsevier.

Zhang, B., von Keitz, M., & Valentas, K. (2008). Thermal effects on hydrothermal biomass liquefaction *Biotechnology for Fuels and Chemicals* (pp. 511-518): Springer.

University of Malaya

Zhang, Q., Chang, J., Wang, T., & Xu, Y. (2007). Review of biomass pyrolysis oil properties and upgrading research. *Energy Conversion and Management, 48*(1), 87-92.

Zhao, H., Li, D., Bui, P., & Oyama, S. (2011). Hydrodeoxygenation of guaiacol as model compound for pyrolysis oil on transition metal phosphide hydroprocessing catalysts. *Applied Catalysis A: General, 391*(1), 305-310.

Zhu, H., Chen, Y., Qin, T., Wang, L., Tang, Y., Sun, Y., & Wan, P. (2014). Lignin depolymerization via an integrated approach of anode oxidation and electro-generated H 2 O 2 oxidation. *RSC Advances, 4*(12), 6232-6238.

University of Malaya

APPENDICES

Appendix A:

A.1: Magnetic recoverability of $Fe(MFe)O_4$-SiO_2 catalyst

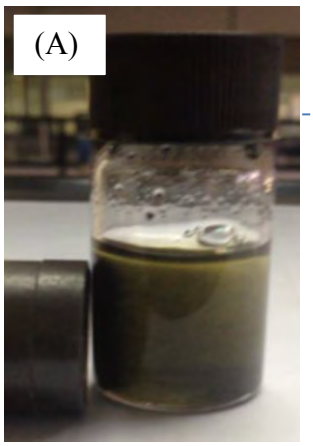

Dispersed $Fe(MFe)O_4$-SiO_2 catalyst in reaction product around a magnet.

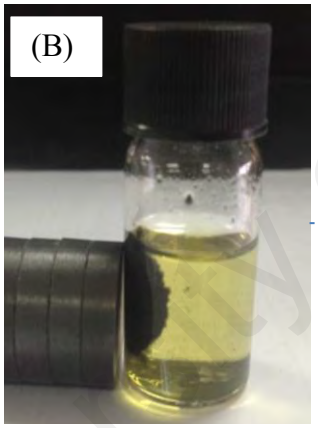

Magnetic $Fe(MFe)O_4$-SiO_2 attracted to a magnet during magnetic recoverability

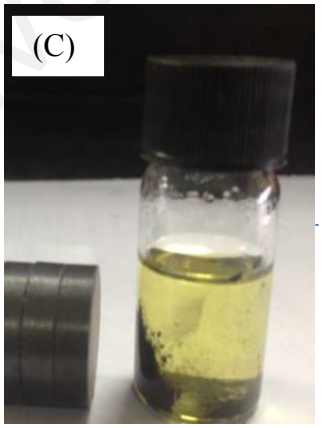

Magnetic $Fe(MFe)O_4$-SiO_2 falling back into the reaction product after removing the magnet.

University of Malaya

Table A.1: Crystal field data for transition metal ions in the $Fe(NiFe)O_4$-SiO_2 catalyst.

$Fe(NiFe)O_4$-SiO_2				Octahedral Site	Tetrahedral Site	OSPE (eV)
No of d-electrons	Ion	Configuration	Dq (cm^{-1})	**CFSE (eV)**	**CFSE (eV)**	
5	Fe^{3+}	$t_{2g}^3eg^2$	`240	0 Δo	0 Δo	0 Δo
6	Fe^{2+}	$t_{2g}^4eg^2$	718	-4.03578×10^{-10}	-2.3766×10^{-11}	-1.1871×10^{-11}
8	Ni^{2+}	$t_{2g}^6eg^2$	500	-7.4388×10^{-11}	-2.2041×10^{-11}	-5.2347×10^{-11}

Table A.2: Crystal field data for transition metal ions in the $Fe(RuFe)O_4$-SiO_2 catalyst.

$Fe(RuFe)O_4$-SiO_2				Octahedral Site	Tetrahedral Site	OSPE (eV)
No of d-electrons	Ion	Configuration	Dq (cm^{-1})	**CFSE (eV)**	**CFSE (eV)**	
5	Fe^{3+}	$t_{2g}^3eg^2$	190	0 Δo	0 Δo	0 Δo
6	Fe^{2+}	$t_{2g}^4eg^2$	715	-3.5470×10^{-10}	-2.3647×10^{-11}	-1.1823×10^{-11}
7	Ru^{3+}	$t_{2g}^5eg^2$	495	-10.7618×10^{-11}	-3.2736×10^{-11}	-7.4882×10^{-11}

University of Malaya

Appendix B: Thermal property of $Fe(MFe)O_4$-SiO_2 catalyst

Table B.1. TGA-DTG of $Fe(NiFe)O_4$-SiO_2 catalyst

Parameter	$FeNiFeO_4$-SiO_2				
	Starting material	1st stage	2nd stage	3rd stage	Residue
% (wt)	100% (8.1800mg)	3.5886 % -0.2935 mg	1.0193 % -0.00833 mg	1.2426 % -0.1016mg	94.1442 % (7.7010mg)
Temp ^oC	RT	50-100	370-400	550	550
Time (min)	0	3-7	35	52	52

University of Malaya

Table B.2. TGA-DTG of $Fe(RuFe)O_4$-SiO_2 catalyst

Parameter	$FeRuFeO_4$-SiO_2					
	SM	1st stage	2nd stage	3rd stage	4th stage	Residue
% (wt)	100 %	1.5465 %	5.2757 %	1.9617 %	0.3060 %	91.5159 %
	(6.5300 mg)	-0.1010 mg	-0.3445 mg	-0.1281 mg	-0.01998 mg	(5.9760 mg)
Temp °C	RT	50-100	370-400	550	620	620
Time (min)	0	2.5	16.5	32	60	60

SM: starting material, RT: room temperature

University of Malaya

Appendix C: Magnetic properties of $Fe(MFe)O_4$-SiO_2 catalyst

Table C.1. Super paramagnetic property of $Fe(MFe)O_4$-SiO_2

VSM Analysis				
Material	Coercivity (Hci) G	Remanence (Mr) emu/g	Magnetization (Ms) emu/g	Ni loading (wt %)
$Fe(NiFe)O_4$-SiO_2	5.8136	0.3949	33.2510	0.51
	6.6810	0.4575	37.7980	0.41
	6.9910	0.5043	40.1270	0.32
	7.8070	0.5386	43.0690	0.13
	7.8124	0.4558	39.8340	0.06
	27.323	1.9097	45.6110	0
NiO	40.216	0.0112	0.1182	100
Material	Coercivity (Hci) G	Remanence (Mr) emu/g	Magnetization (Ms) emu/g	Ru loading (wt %)
$Fe(RuFe)O_4$-SiO_2	13.353	1.1223	40.648	~0.51

M = Ni or Ru

University of Malaya

Table C.2. Effect of temperature on magnetic parameter of $Fe(NiFe)O_4$-SiO_2

Mass (mg)	$Fe(NiFe)O_4$-SiO_2				
	Temp	size	Ms	Mr	Hc
~14.28	400	12.50	32.593	0.50538	7.5123
~14.28	500	14.20	38.586	0.56678	6.8898
~14.28	600	18.90	32.97	0.37908	6.7886
~14.28	700	13.40	35.41	0.51227	7.1202

Table C.3. Effect of temperature on magnetic parameter of $Fe(RuFe)O_4$-SiO_2

Mass (mg)	$FeRuFeO_4$-SiO_2				
	Temp	size	Ms	Mr	Hc
~14.28	400	12.50	40.712	0.8534	7.4116
~14.28	500	14.32	44.527	0.9004	8.4148
~14.28	600	19.80	44.990	0.7234	10.252
~14.28	700	13.55	43.511	0.8896	9.8581

University of Malaya

Appendix D: Chemical properties of catalyst

Table D.1. FTIR and Raman

	FT-IR				Raman			
	Tetrahedral Site		Octahedral Site		Tetrahedral Site		Octahedral Site	
S/N	WN(cm^{-1})	A	WN(cm^{-1})	A	WN(cm^{-1})	A	WN (cm^{-1})	A
1	-	-	460	Ni-O	240	- Fe^{3+}-	500	Ni-O
2	567	O-Fe-O	-	-	800		598	Ni-O
3	648	O-Fe-O	-	-	915	$Si-O^-$	-	-
4	-	-	-	-	1070	$Si(-O-)_2$	-	-
5	1084	Si-O-Fe	-	-	1310	Si-O-Fe	-	-

WN: wavenumber, A: Assignment

University of Malaya

Table D.2. Temperature programmed reduction (TPR)

Catalytic material	Total H_2 consumed (µmol/g)	Ramp (^oC/min)	Gas flow (ml/min)	Stages/reduction T ^oC		
				1	2	3
$FeNiFeO_4$-SiO_2	4972.	10	10	408	448	611
$FeRuFeO_4$-SiO_2	21491	10	10	459	-	655
Fe_3O_4	2452	10	10	0	0	648
SiO_2	0.0000	10	10	no reduction from 30 to 700^oC		

University of Malaya

Table D.3. X-ray Fluorescence (XRF)

	Composition			Total
ID	Ni	SiO_2	Fe_3O_4	
$FeNiFeO_4$-SiO_2	0.41	38.7	58.6	100
$FeNiFeO_4$-SiO_2	0.32	40.2	55.4	100
$FeNiFeO_4$-SiO_2	0.51	38.0	57.0	100
$FeNiFeO_4$-SiO_2	0.13	39.2	55.6	100
$FeNiFeO_4$-SiO_2	0.06	39.4	55.3	100
Fe_3O_4-SiO_2	0	37.5	58.4	100
Fe_3O_4	0	0	100	100

Composition				
x = Ni %	y = Si %	z = Fe%	n = O%	**Total**
0.51	18.11	40.44	40.94	100
Catalyst formula: $Fe_xO_ySi_zNi_n$				

S/N	**Composition**			
	Ru	SiO_2	Fe_3O_4	**Total**
$FeRuFeO_4$-SiO_2	0.51	37.7	58.6	100

University of Malaya

Appendix E: Bet Analysis

E.1: BET analysis on $Fe(NiFe)O_4$-SiO_2

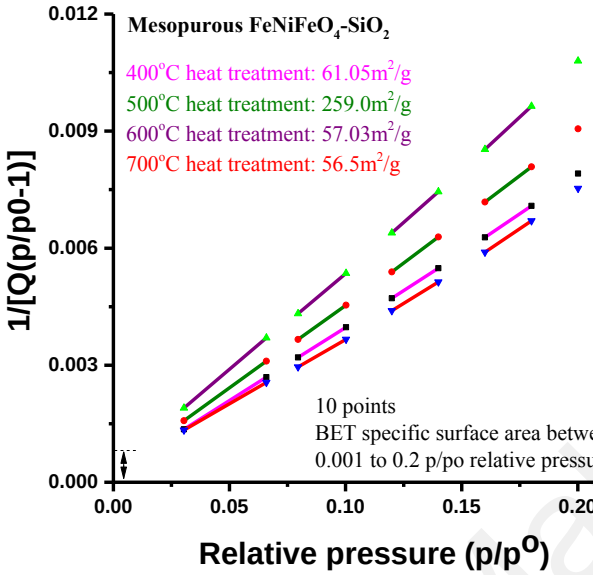

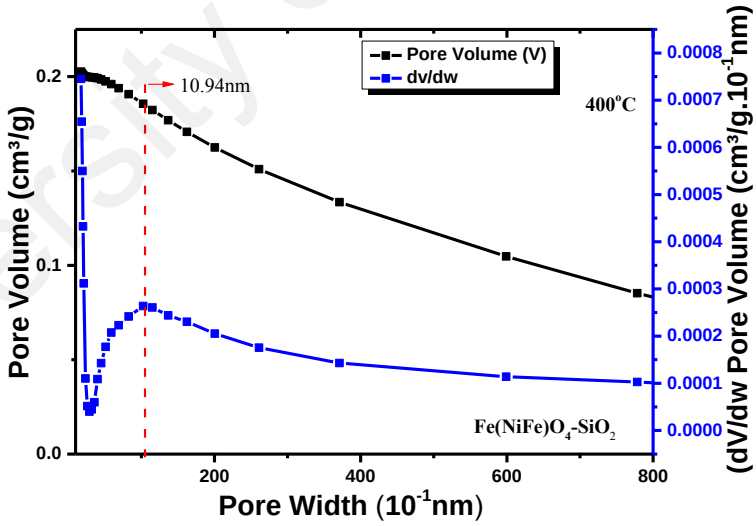

University of Malaya

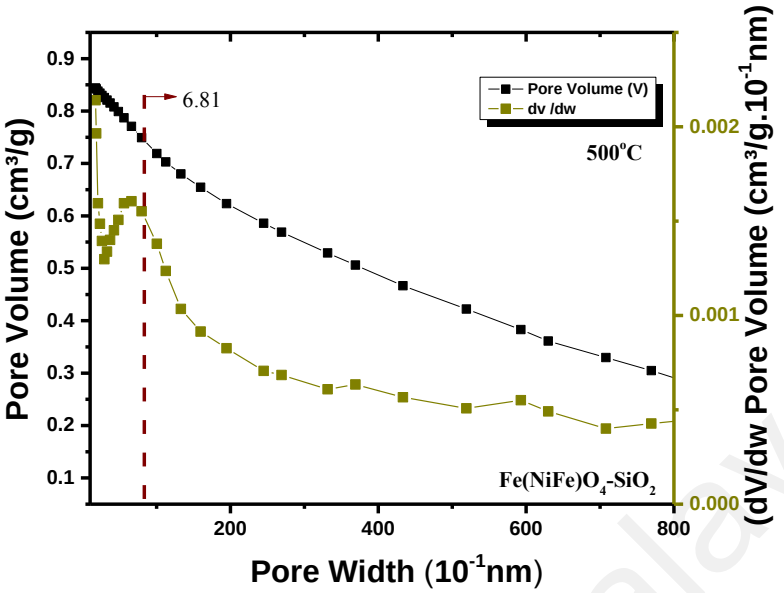

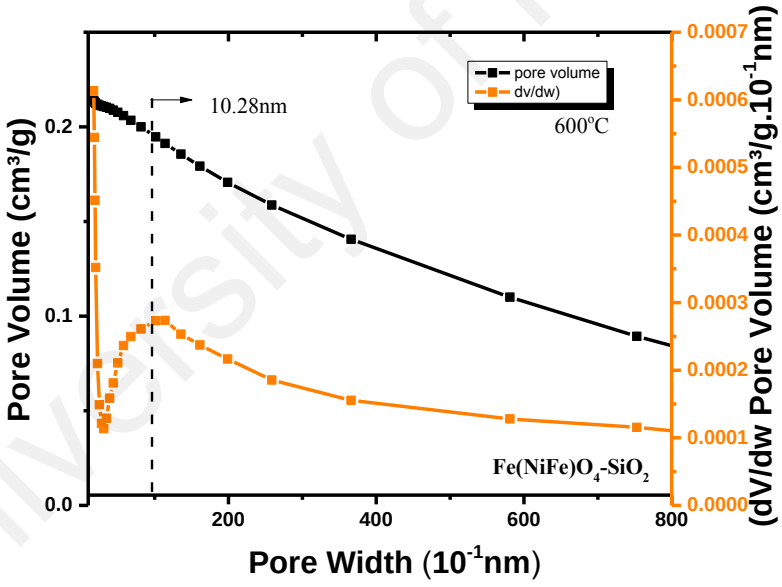

University of Malaya

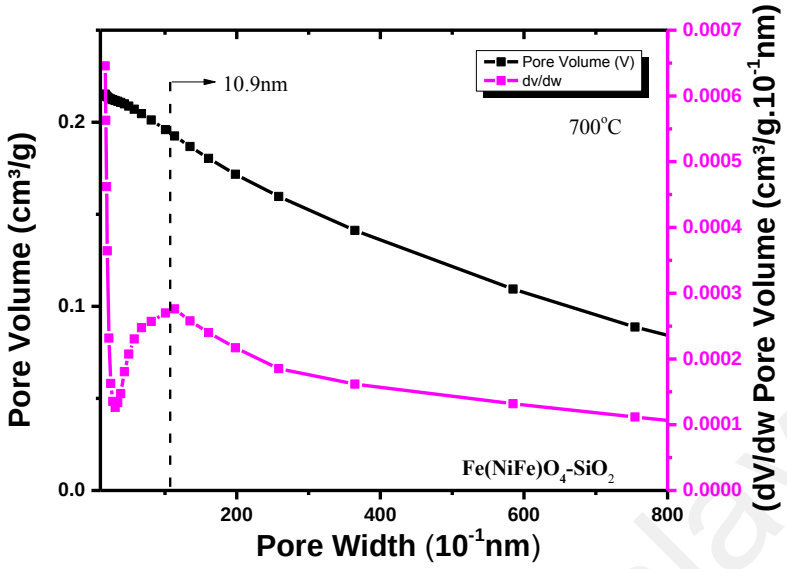

E.1: BET analysis on $Fe(RuFe)O_4$-SiO_2

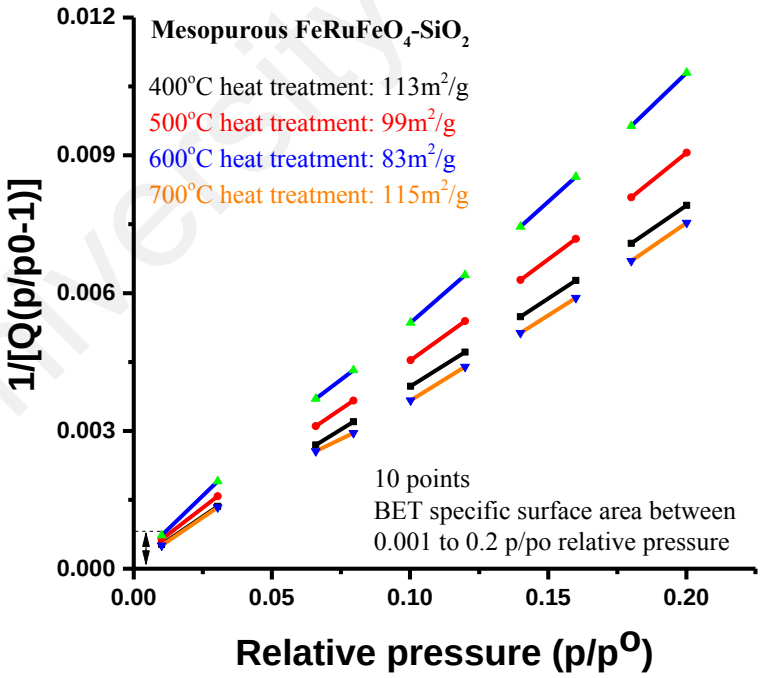

University of Malaya

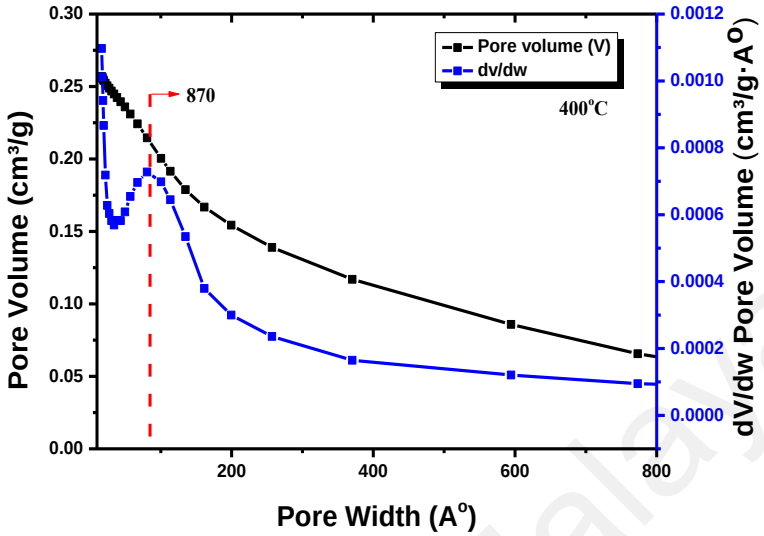

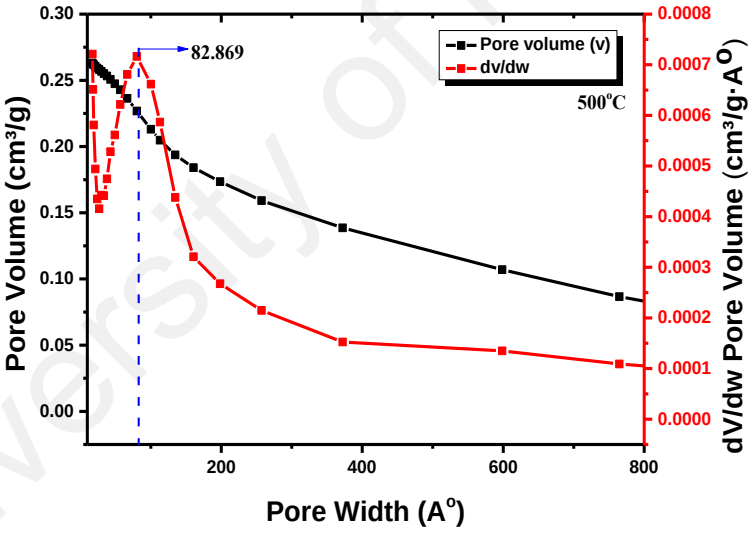

University of Malaya

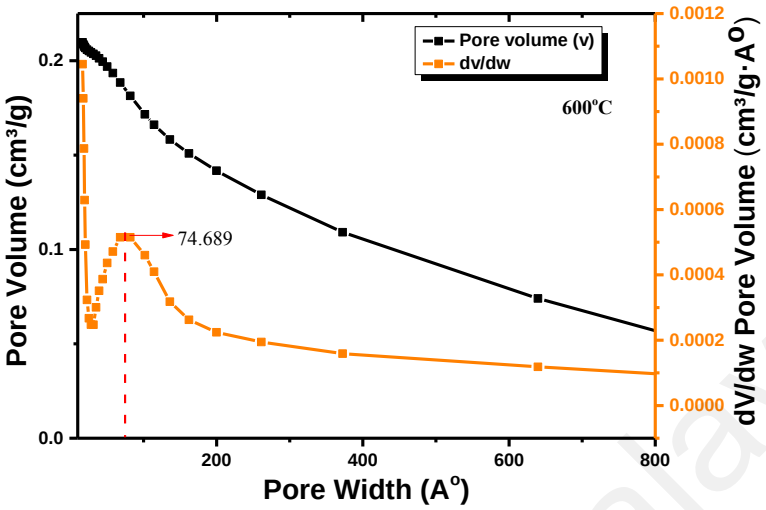

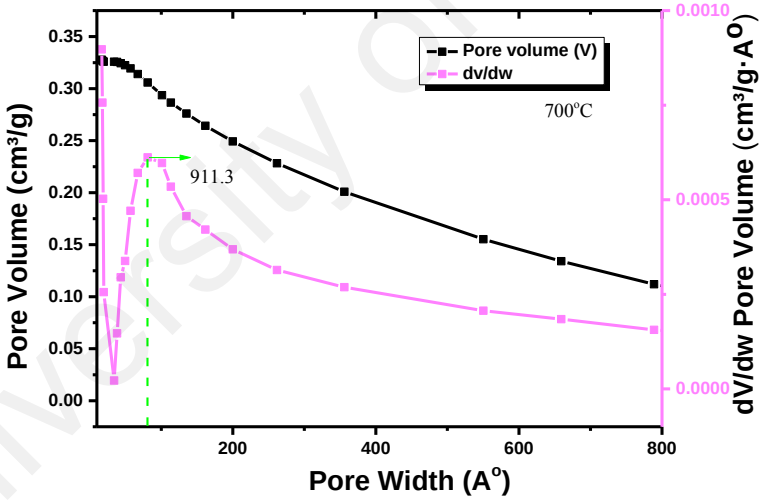

University of Malaya

Appendix F: Synopsis on some GC analysis

F.1 GC-Temperature programs

Table F.1: Temperature program for furfuryl alcohol GC analysis.

Oven Ramp	°C/min	Next °C	Hold min	Run Time
Initial		40	5	5.00
Ramp 1	15	161	10	23.07
Ramp 2	15	170	10	33.67
Post Run		50	0.00	33.67

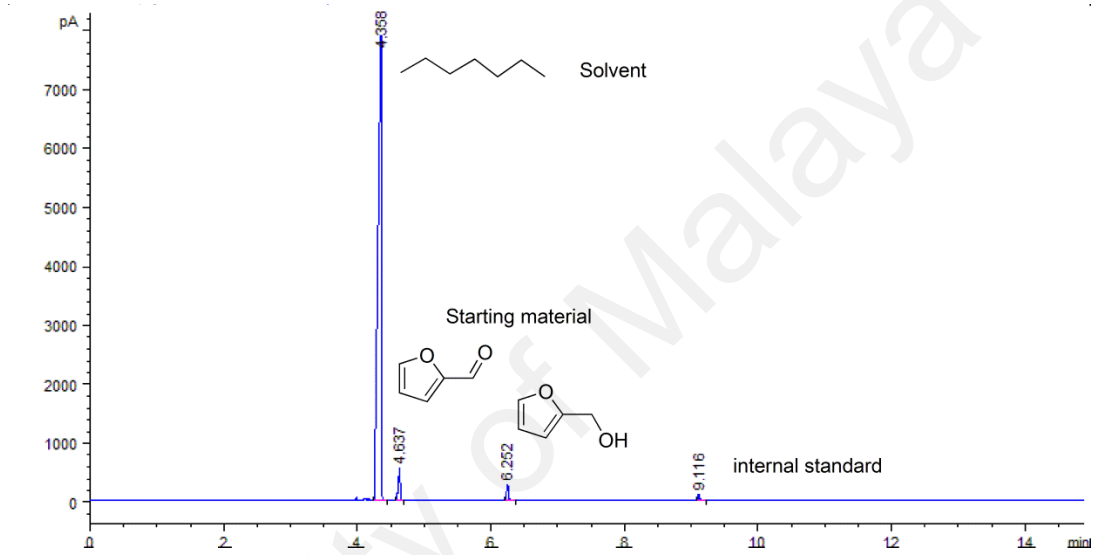

Table F.2 Temperature program for vanillin hydrogenation products GC analysis

Oven Ramp	°C/min	Next °C	Hold min	Run Time
Initial		40	2	2
Ramp 1	15	160	2	12
Ramp 2	15	230	5	21.67
Post Run		50	0.00	21.67

University of Malaya

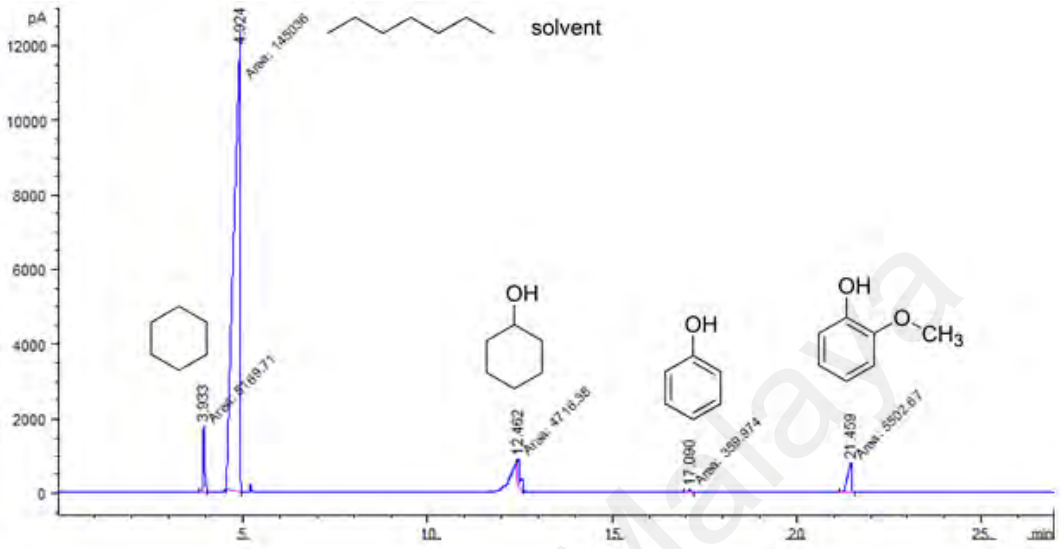

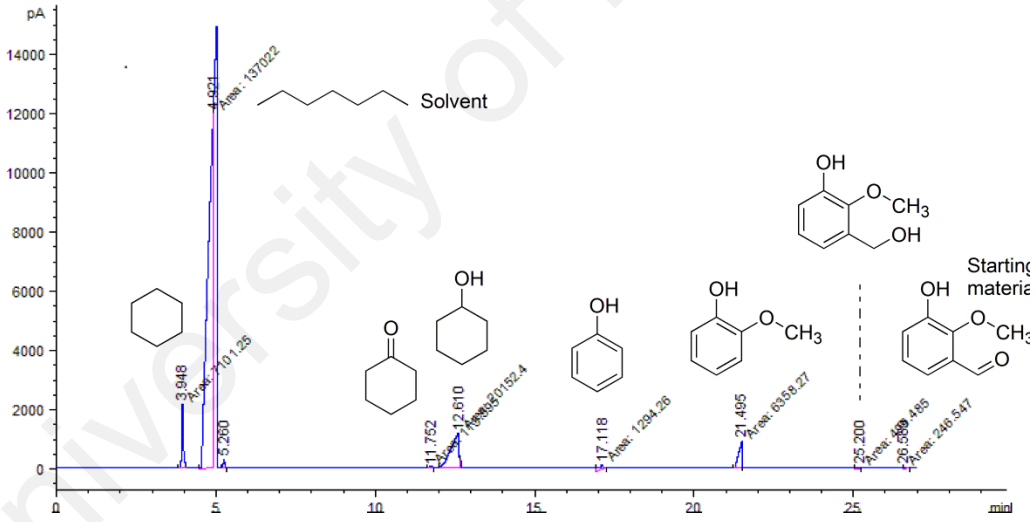

University of Malaya

APPENDIX G Guide to mechanism of reaction

G.1: Time dependent density functional theory showing homo and lumo for furfural

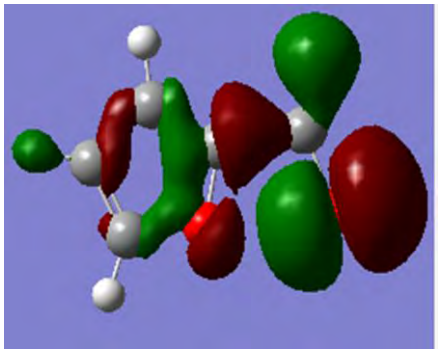

S1 Electron density for HOMO

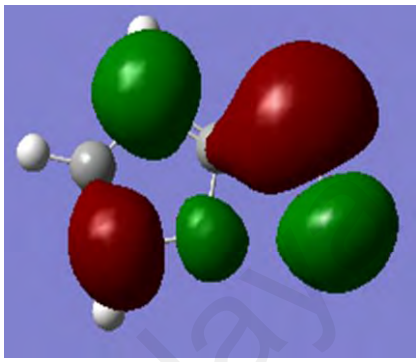

S1 Electron density for LUMO

Excitation energies and oscillator strengths:

Excited State 1: Singlet-A 2.1207 eV 584.64 nm f=0.0000 <S**2>=0.000

25 -> 26 0.70585

This state for optimization and/or second-order correction.

Total Energy, E(TD-HF/TD-KS) = -341.276490083

Copying the excited state density for this state as the 1-particle RhoCI density.

Excited State 2: Singlet-A 4.1303 eV 300.18 nm f=0.2101 < S**2 > = 0.000

23 -> 26 -0.14859

24 -> 26 0.68664

24 <- 26 -0.11114

University of Malaya

Excited State 3: Singlet-A 4.8326 eV 256.56 nm f=0.0421 <S**2>=0.000

23 -> 26 0.68037

24 -> 26 0.14270

G.2: Time dependent density functional theory showing homo and lumo for vanillin

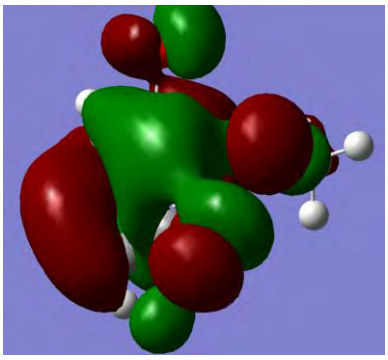

S2 Electron density for HOMO

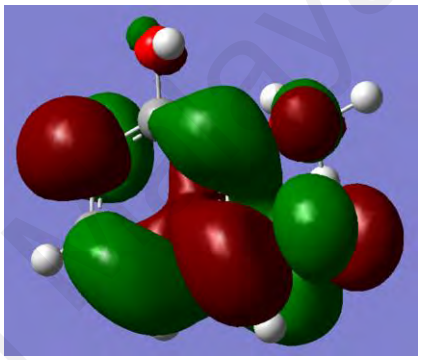

S2 Electron density for LUMO

Excitation energies and oscillator strengths:

Excited State 1: Singlet-A 2.4760 eV 500.73 nm f=0.0004 <S**2>=0.000

38 -> 41 0.21583

39 -> 41 0.56650

40 -> 41 -0.34481

This state for optimization and/or second-order correction.

Total Energy, E(TD-HF/TD-KS) = -532.167918849

University of Malaya

Copying the excited state density for this state as the 1-particle RhoCI density.

Excited State 2: Singlet-A 3.2284 eV 384.05 nm f=0.0287 <S**2>=0.000

38 -> 42 -0.13125

39 -> 41 0.37300

40 -> 41 0.57893

Excited State 3: Singlet-A 4.0584 eV 305.50 nm f=0.0593 <S**2>=0.000

37 -> 41 0.50503

38 -> 41 -0.42800

39 -> 41 0.11649

40 -> 41 -0.16187

University of Malaya

Appendix H 2D and 3D images of atomic force microscopy on $Fe(RuFe)O_4$-SiO_2 and $Fe(NiFe)O_4$-SiO_2 nanoparticle catalyst that was treated at 500°C

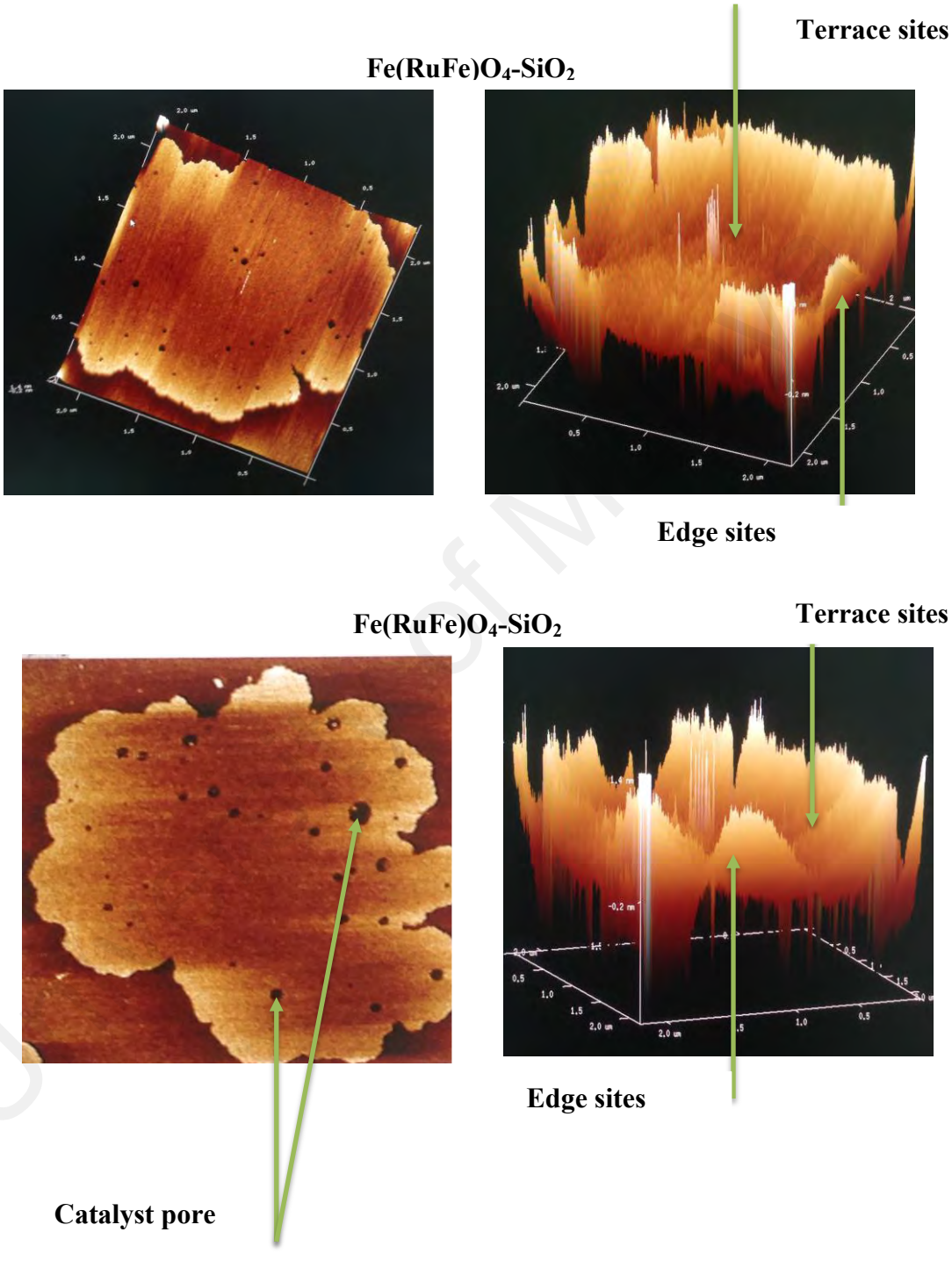

APPENDIX I: Z-matrix (Cartesian coordinates)

Charge = 0 Multiplicity = 2

Symbolic Z-Matrix:

Si-Si3	3.96382	-0.0179	0.00583
O-O_2	4.03515	-0.79387	1.32383
O-O_2	2.62465	0.71903	-0.08063
O-O_2	5.10937	0.99641	-0.05201
O-O_2	4.08614	-0.99347	-1.16803
Fe-Fe3+2	1.06402	-0.22216	-0.04138
O-O_3	-0.36078	0.94506	-0.15786
Fe-Fe3+2	-1.84963	-0.11822	0.08631
O-O_3	-3.37076	0.92385	0.00282
Ni-Ni4+2	-4.70546	-0.24155	-0.03083
H-H_	-0.30515	1.48787	0.66850

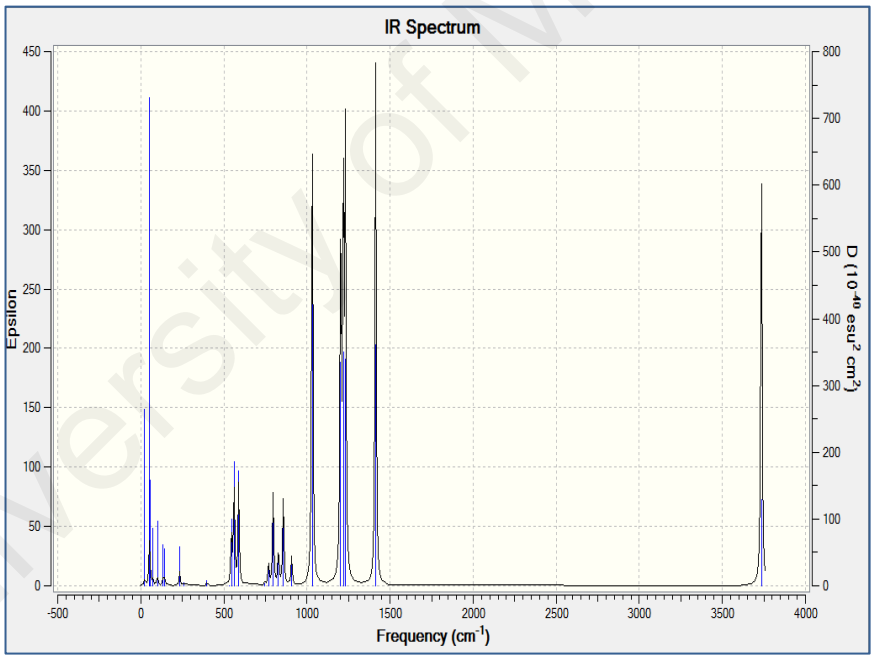

University of Malaya

APPENDIX J: List of Publications and Papers Presented

J.1 Book chapter on bio-refining prospects of lignocellulose biomass resource to fuel

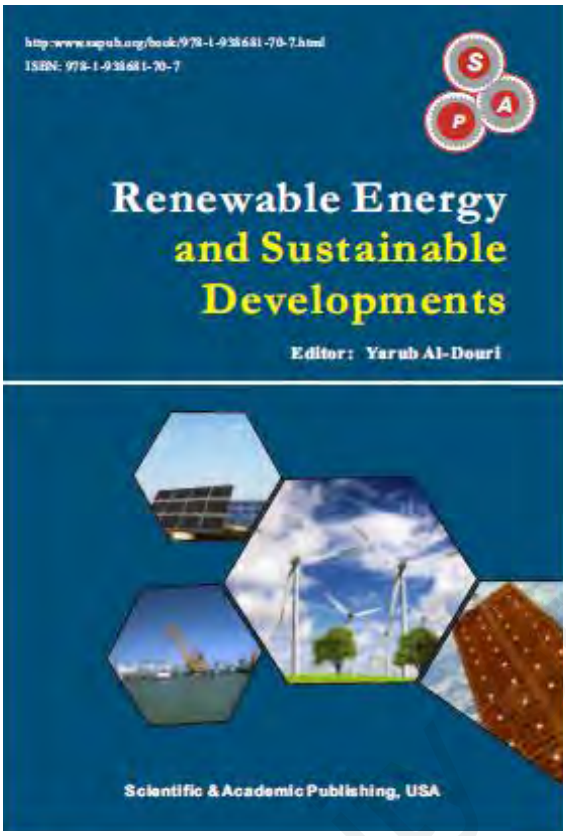

Chapter 11

Opportunities in Utilization of Lignocellulosic Biomass Oil to Bio-Esters

Sharifah Bee Abd Hamid, Ahmed Halilu, Sharafadeen Gbadamasi, Luqman Hakim

Nanotechnology & Catalysis Research Centre (NANOCAT), Block A, IPS Building, University of Malaya (UM), Kuala Lumpur, Malaysia

Abstract Nowadays, serious environmental pollution and energy crisis are the most threatening problems to human kinds. Therefore, executing research for generating clean energy has been the interest of the global community. Clean energy resource poses no environmental challenges due to its renowned renewability. One of the prospective ways to produce clean energy is to convert lignocellulosic biomass into bio oil which has energy density up to 20MJ/M^3 through fast pyrolysis or hydrothermal treatments. Bio oil is upgraded over range of catalysts via different routes into more useful energy resource such as bio-esters because of its associated challenges such as high amount of oxygenated compounds leading to chemical instability over time and also low heating value among others. The main focus of this review article is to elucidate the state-of-the-art in eliminating these challenges using two of the applauded techniques of upgrading bio oil such as Hydrodeoxygenation (HDO), and one step hydrogenation-esterification (OHE). These processes are all high pressure operations employing a wide range of heterogeneous catalysts. Critical information has been shown on how hydrogen is used to remove oxygen from bio-oil in the former route and also used to upgrade the unstable bio oil in the

http:www.sapub.org/book/978-1-938681-70-7.html

University of Malaya

J.2: First research article (energy & fuels)

energy&fuels

Article

pubs.acs.org/EF

Highly Selective Hydrogenation of Biomass-Derived Furfural into Furfuryl Alcohol Using a Novel Magnetic Nanoparticles Catalyst

Ahmed Halilu,[†,‡] Tammar Hussein Ali,[†] Abdulazeez Yusuf Atta,[‡] Putla Sudarsanam,[§] Suresh K. Bhargava,[§] and Sharifah Bee Abd Hamid*[,†]

[†]Nanotechnology and Catalysis Research Center, (NANOCAT) Universiti Malaya, 50603 Kuala Lumpur, Malaysia

[‡]Department of Petrochemicals, National Research Institute of Chemical Technology (NARICT), P.M.B. 1052 Zaria, Nigeria

[§]Centre for Advanced Materials and Industrial Chemistry (CAMIC), School of Applied Sciences, RMIT University, Melbourne VIC 3001, Australia

ABSTRACT: Designing efficient and facile recoverable catalysts is desired for sustainable biomass valorization. This work reports the one-pot synthesis of a novel magnetic $Fe(NiFe)O_4-SiO_2$ nanocatalyst for hydrogenation of biomass-derived furfural into valuable furfuryl alcohol. Various techniques were used to systematically analyze the physicochemical properties of the $Fe(NiFe)O_4-SiO_2$ nanocatalyst. Vibrating sample magnetometer analysis reveals low coercivity of $Fe(NiFe)O_4-SiO_2$ (6.991 G) compared with that of $Fe_3O_4-SiO_2$ (27.323 G), which is attributed to highly dispersed Ni species in the $Fe(NiFe)O_4-SiO_2$ catalyst. HRTEM images indicated the nanosized nature of the $Fe(NiFe)O_4-SiO_2$ catalyst with an average diameter of ~14.32 nm. The $Fe(NiFe)O_4-SiO_2$ catalyst showed a superior BET surface area (259 m^2/g), which is due to the formation of nanosized particles. The magnetic $Fe(NiFe)O_4-SiO_2$ nanocatalyst shows a remarkable performance with 94.3 and 93.5% conversions of furfural and ~100% selectivity of furfuryl alcohol at 90 °C and 20 H_2 bar and 250 °C and 5 H_2 bar, respectively. Using heptane as a solvent, the effect of temperature, pressure, reactant amount, and catalyst loading were investigated to optimize the reaction conditions. A probable mechanism via a non-hydrogen spillover route was proposed for the hydrogenation of furfural to furfuryl alcohol over the magnetic $Fe(NiFe)O_4-SiO_2$ nanocatalyst. The efficiency of the magnetic $Fe(NiFe)O_4-SiO_2$ nanocatalyst is attributed to highly dispersed nickel species, which plays a key role in the dissociation of H_2 into a proton and a hydride in the furfural hydrogenation. The superior performance of the magnetic $Fe(NiFe)O_4-SiO_2$ nanocatalyst, along with the advantages of low cost and easy recoverability, could make it a new appealing catalyst in various selective hydrogenation reactions.

1. INTRODUCTION

The world is presently facing detrimental environmental problems due to vast consumption of fossil fuels and associated global warming effects.[1−3] The consumption of fossil fuels results in increasing levels of greenhouse gas (GHG) emissions; CO_2 levels have increased from 284 ppm in 1832 to 397 ppm in 2013.[3] Global GHG emissions are expected to rise by ~2.5% in 2015 compared with 2013 levels. If this situation continues, global average temperatures will increase by 2.5−5.4 °C above preindustrial levels by 2050. Concurrently, it is expected that the global production of petroleum will reach a maximum by 2020 and thereafter decay gradually.[1] These growing concerns have motivated the researchers to search for alternative renewable feed-stocks for the production of fuels and chemicals.

In this context, biomass is a potential feedstock alternative to fossil fuels due to its high abundance, biodegradability, and remarkable sustainability.[4−6] Nature itself produces 170 billion metric tons of biomass per year by photosynthesis. Especially, lignocellulose contains a large amount of biomass with three major components: cellulose (~35−50%), hemicellulose (~20−35%), and lignin (~10−25%). Thus, the production of fuels and chemicals from lignocellulose derivatives is an attractive way to overcome the negative impacts of fossil fuels.

Furfural is one of the promising biomass platform chemicals that can be largely produced from acidic hydrolysis of hemicellulose.[5,7−11] Several processes have been developed for the conversion of furfural into a number of valuable chemicals and fuels, such as furfuryl alcohol, 2-methylfuran, 2-methyltetrahydrofuran, tetrahydrofurfuryl alcohol, cyclopentanone, furfurylamine, 1,5-pentanediol, and so on. Among these, the production of furfuryl alcohol by selective hydrogenation of furfural has received paramount interest because of many potential applications of furfuryl alcohol.[10,12,13] For example, furfuryl alcohol is widely used in the chemical industry, mainly for the production of foundry resins, synthetic fiber, farm chemicals, adhesives, and fine chemicals. In addition, furfuryl alcohol is used as a diluent for epoxy resins and as a solvent for phenol formaldehyde resins. In organic synthesis, furfuryl alcohol is a valuable feedstock for the production of tetrahydrofurfuryl alcohol and 2,3-dihydropyran. Moreover, it is a key intermediate for the synthesis of lysine, vitamin C, lubricants, and plasticizers.

In industry, furfuryl alcohol is obtained by hydrogenation of furfural with copper chromite catalysts, operating between 130 and 200 °C, at pressures up to 30 bar.[12] The main drawback of copper chromite catalysts is the toxic nature of chromium oxides, which is highly undesirable from the viewpoints of 12 Green Chemistry Principles. Alternatively, a variety of precious and nonprecious metal catalysts including Pt, Ru, Pd, Co, Cu,

Received: December 11, 2015
Revised: February 2, 2016
Published: February 3, 2016

ACS Publications © 2016 American Chemical Society

DOI: 10.1021/acs.energyfuels.5b02826
Energy Fuels 2016, 30, 2216−2226

J.3: Second research article (ACS Catalysis)

Tuning the surface atomic frontiers of mesoporous magnetic $Fe(MFe)O_4$-SiO_2 (M = Ru and Ni) nanocatalysts for hydro-processing of biomass model compounds

Sharifah Bee Abd Hamid[†*] Ahmed Halilu[†‡], Abdulazeez Yusuf Atta[‡], Putla Sudarsanam[§], Suresh K. Bhargava[§],

[†] Nanotechnology and Catalysis Research Center, (NANOCAT) Universiti Malaya, 50603 Kuala Lumpur, Malaysia.

[‡]Department of Petrochemicals and Allied, National Research Institute of Chemical Technology (NARICT), P.M.B 1052, Nigeria.

[§]Centre for Advanced Materials and Industrial Chemistry (CAMIC), School of Applied Sciences, RMIT University, Melbourne VIC 3001, Australia

KEYWORDS: Structural, reactivity, hydro-processing, magnetic catalyst

ABSTRACT. Tuning the surface atomic properties of magnetic nanocatalysts is vital for the advancement of catalysis and biomass valorization fields. In this work, a facile cost-effective method, i.e. heat treatments from 400 to 700 °C were employed to modify the properties of magnetic $Fe(MFe)O_4$-SiO_2 (M = Ru and Ni) nanocatalysts for hydro-processing of biomass model compounds, such as furfural and vanillin. The estimated surface atomic densities indicate reconstructions of surface atoms during the heat treatment, resulting in the formation of terrace and edge sites on the catalyst surface, which is further evidenced by atomic force spectroscopy analysis. For both catalysts, the crystallite size is increased with the increase of heat treatment from 400 to 600 oC and then decreases at 700 ^oC. The product distributions in hydro-processing of furfural and vanillin are highly dependent on the heat treatment and the catalyst. A high selectivity of cyclohexanone is found in hydro-processing of vanillin for $Fe(NiFe)O_4$-SiO_2 calcined at 400 ^oC and it's selectivity drastically decreased, with the increase of cyclohexane by increasing heat treatment up to 700 ^oC. In contrast, except at 500 ^oC heat treatment (cyclohexane is the major product), a high selectivity of cyclohexanol was found in hydro-processing of vanillin for $Fe(RuFe)O_4$-SiO_2 catalyst. In hydro-processing of furfural, a high selectivity of tetrahydrofuran was found with both catalysts treated at 600 ^oC. Time dependent density functional theory (TD-DFT) calculations were applied for a fundamental understanding of electron density distribution in furfural and vanillin. Based on TD-DFT calculations and catalytic activity results, we postulated possible reaction pathways for hydro-processing of furfural and vanillin.

University of Malaya

J.4: International conference on chemistry, chemical and petrochemical engineering (ICCCPE), 2016